UNIVERSIDAD
NACIONAL
DE COLOMBIA

A machine learning framework to support multi-channel time series classification in BCI systems with preserved interpretability

Mateo Tobón Henao

Universidad Nacional de Colombia
Faculty of Engineering and Architecture
Department of Electric, Electronic and Computing Engineering
Manizales, Colombia
2023

A machine learning framework to support multi-channel time series classification in BCI systems with preserved interpretability

Mateo Tobón Henao

Dissertation submitted as a partial requirement to receive the grade of:
Master of Engineering - Automatics

Advisor:
Prof. Andrés Marino Álvarez-Meza, Ph.D.

Co-Advisor:
Prof. Germán Castellanos-Domínguez, Ph.D.

Academic research group:
Signal processing and recognition group (SPRG)

Universidad Nacional de Colombia
Faculty of Engineering and Architecture
Department of Electric, Electronic and Computing Engineering
Manizales, Colombia
2023

Metodología de aprendizaje automático para la clasificación interpretable de series de tiempo multicanal en sistemas BCI.

Mateo Tobón Henao

Disertación presentada como requisito parcial para recibir el título de:
Maestría en Ingeniería - Automatización Industrial

Director:
Prof. Andrés Marino Álvarez-Meza, Ph.D.

Codirector:
Prof. Germán Castellanos-Domínguez, Ph.D.

Grupo de investigación:
Grupo de control y procesamiento digital de señales (GCPDS)

Universidad Nacional de Colombia
Facultad de Ingeniería y Arquitecura
Departamento de Ingeniería Eléctrica, Electrónica y Computación
Manizales, Colombia
2023

ACKNOWLEDGEMENTS

I am sincerely thankful to God for providing strength and guidance throughout my academic journey. I express gratitude to my beloved children, Maria Antonia and Isaac, whose love and smiles were a constant source of motivation during challenging times. I extend heartfelt thanks to my supportive wife and dedicated parents for their unwavering encouragement and lifelong commitment to my education. Additionally, I appreciate the guidance of Professors Andrés Marino Álvarez Meza and Germán Castellanos Domńguez, and the Signal Processing and Recognition Group (SPRG) at Universidad Nacional de Colombia sede Manizales for their valuable input and academic discussions. Special acknowledgment is extended to Daniel Guillermo Garcia and Dayan Alexander Benavides for their contributions to discussions and document support. Lastly, I recognize that this research would not have been possible without the support given by the project: *Caracterización Morfológica de Estructuras Cerebrales por Técnicas de Imagen para el Tratamiento Mediante Implantación Quirúrgica de Neuroestimuladores en la Enfermedad de Parkinson (código 110180763808)*, funded by MINCIENCIAS, and *Sistema prototipo de procesamiento de bioseñales en unidades de cuidado intensivo neonatal utilizando aprendizaje de máquina - Fase 1: Validación en ambiente simulado, Hermes 55063, funded by Universidad Nacional de Colombia.*

ABSTRACT

Brain-Computer Interfaces (BCIs) based on Electroencephalography (EEG) have gained significant attention as a practical approach for human-technology interaction. Motor imagery (MI) paradigms, wherein users mentally simulate motor tasks without physical movement, are widely employed in BCI development. However, constructing EEG-based BCI systems faces challenges due to the low Signal-to-Noise Ratio (SNR), non-stationarity, and nonlinearity of EEG signals, as well as the inter- and intra-subject variability that hinders the extraction of discriminant features. Additionally, poor motor skills among subjects lead to difficulties in practicing MI tasks under low SNR scenarios.

To address these challenges, this thesis proposes two novel methodologies for EEG-based MI classification. Firstly, a subject-dependent preprocessing approach, termed Subject-dependent Artifact Removal (SD-AR), is presented. This approach employs Surface Laplacian Filtering and Independent Component Analysis algorithms to selectively remove signal artifacts based on the subjects' MI performance. The study also investigates power- and phase-based functional connectivity measures to extract relevant and interpretable patterns and identify subjects with suboptimal performance. The SD-AR methodology significantly improves MI classification performance in subjects with poor motor skills by effectively mitigating electrooculography and volume-conduction EEG artifacts.

Secondly, a deep learning methodology, named kernel-based regularized EEGNet (KREEGNet), is introduced for EEG-based MI classification. KREEGNet is built on the foundation of centered kernel alignment and Gaussian functional connectivity, addressing the challenge of intrasubject variability and lack of spatial interpretability within end-to-end frameworks. The novel architecture of KREEGNet includes an additional kernel-based layer for regularized Gaussian functional connectivity estimation using CKA. Experimental results from binary and multiclass MI classification databases demonstrate the superiority of KREEGNet over baseline EEGNet and other state-of-the-art methods. The model's interpretability is further explored at individual and group levels, utilizing classification performance measures and pruned functional connectivities.

In conclusion, the proposed methodologies in this thesis contribute to enhancing the reliability, interpretability, and classification performance of EEG-based MI paradigms in BCI systems. The SD-AR approach effectively tackles artifacts and enhances the quality of EEG data, particularly for subjects with poor motor skills. On the other hand, KREEGNet demonstrates remarkable performance improvements and provides spatial interpretability, making it a promising alternative for interpretable end-to-end EEG-BCI based on deep learning. These advancements pave the way for more effective and practical BCI applications in real-world scenarios.

Keywords: BCI, MI, EEG, ML, DL, multi-channel time series, relevance analysis

RESUMEN

Las interfaces cerebro-computadora (BCIs) basadas en señales de electroencefalografía (EEG) han ganado una atención significativa en los últimos años como un enfoque práctico para la interacción humano-computadora. Los paradigmas de imaginación motora (MI), donde los usuarios simulan mentalmente tareas motoras sin movimiento físico, son ampliamente empleados en el desarrollo de BCI. Sin embargo, la construcción de sistemas BCI basados en señales de EEG enfrentan importantes desafíos debido al bajo índice de Señal a Ruido (SNR), la no estacionariedad y la no linealidad de las señales de EEG, así como la variabilidad inter e intrasujeto que dificultan la extracción de características discriminantes.

Para abordar estos desafíos, esta tesis propone dos metodologías novedosas para la clasificación de MI basada en EEG. En primer lugar, se presenta un enfoque de preprocesamiento sujeto dependiente, denominado Eliminación de Artefactos sujeto dependiente (SD-AR, por sus siglas en inglés). Este enfoque emplea el Filtrado Laplaciano de Superficie y algoritmos de Análisis de Componentes Independientes para eliminar selectivamente artefactos de las señales de EEG basados en el rendimiento que cada uno de los sujetos obtiene durante la tarea de MI. Igualmente se investiga el uso de medidas de conectividad funcional basadas en potencia y fase para extraer patrones relevantes e interpretables e identificar sujetos con rendimiento subóptimo. La metodología SD-AR mejora significativamente el rendimiento de clasificación de MI en sujetos con habilidades motoras deficientes al

mitigar efectivamente los artefactos de electrooculografía y conducción de volumen en EEG.

En segundo lugar, se introduce una estrategia de regularización basada en kernels y la red neuronal EEGNet (KREEGNet). KREEGNet se construye a base del método de alineamiento de kernel centralizado y la conectividad funcional gaussiana, abordando el desafío de la variabilidad intrasujeto y la falta de interpretabilidad espacial en arquitecturas de aprendizaje profundo. Esta novedosa arquitectura (KREEGNet) incrusta una capa adicional a la arquitectura EEGNet que se construye a base del kernel gaussiano y se utiliza para estimar la conectividad funcional gaussiana. Posteriormente, la salida de esta capa se utiliza como entrada al regularizador basado en CKA . Los resultados experimentales en bases de datos públicas demuestran la superioridad de KREEGNet sobre EEGNet y otros métodos de vanguardia. Además, se lleva a cabo una interpretabilidad del modelo a nivel individual y grupal, utilizando métricas de rendimiendo para tareas de clasificación y conectividades funcionales relevantes.

En conclusión, las metodologías propuestas en esta tesis contribuyen a mejorar la fiabilidad, interpretabilidad y rendimiento de los sistemas BCI basados en señales de EEG para tareas de MI. El enfoque SD-AR aborda efectivamente la eliminación de artefactos y mejora la calidad de las señales EEG, particularmente para sujetos con habilidades motoras deficientes. Por otro lado, KREEGNet demuestra mejoras notables en el rendimiento y proporciona interpretabilidad espacial, convirtiéndose en una alternativa prometedora para hacer interpretables sistemas BCI basados en modelos de aprendizaje profundo.

Palabras clave: BCI, MI, EEG, ML, DL, series de tiempo multicanal, análisis de relevancia

Contents

LIST OF FIGURES

LIST OF TABLES

ABBREVIATIONS

ACC Accuracy 33

AUC Area Under the Receiver Operating Characteristics Curve 33

BCI Brain-Computer Interface 1

CAR Common Average Reference 8

CKA Centered Kernel Alignment 18

COH Spectral Coherence 28

CSP Common Spatial Patterns 2

DL Deep Learning 3

EEG Electroencephalography 2

EOG Electrooculography 17

ERD/ERS Event-Related Desynchronization/Synchronization 9

FC Functional Connectivities 2

GCN Graph Convolution Neural Network 10

GFC Gaussian Functional Connectivity xvii, 17

ICA Independent Component Analysis 2

Ind-AR subject-independent artifact removal 39

ISV Inter-subject variability xiii, 6

kappa Cohen's Kappa coefficient 33

KL Kullback-Leibler 87

KREEGNet Kernel-based Regularized EEGNe 46

KS Kolmogorov-Smirnov 63

LDA Linear Discriminant Analysis 3

LRP Layer-Wise Relevance Propagation 14

MI Motor imagery 1

ML Machine learning 2

PCA Principal Component Analysis 3

PLV Phase-Locking Value 28

SD-AR Subject-Dependent Artifact Removal 23

SL Surface Laplacian 2

SNR Signal-to-noise ratio 8

SPRG Signal Processing and Recognition Group 4

CHAPTER

ONE

INTRODUCTION

1.1 Motivation

Brain-Computer Interface (BCI)s have emerged as a cutting-edge technology that directly connects the human brain and external devices, bridging the ultimate frontier between humans and computers [Venkatachalam et al., 2020, Abiri et al., 2019]. This breakthrough technology has enabled people with neuromotor disorders, nervous system injuries, or limb amputations to control machines using their brains, as no peripheral nerves or muscles are involved in the process [Dai et al., 2020]. Motor imagery (MI) is one of the essential branches of BCIs control paradigms, which allows users to control robots or external machines merely by imagining movement without the intervention of peripheral nerves [Wang et al., 2017, Gaur et al., 2021].

BCI technology has significant potential in motor function rehabilitation [Steenbergen et al., 2020, Khan et al., 2020], assistance [Kanna and Vasuki, 2021], and other areas, sparking extensive discussions on MI-based BCIs [Miao et al., 2020]. Acquiring brain

activity is a critical aspect of MI-based BCIs, and multi-channel time series signals as Electroencephalography (EEG) are commonly preferred due to their high time resolution, cost-effectiveness, and user-friendliness compared to other neuroimaging methods [Padfield et al., 2019]. Moreover, the use of multi-channel time series signals in MI tasks is essential as it captures the activation of multiple brain regions, enabling a comprehensive understanding of complex neural activity [Kaur and Kaur, 2015]. These signals facilitate the exploration of Functional Connectivities (FC) and coordinated patterns between brain regions during MI while reducing noise and artifacts through redundancy and robust signal processing techniques [Ghosh et al., 2015].

Figure **1-1**. The diagram depicts the typical signal processing steps involved in an EEG-based system for MI.

Traditional Machine learning (ML) approaches have been extensively used to classify MI-EEG data. Figure **1-1** shows a typical BCI signal-processing pipeline with four stages: (i) Preprocessing, (ii) Feature extraction, (iii) Feature selection, and (iv) Classification. The first stage is critical for eliminating noise and artifacts in the EEG signals, which can significantly affect the accuracy of subsequent processing stages. A range of techniques, such as bandpass filters [Sahu et al., 2021], spatial filters like Independent Component Analysis (ICA) [Wang et al., 2015a] and Surface Laplacian (SL) [Kayser and Tenke, 2015], and time filters based on regression models [Sakkaff and Nanayakkara, 2008] are employed to achieve this. The second stage involves feature extraction using advanced methods such as autoregressive models [Krusienski et al., 2006, Kevric and Subasi, 2017], Short-Time Fourier Transform [Tabar and Halici, 2016], Wavelet Transform [Wang et al., 2014], Common Spatial Patterns (CSP) [Yang et al., 2016, Zhang et al., 2017], and FCs [Hamedi et al., 2016]. The extracted features in the time, frequency, and spatial domain represent the user's intended movement, which is crucial for accurate classification. The third stage focuses on identifying the most informative features

from the extracted features using techniques such as Principal Component Analysis (PCA) [Yu et al., 2014], Filter Bank Selection [Kumar et al., 2017], and Evolutionary Algorithms [Liu et al., 2017]. Finally, the fourth stage involves the application of ML algorithms such as Support Vector Machines, Linear Discriminant Analysis (LDA), and Naive Bayes Classifier [Baig et al., 2017, Oikonomou et al., 2017, Kumar et al., 2017] to predict the MI movements from the extracted and selected features.

Nonetheless, the traditional ML approach has limitations, such as the need for manual specification of signal processing [Bashashati et al., 2007], feature extraction [McFarland et al., 2006], and classification methods [Lotte et al., 2007], requiring significant subject-matter expertise and/or prior knowledge about the expected EEG signal. Additionally, the specificity of the EEG signal's preprocessing steps for the EEG feature of interest could exclude potentially relevant EEG features from the analysis.

End-to-end Deep Learning (DL) models such as DeepConvnet, ShallowConvnet [Schirrmeister et al., 2017], EEGNet [Lawhern et al., 2018], and TCNet-fusion [Musallam et al., 2021] have recently been proposed to overcome these limitations by automatically preprocessing and extracting relevant features from the EEG signals. These models have shown superior performance over traditional ML models in various EEG signal classification tasks, capturing complex patterns and relationships within the data.

In spite of this, the nested non-linear structure of these models makes them uninterpretable, which makes it difficult to understand how they arrive at their predictions [Samek et al., 2017]. This lack of interpretability is particularly problematic in MI-based BCI, where decisions based on the model's predictions can have significant consequences [Hu et al., 2023]. For instance, in the case of an MI-based BCI system controlling a prosthetic limb, it is crucial to understand how the system makes its decisions to ensure the limb's accurate and safe control. Therefore, the lack of transparency in black box DL models can make identifying potential sources of errors or biases challenging, leading to ineffective motor rehabilitation interventions.

Consequently, developing explainability techniques is necessary to provide a clear understanding of how the models make predictions. Specifically, in MI-based BCI, the explainability of the model is essential in identifying the brain regions and neural processes involved in the MI tasks [Hashem et al., 2023]. This knowledge can provide insights into the mechanisms underlying motor imagery and facilitate the development of more effective motor rehabilitation interventions.

In a local context, the Signal Processing and Recognition Group (SPRG), associated with the Universidad Nacional de Colombia and classified as A1 by Minciencias, has researched biosignals analysis and developed computer-aided diagnosis by data analytics and machine learning techniques. In particular, during the last years, the SPRG has been working on the design of methodologies to improve the performance and explainability of EEG-based BCIs [García-Murillo et al., 2023, Collazos-Huertas et al., 2023] in a variety of research projects (supported by Minciencias, Dirección Nacional de Investigaciones de Manizales (DIMA), and Vicerrectoría de Investigaciones de la Universidad Nacional de Colombia)

- Procesamiento de señales de electroencefalografía en interfaz cerebro-computador orientado a la detección de imaginación motora utilizando modelos de aprendizaje profundo y medidas de conectividad.
- Prototipo de interfaz cerebro-computador multimodal para la detección de patrones relevantes relacionados con trastornos de impulsividad.
- Prototipo de interfaz cerebro-computador de bajo costo para la detección de patrones relevantes de actividad eléctrica cerebral relacionados con TDAH.
- Prototipo de interfaz cerebro-computador multimodal para la detección de patrones relevantes relacionados con trastornos de impulsividad.
- Interfaz cerebro-computador basada en aprendizaje de máquina y teoría de información como soporte a la detección de trastornos de déficit de atención e hiperactividad.

- Brain Music: Prototipo de interfaz interactiva para generación de piezas musicales basado en respuestas eléctricas cerebrales y técnicas de composición atonal.

Therefore, from both local and general perspectives, it is essential to continue developing and improving accurately and explainable MI EEG-based BCIs to enable individuals with neuromotor disorders or limb amputations to control external devices accurately and enhance transparency.

1.2 Problem statement

The insufficient functioning of MI EEG-based BCIs can have severe consequences for individuals relying on these devices. These BCIs enable users to control external devices or prosthetics through their thoughts, but their suboptimal performance leads to frustration, inaccuracy, and reduced functionality [Han et al., 2019]. To enhance BCI effectiveness, it is necessary to prioritize transparency in BCIs. This can result in improved operational efficiency and smoother integration of BCI technology into daily life, ultimately improving the quality of life for individuals with motor disabilities [Collazos-Huertas et al., 2021a].

The factors contributing to the limited effectiveness of BCIs during MI tasks are complex and varied. Inter-subject variability is a significant factor that contributes to poor performance [Saha and Baumert, 2020], but mood, attention, and fatigue can also exert substantial influence. Additionally, the lack of interpretability in BCIs poses a critical challenge, hindering the identification of distinguishable patterns between high-performing and low-performing subjects. The difficulty in interpreting MI EEG-based BCIs and understanding their decision-making processes complicates the optimization of design and the enhancement of MI functionality [Salami et al., 2022].

In conclusion, this master's thesis addresses two significant challenges in the field of MI EEG-based BCIs. The first challenge is ISV, where the performance of BCIs varies

substantially among subjects due to various factors, including gender, age, lifestyle, neurophysiological and psychological parameters, genetic differences, and cognitive processes. This variability hinders the development of reliable and accurate BCIs. Furthermore, the presence of noise in EEG signals exacerbates this variability, making it difficult to accurately identify neural activity patterns. The second challenge is the lack of explainability in ML-based algorithms used in MI EEG-based BCIs. The complex nature of these algorithms raises concerns regarding the safety, reliability, and trustworthiness of the system's outputs. It also limits the development of effective interventions and training programs while impeding researchers' understanding of sensorimotor processes.

1.2.1 Inter-subject variability (ISV)

EEG-based BCIs pose a significant challenge due to the variability in subjects' performance during MI tasks. The quality of electrical activity patterns generated by the subjects' brains plays a crucial role in controlling external devices [Pérez-Velasco et al., 2022]. However, these patterns exhibit substantial variation among subjects, even under identical stimuli or conditions [Seghier and Price, 2018]. Various factors, including gender, age, lifestyle, neurophysiological and psychological conditions, genetic differences, and cognitive processes, contribute to this variability [Subirats et al., 2018, Sannelli et al., 2019]. Such diversities in brain patterns result in performance fluctuations, impeding the development of reliable and accurate BCIs [Vidaurre and Blankertz, 2010].

Moreover, noise in EEG signals significantly contributes to this variability, obscuring underlying neural activity and leading to false positives or negatives in interpreting the signal [Caicedo-Acosta et al., 2021]. This noise can originate from various sources, such as electromagnetic interferences, movement artifacts, and individual skull thickness and conductivity differences [LK Jaya Shree, 2021, Roy et al., 2019, Shoka et al., 2019]. These unwanted signals make it difficult to identify the neural activity patterns that drive BCI performance accurately. Therefore, distinguishing the signal from noise is crucial in developing reliable and accurate BCIs.

1.2.2 Explainability in MI EEG-based BCIs

Besides, the lack of explainability of ML-based algorithms in biomedical applications has become a critical issue in recent years. The complexity of these algorithms makes it challenging to understand the decision-making processes and the reasoning behind the system's outputs [Teng et al., 2022]. This lack of transparency raises concerns about the safety and reliability of the system, particularly in critical areas such as clinical decision-making. Without a clear understanding of how the system arrived at its decisions, clinicians may not trust the system's outputs, leading to underutilization or misinterpretation of the results, ultimately affecting patient care [Meng et al., 2022].

Moreover, the insufficient comprehension of the decision-making mechanisms employed by ML-based algorithms in MI EEG-based BCIs is impeding the advancement of effective and dependable interventions and training programs for individuals struggling with this technology [Müller et al., 2004]. This limitation is impeding researchers from addressing the challenges of BCI systems and is ultimately affecting the quality of life of individuals with motor disabilities [Liu et al., 2022]. Besides, the lack of progress in developing better MI BCIs is hindering researchers' ability to comprehend the intricate sensorimotor processes of the brain, which in turn is preventing the development of more accurate and effective BCI systems [Collazos-Huertas et al., 2023]. Therefore, addressing the issue of explainability is crucial to advancing BCI technology and improving the lives of individuals who depend on it.

According to the aforementioned challenges, the following research question emerges: How can an cutting-edge machine learning framework be developed to effectively address the challenges of ISV and the lack of explainability in MI EEG-based BCIs.

1.3 State-of-the-art

1.3.1 Approaches to address ISV

In recent years, ML-based approaches have gained increasing attention to tackle the issue of ISV in MI EEG-based BCIs. Various methods have been proposed to enhance the performance of BCIs during the preprocessing and feature extraction stages. The preprocessing methods aim to mitigate the impact of low Signal-to-noise ratio (SNR) caused by environmental and physiological artifacts such as electrical noise, eye and muscle movements, heart activity, and respiration [Somers et al., 2018]. Additionally, the preprocessing methods aim to tackle the low spatial resolution challenge caused by the volume conduction effect [Kwon et al., 2019]. On the other hand, the feature extraction methods aim to transform raw EEG signals into relevant brain patterns independent of subject-specific differences [Ince et al., 2007]. This approach allows identifying common patterns across individuals, improving the generalizability of BCI systems.

Several methods have been proposed in the literature to address different noise sources, including artifacts and volume conduction. Artifacts in EEG signals can be removed using regression-based techniques, which model the artifacts as regressors and use linear approaches to remove them from the signal [Kotte and Dabbakuti, 2020]. Band-pass and notch filters can also eliminate electrical and environmental noise and frequency bands where neurophysiological information is irrelevant [Singh et al., 2021]. Blind source separation methods, such as canonical correlation analysis, PCA, and ICA, are commonly used to decompose the contaminated EEG signal into statistically independent components and remove or correct the artifact signals [Stergiadis et al., 2022]. Among these methods, ICA is well-known for its success in eliminating various types of artifacts [Rashid et al., 2020, Artoni et al., 2018, Lahane et al., 2019]. In addition, different spatial filters have been proposed to overcome the problem of volume conduction, including the Common Average Reference (CAR) and SL. The CAR spatial filter subtracts the

average electrical activity measured across all sensors from each of the sensors to reduce the recorded noise [Uribe et al., 2019]. Still, it does not address sensor-specific noise and may introduce noise into an otherwise clean sensor [Mridha et al., 2021]. An updated version of CAR, the SL, aims to remove the common brain activity of neighboring sensors due to the volume conduction effect, which improves local topographical features, facilitates sensor-level connectivity analysis, and helps to enhance the SNR [Xu et al., 2018].

Despite the effectiveness of these methods, applying them to all subjects regardless of the individual noise level and type can be detrimental to subjects with clean EEG signals [Repov, 2010]. Indeed, the aforementioned approaches can induce noise, reducing MI performance. For example, the use of an SL filter to address the volume conduction problem for all individuals may inadvertently introduce noise to the EEG signals of unaffected individuals. This occurs because the filter removes the average electrical activity from nearby sensors, thereby altering the original signal information [Tobón-Henao et al., 2022]. Therefore, personalized preprocessing methods that consider individual differences in noise sources are necessary to improve BCI performance.

Feature extraction methods can be broadly categorized into three domains: time, time-frequency, and spatial. In the time domain, amplitude modulation [dos Santos et al., 2020] and time-domain analysis of variance [Rajabioun, 2020] are widely used to extract features related to the amplitude and timing of specific EEG components, providing insights into the underlying neural processes involved in MI. These features facilitate the effective classification of EEG signals into distinct MI classes by maximizing the differentiation among MI patterns within each class. In the time-frequency domain, wavelet transform [Taran and Bajaj, 2019] is a commonly used method that analyzes changes in the frequency content of the EEG signal over time. This method provides information about the temporal dynamics of neural processes during MI, including Event-Related Desynchronization/Synchronization (ERD/ERS) and intertrial coherence. These features improve the accuracy and reliability of the BCI system by capturing the temporal evolution during the MI

task [Sadiq et al., 2019]. In the spatial domain, CSP and FCs are two standard methods used for feature extraction. CSP projects the EEG signals into a lower dimensional space using a set of learned spatial filters that enhance the differences between MI classes [Zhang et al., 2018]. On the other hand, FCs capture the similarity between different EEG channels, providing information on which brain regions interact when a subject performs the MI task [Hsu, 2014]. This technique enables the identification of significant relationships between channels that can be used to classify the MI task effectively.

However, choosing the appropriate feature extraction method for the MI task is challenging, as it demands considerable subject-matter expertise and prior knowledge about the anticipated EEG signal [Bashashati et al., 2007, Lotte et al., 2007]. Moreover, the specificity of the EEG signals' preprocessing steps for the EEG feature of interest could exclude potentially relevant EEG features from the analysis [Van Erp et al., 2012, Lance et al., 2012].

In recent years, end-to-end DL architectures have proven promising in addressing the limitations of traditional methods for handling ISV. These architectures automate preprocessing and feature extraction from EEG signals [Altaheri et al., 2021], covering the entire process from raw input to final output. This enables automatic adaptation to individual MI patterns, reducing dependence on manually crafted features and preprocessing methods that may not generalize well across individuals. End-to-end DL models such as EEGNet, ShallowConvNet, DeepConvNet, EEG-transformer [Song et al., 2021], and Graph Convolution Neural Network (GCN) [Sun et al., 2022, Ma et al., 2022] have great potential to tackle ISV-related challenges. EEGNet and ShallowConvNet utilize convolutional layers to extract spatial and temporal patterns from EEG data. However, EEGNet may struggle with capturing long-range temporal dependencies [He et al., 2022], while ShallowConvNet may not be as effective as deeper architectures in capturing complex patterns. On the other hand, DeepConvNet excels at capturing spatial and temporal patterns but requires a large amount of training data to avoid overfitting [Song et al., 2019]. Transformer-based models like EEG-transformer are adept at processing variable-length EEG sequences by employing

a self-attention mechanism to capture dependencies between different segments [Sun et al., 2021]. However, these models come with higher computational costs in both training and inference stages, necessitating specialized computing engines like GPUs and TPUs, particularly for larger models. Additionally, the larger models may require substantial storage capacity. [Kong et al., 2021]. GCNs, on the other hand, capture spatial relationships between electrodes by aggregating information from neighboring nodes in the graph. Nonetheless, they are sensitive to graph construction from EEG signals [Berton et al., 2015].

Despite their strengths, these DL models can be prone to overfitting when they are too complex or the training data is noisy or insufficient [Yang et al., 2021, Zhang et al., 2019]. To address this challenge, various regularization techniques have been proposed. Domain adaptation aims to reduce variability across different subjects by learning a mapping between source and target domains [Phunruangsakao et al., 2022]. Yet, it requires a substantial amount of labeled data from both domains [Ganin et al., 2016]. Multi-task learning leverages information from related tasks to improve the performance of individual tasks [Halme and Parkkonen, 2018]. Nevertheless, it assumes the availability of multiple related tasks, which may not be practical in specific scenarios [Marquand et al., 2014]. Dropout and batch normalization are also helpful techniques that can reduce ISV. The former randomly drops out a fraction of neurons during training to enhance the model's ability to learn robust features [Roy et al., 2020]. The latter normalizes input features across subjects to enhance network stability and convergence [Huang et al., 2019]. However, both techniques increase computational requirements, and their performance is sensitive to hyperparameters [Srivastava et al., 2014, Ioffe and Szegedy, 2015]. FC-based regularizers introduce a penalty term to obtain low-rank or sparse connectivity matrices, reducing the impact of ISV by enforcing consistent structure among subjects [Mridha et al., 2021]. Nonetheless, these regularizers assume a smooth or sparse connectivity structure of the brain, which may not always hold in practice [Cai et al., 2010]. Figure **1-2** summarizes the previous discussion concerning the ISV issue.

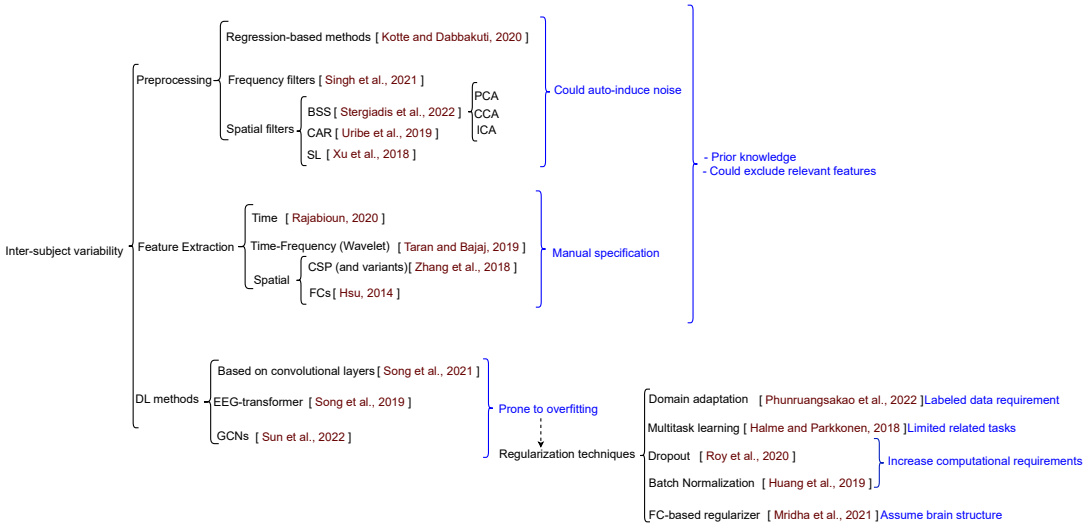

Figure **1-2**. Summary of the main approaches used to tackle the ISV problem and their disadvantages highlighted in blue.

1.3.2 Interpretation techniques for MI-related brain processes

Understanding the neural mechanisms of MI is critical in optimizing the design of EEG-based BCIs [Velasquez-Martinez et al., 2020b]. Various techniques have been employed to achieve this, which can examine the brain processes in the spatiotemporal-frequency domain [Collazos-Huertas et al., 2021b]. These approaches have resulted in improved accuracy and reliability of BCI performance. As such, studying the underlying neural mechanisms of MI is fundamental to advancing BCI technology.

Researchers have employed various time-frequency methods to investigate the brain processes involved in the MI task. These include ERD/ERS plots, Power Spectral Density, and Spectrograms. ERD/ERS plots visually represent changes in EEG signal power in specific frequency bands over time during the MI task [Wilson et al., 2019]. Power spectral density analysis helps identify the frequency bands most relevant to MI and their respective changes in power over time [Cona et al., 2009]. Finally, spectrograms can reveal the temporal dynamics of neural activity by showing how

the power of EEG signals changes in different frequency bands over time during the MI task [Tayeb et al., 2019]. Despite their usefulness, these methods have certain limitations, such as difficulty localizing activity to specific brain regions, risk of misinterpreting spurious correlations as meaningful, and addressing the dimensionality and nonlinearity of EEG signals [Poldrack, 2011, Velasquez-Martinez et al., 2018].

Spatial methods, on the other hand, aim to identify the brain regions where significant brain activity is observed [Marks and Isaac, 1995]. Topographical maps are a well-known technique in spatial methods that show the amplitude or power of EEG signals at specific time points or frequency bands at each electrode [Achanccaray and Hayashibe, 2020]. This approach helps to identify the scalp regions where neural activity related to MI is most prominent. Nonetheless, this method poses limitations regarding spatial resolution, depending on the number of channels and montage used to capture the neural activity [Xu et al., 2020]. Additionally, only local brain activity regions are displayed, and information about how these regions interact during the MI task is omitted. In order to address this limitation, brain connectivities such as correlation [Phang and Ko, 2020], spectral coherence [Li et al., 2022], and phase-lag index [Yang et al., 2022] have been used to quantify the degree of relationship among different brain regions in the frequency and phase domain. However, these methods are also susceptible to various sources of noise and artifacts, such as volume conduction, reference choice, and non-stationarity of the signals [Ruiz-Gómez et al., 2019], which can affect their accuracy and interpretability.

In addition to time-frequency and spatial methods, approaches that directly match brain process patterns and classification performance are used to analyze differences between high and low-performing subjects [Collazos-Huertas et al., 2020]. A classical approach is the CSP technique, which can estimate spatial filters that quantify the degree of separability observed in the neural activity of each channel regarding the MI classes [Naeem et al., 2006]. Nonetheless, CSP has certain limitations, such as the assumption that EEG signals are stationary, sensitivity to noise, and overfitting when many channels are presented [Mishuhina and Jiang, 2018]. Therefore, DL methods have been proposed as an alternative.

One method is Grad-CAM, which generates a heatmap by using the gradients of the target class concerning the feature maps [Deng et al., 2021]. This heatmap highlights elements of EEG signals that contribute the most to the target class. Another approach is Layer-Wise Relevance Propagation (LRP), which propagates relevance scores backward through the neural network layers to identify which input features are most responsible for the output [Bang and Lee, 2022]. Finally, activation maps can be visualized to gain insights into the network's behavior and identify which features are being learned at each layer [Li and Ruan, 2021]. Class activation-based methods allow quantifying the relevance of each input feature, e.g., the EEG channel and time sample, and propagating each class score of a given trial using backpropagation and data upsampling. Therefore, this method preserves both the relevance of the final score and the dimensions of the input feature [Sturm et al., 2016].

However, the earlier methods often overlooked salient information about the most important frequency bands and the connectivity between different parts of the brain in the context of the MI classification task [García-Murillo et al., 2023]. Consequently, the development of a technique that emphasizes connections among brain regions, specifically those contributing most to MI task discriminability, and seamlessly integrates into any signal processing MI pipeline has the potential to enrich the comprehension of performance variations among subjects in EEG-based BCIs. Figure **1-3** provides a summarized overview of the preceding discussion on interpretation techniques for understanding brain processes.

In the research context at hand, the utilization of ML and DL approaches shows great promise in addressing the issue of ISV. To reduce the low SNR in EEG signals, it is crucial to adopt personalized preprocessing methods that consider the individual differences in noise sources and types. This approach involves sequentially applying SL filtering and ICA methods, with an automatic switching mechanism based on MI-BCI accuracy score. Additionally, by integrating well-established BCI architectures like EEGNet with FC-based regularizers, the problem of ISV can be effectively mitigated. Leveraging the spatial information

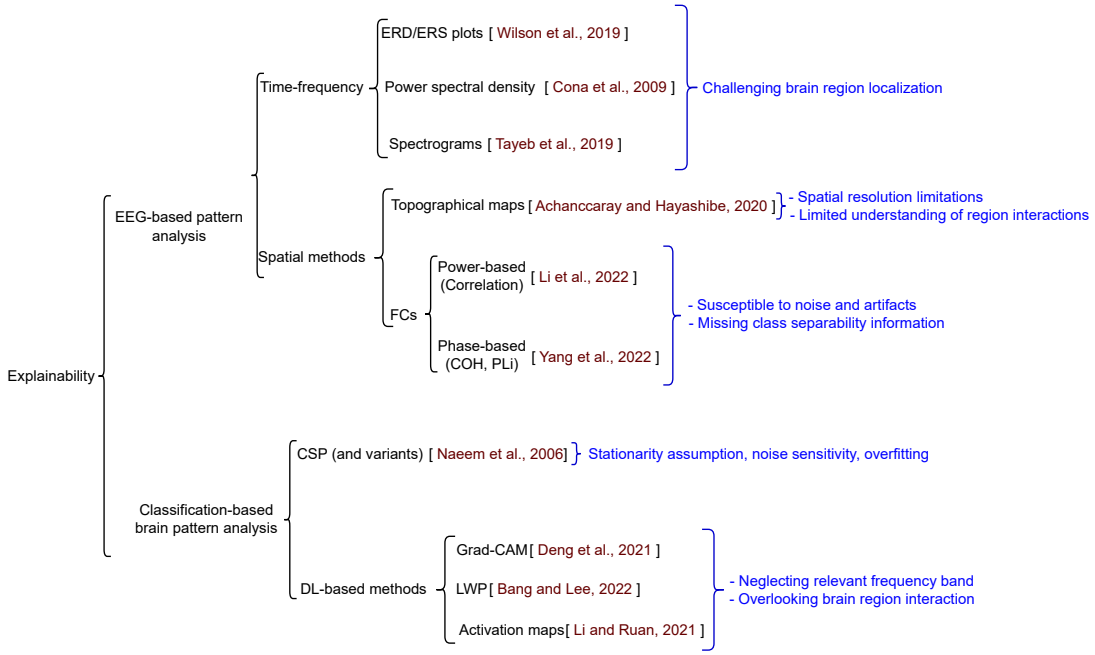

Figure **1-3**. Summary of interpretation techniques for investigating brain processes in the MI task, and their drawbacks highlighted in blue.

provided by FC helps reduce the detrimental effects of overfitting, enabling the network to focus solely on relevant information. Moreover, the use of FC class discriminative methods becomes crucial to address the challenge of interpretability in MI-EEG-based BCIs. These methods facilitate the assessment of differences in brain patterns among subjects, particularly focusing on variations in key connections and channels involved in the MI classification task. These considerations form the foundation of our research objectives. Our primary aim is to explore a subject-dependent preprocessing technique that accounts for subjects' differences in noise level and type. Additionally, we aim to develop a regularized version of EEGNet to reduce the overfitting effect. Lastly, we aim to investigate FC-based methods for evaluating differences in brain patterns among subjects, contributing to the overall interpretability of MI-EEG-based BCIs.

1.4 Aims

1.4.1 General aim

To develop a machine learning framework that incorporates classical ML and DL approaches to support multi-channel time series classification in MI-BCI systems, handling inter-subject variability with preserved interpretability.

1.4.2 Specific aims

- To develop a subject-dependent preprocessing approach for multi-channel MI discrimination that accounts for individual noise levels and type differences among subjects such that the ISV effect is reduced.

- To build an end-to-end deep learning model that effectively deals with the ISV effect.

- To develop an interpretability strategy that allows visualizing salient spatial patterns to support multi-channel EEG-based MI systems.

1.5 Outline and contributions

Below, provide a brief introduction to the primary contributions of this master's thesis. They are summarized in Figure 1-4

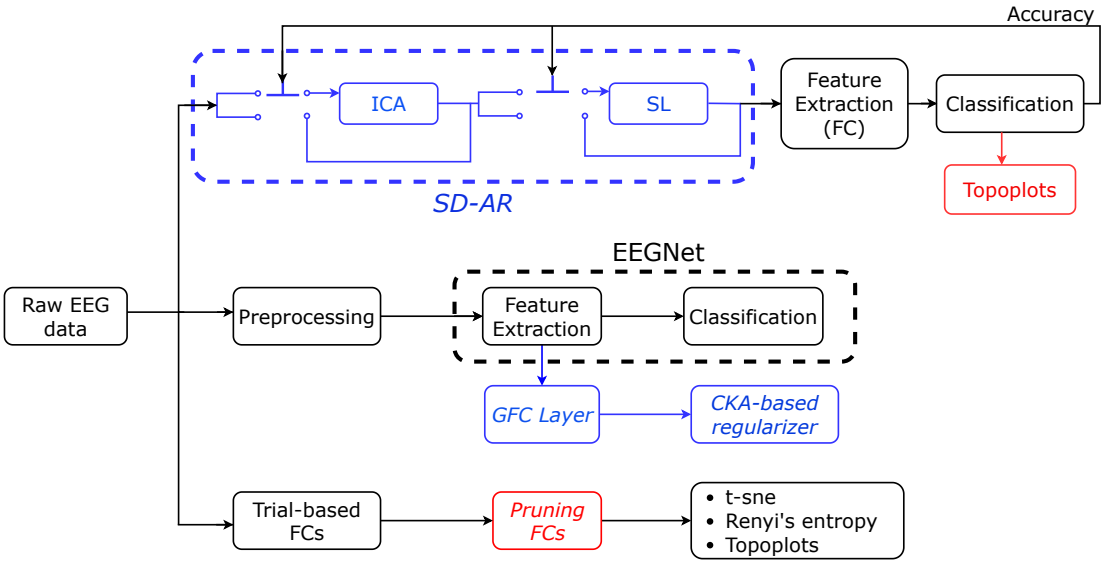

Figure **1-4**. Schematic diagram illustrating the proposed solutions for the ISV and explainability problems addressed in this thesis to support multi-channel time series classification in BCI systems with preserved interpretability. Blue boxes represent the solutions for the ISV problem, while the red boxes represent the solutions for the explainability problem. Each branch is dedicated to an specific objective. GFC stands for Gaussian Functional Connectivity (GFC)

1.5.1 Subject-dependent artifact removal

A low SNR in EEG signals often affects the performance of MI classifiers, which can obscure MI patterns and lead to decreased classification accuracy. Furthermore, it is essential to note that each subject can exhibit different levels and types of noise, resulting in a variable performance among individuals and contributing to the issue of ISV.

To address this challenge, we propose a subject-dependent preprocessing approach in Chapter 2 that reduces the low SNR phenomenon in poorly performing subjects by selectively removing artifacts based on the accuracy obtained upon individual subjects. Specifically, we utilize two preprocessing methods: ICA [Rashid et al., 2020] and SL [Xu et al., 2018], to remove artifacts related to Electrooculography (EOG) signals and the volume conduction effect, respectively. Furthermore, by selectively

applying these preprocessing techniques, we aim to reduce the variability among subjects' performance, emphasizing boosting the performance of bad-performing subjects. Additionally, we utilized various methods to investigate differences in brain patterns among subjects, clustering them based on their MI classification performance. This analysis provides insight into the variability among subjects and informs further improvements to our preprocessing and classification methods.

1.5.2 Kernel-based Regularized EEGNet using Centered Alignment and Gaussian Connectivity for Motor Imagery Discrimination

DL models have shown promising results in performing MI tasks. However, various factors, such as the amount and quality of EEG signals, which can differ across subjects, can hinder the model's performance. In addition, the limitations in the EEG signals can cause models to overfit the training data, leading to poor generalization in new samples and ultimately contributing to the ISV phenomenon.

To address this issue, we proposed a regularizer in Chapter 3 based on the well-known Centered Kernel Alignment (CKA) method [Wang et al., 2015b]. This regularizer encodes the information of graph-structured data, which is computed as FCs using the GFC approach [García-Murillo et al., 2021]. Additionally, we implemented a GFC layer that computes the graphs in a data-driven way and can be directly coupled into an end-to-end DL model. Specifically, we utilized the EEGNet [Lawhern et al., 2018] network as the backbone for our implementation. This approach aims to reduce the effect of overfitting, improves the performance of all subjects, and reduces the variability among them, boosting the performance of low-performing subjects.

1.5.3 FC and Kolmogorov-Smirnov Test-based method to understand differences among MI task performers

Although DL models have demonstrated impressive classification performance in MI tasks, their complexity can obscure the underlying decision-making processes and the factors influencing the performance of both high- and low-performing subjects. In Chapter 4, we propose a novel method based on FCs [Hamedi et al., 2016] and the Kolmogorov-Smirnov [Berger and Zhou, 2014] test to explore differences in brain processes among subjects with varying performance levels. Our method represents each subject as an undirected weighted graph, highlighting the most discriminative FC links. Analyzing these graphs helps identify the brain regions and connections most relevant to the MI task and provides insights into the differences between good- and poor-performing subjects.

1.6 EEG datasets

We used two established datasets in MI to evaluate our proposals: BCI Competition IV dataset 2a (DBI) [Brunner et al., 2008] and Giga (DBII) [Cho et al., 2017]. We created a classification pipeline for each proposal using traditional ML or DL techniques and evaluated its effectiveness based on performance and visual interpretability. We also extracted relevant features or interpreted models by FCs for each proposal.

1.6.1 DBI

The BCI Competition 2008 - Graz Dataset 2a is a publicly available collection that can be accessed at `http://www.bbci.de/competition/iv/index.html` (accessed on April 1st, 2023). The dataset contains EEG data from $M = 9$ subjects that were acquired in two sessions on different days, using a MI paradigm consisting of four

MI tasks: imagining the movement of the left hand, the right hand, both feet, or the tongue. Each session consisted of six runs, and each run included 48 trials, with 12 trials for each of the four possible tasks. Therefore, each session contained $N = 288$ trials, and the entire dataset contained 576 trials per subject in the two recording sessions.

During each trial, a short acoustic warning and a cross on a black screen indicated the beginning of the trial, which lasted for $T = 7$ seconds. At 2 seconds, a visual cue appeared on the screen for 1.25 seconds, consisting of an arrow pointing left, right, down, or up, corresponding to one of the four MI tasks. The cue instructed the subject to perform the indicated MI task until the cross had disappeared from the screen after 6 seconds. After each trial, a short break followed, and the screen went black.

The EEG data were recorded using a 22-channel montage with Ag/AgCl electrodes based on the 10/20 system ($C = 22$). In addition, three electrooculogram (ERD/ERS) electrodes were used to record ocular artifacts. Both EEG and ERD/ERS signals were sampled at a rate of 250 Hz and bandpass-filtered between 0.5 and 100 Hz. A Notch filter at 50 Hz was also applied. The datasets for each subject and session were stored in the General Data Format (GDF) for biomedical signals using one file per subject and session.

1.6.2 DBII

The Giga dataset is publicly available at `http://gigadb.org/dataset/100295` (accessed on 1 April 2023), and it consists of EEG data from 52 healthy subjects, out of which only $M = 50$ are usable for evaluation. The data were acquired in one session according to the BCI experimental paradigm of MI with two classes, left and right hands. Each session consisted of five or six runs, each performing 100 or 120 trials per class. Each trial lasted for $T = 7\,s$ and began with a black screen containing a fixation cross for $2\,s$. Subsequently, a cue instruction appeared randomly on the

screen within $3\,s$, prompting the subject to perform the indicated MI task. Finally, a blank screen appeared, followed by a break of 4.1 to $4.8\,s$.

The EEG data were collected using a Biosemi ActiveTwo system with $C = 64$ Ag/AgCl electrodes placed according to the 10/10 international system. The subjects' signals were sampled at $512\,Hz$ and stored in (`*.mat`) format.

In addition to the MI recordings, real left-hand and right-hand movements were also collected, along with six types of noise, including blinking eyes, eyeball movement up/down, eyeball movement left/right, head movement, jaw clenching, and resting state.

Figure **1-5** provides an overview of the DBI (four-class problem) and DBII (binary problem) montage and paradigm used for MI classification.

1.7 Thesis structure

The thesis is structured as follows: Chapter 2 presents a subject-dependent preprocessing schema to enhance the low SNR in EEG signals and reduce variability among subjects' performance. Chapter 3 focuses on developing a regularizer based on the CKA method that operates over FC-structured data to reduce overfitting in end-to-end DL models for performing MI tasks. In Chapter 4, we propose a novel approach that utilizes FCs and the Kolmogorov-Smirnov test to explore differences in brain processes among subjects with varying performance levels. Finally, Chapter 5 concludes the thesis by summarizing the main contributions, discussing possible directions for future work, and providing a list of academic products associated with this thesis.

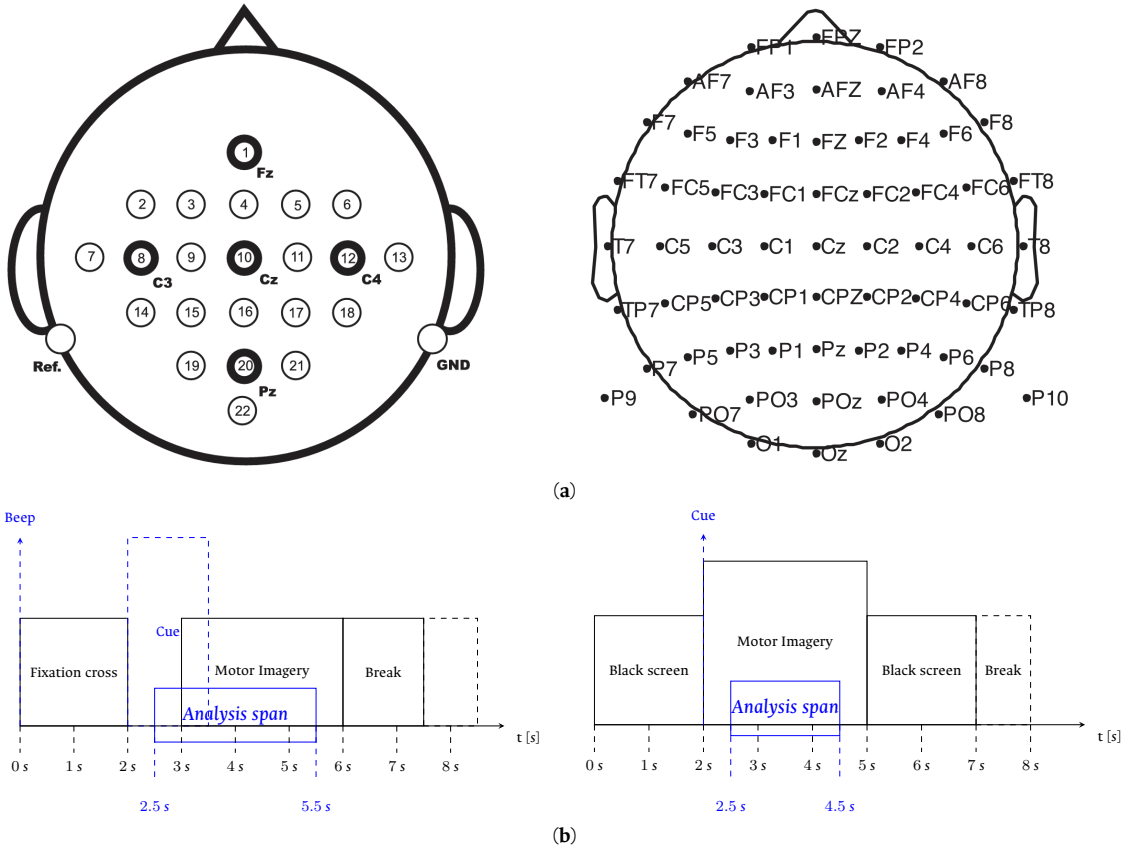

Figure **1-5**. The EEG MI databases examined were DBI (BCI Competition four-class task) and DBII (GigaScience binary task), displayed in the left and right columns, respectively. The top row shows the EEG montages, while the bottom row presents tested MI paradigm.

CHAPTER

TWO

SUBJECT-DEPENDENT ARTIFACT REMOVAL

This chapter presents an innovative approach for subject-dependent preprocessing to mitigate the low SNR phenomenon observed in subjects who fail when performing MI tasks. Our method selectively removes artifacts while performing feature extraction using FC measures. The evaluation of our proposed *SD-AR* approach demonstrates improvements in the performance of the MI classifier for subjects with poor motor skills.

The approach focuses on addressing two common artifacts in EEG data, namely Electrooculogram (EOG) artifacts and volume conduction effects, both of which can distort the extraction of feature sets and severely degrade the classifier's performance in MI tasks. Existing techniques such as SL and ICA have been commonly employed for artifact removal. However, their effectiveness is limited in cases of low SNR, particularly in subjects with poor proficiency in MI tasks.

To tackle this challenge, we introduce a novel approach for Subject-Dependent Artifact Removal (SD-AR), that adaptively applies either SL or ICA based on the

classifier accuracy achieved by each individual. By leveraging subject-specific information, our approach yields superior artifact removal results compared to the traditional preprocessing techniques. Furthermore, the validation results obtained from the datasets described in Section 1.6 indicate that our proposal consistently outperforms existing preprocessing methods in all evaluated scenarios for artifact removal.

Although both SL and ICA do not require subject-specific parameter tuning, their effectiveness is enhanced as the dimensions of the EEG montage increases. Additionally, subjects are analyzed in groups to gain insights into the variations in brain patterns and analyze the contributions of different brain regions to the MI task. This analysis enables us to understand the interplay among brain regions and identify key regions with a crucial role in MI.

2.1 Methods

In this section, the main mathematical fundamentals of the well-known SL method are given. Then, the ICA technique is described. Finally, we outline our *SD-AR* approach. SD-AR allows building a discriminant preprocessing strategy based on SL filtering and ICA to feed a FC-based feature extraction stage for further classification.

2.1.1 Surface Laplacian Filtering

Let $\boldsymbol{X} \in \mathbb{R}^{C \times T}$ be an EEG signal with $C \in \mathbb{N}, T \in \mathbb{N}$ being the number of channels and time samples, respectively. The SL computes the second spatial derivative of the underlying flow of electrical current produced by brain activity at the electrode $c \in C$ concerning the neighboring scalp potentials $c' \in C,\ c \neq c'$. In practice, the Laplacian

filter of EGG data, denoted as $\boldsymbol{X}_L \in \mathbb{R}^{C\times T}$, is computed as [Carvalhaes and De Barros, 2015]:

$$\boldsymbol{X}_L = \boldsymbol{D}\left(\boldsymbol{X}^\top \boldsymbol{G}_s^{-1} - \boldsymbol{X}^\top \boldsymbol{G}_s^{-1}\mathbf{1}\boldsymbol{G}_s^{-1}/\mathbf{1}\boldsymbol{G}_s^{-1}\mathbf{1}\right)^\top$$

where $\mathbf{1}\in\mathbb{N}^{C\times C}$ is an all-ones matrix, and $\boldsymbol{G}_s = \boldsymbol{G} + \varepsilon\boldsymbol{I}$ is a smoothed version of $\boldsymbol{G}$, $\boldsymbol{I}\in\mathbb{R}^{C\times C}$ is the identity matrix, $\varepsilon\in\mathbb{R}[0,1]$ is a regularization parameter; and $\boldsymbol{G}$ and $\boldsymbol{D}\in\mathbb{R}^{C\times C}$ are weighting matrices with elements defined as:

$$g(c,c') = \frac{1}{4\pi}\sum_{n\in\iota}\frac{\zeta(2n+1)P_n(\text{cosdist}(\boldsymbol{e}_c,\boldsymbol{e}_{c'}))}{(n(n+1))^{\vartheta}} \tag{2-1a}$$

$$d(c,c') = \frac{1}{4\pi}\sum_{n\in\iota}\frac{\zeta(2n+1)P_n(\text{cosdist}(\boldsymbol{e}_c,\boldsymbol{e}_{c'}))}{(n(n+1))^{\vartheta-1}} \tag{2-1b}$$

In the equations above 2-1, P_n is a Legendre Polynomial of order n, $\iota\in\mathbb{N}$ is the highest polynomial order considered, $\vartheta\in\mathbb{R}^+$ is a smoothness constant, $\text{cosdist}(\boldsymbol{e}_c,\boldsymbol{e}_{c'}) = 1 - \|\boldsymbol{e}_c - \boldsymbol{e}_{c'}\|_2^2/2$ is the cosine distance between a pair of electrode positions, and $\boldsymbol{e}_c, \boldsymbol{e}_{c'}\in\mathbb{R}^3[-1,1]$ are the electrode positions normalized to a unit-radius sphere. The notation $\|\cdot\|_2$ stands for ℓ_2-norm distance.

2.1.2 Independent Component Analysis

Brain and artifact sources are assumed to mix linearly in $\boldsymbol{X} = \boldsymbol{O}\boldsymbol{S}$, where $\boldsymbol{O}\in\mathbb{R}^{C\times Q}$ is the mixing matrix and $\boldsymbol{S}\in\mathbb{R}^{Q\times T}$ is the sources' matrix, being $Q\leq C$ the number of sources. Under the assumption that the components are statistically independent and non-Gaussian distributed, the joint estimation of $\hat{\boldsymbol{S}} = \{\hat{\boldsymbol{s}}_q : q\in Q\}$ and $\hat{\boldsymbol{O}} = \{\hat{\boldsymbol{o}}_q : q\in Q\}$ can be performed through the negentropy-based optimizing framework as follows [Kumar and Jayanthi, 2020]:

$$\begin{aligned}\hat{\boldsymbol{o}}_q = \underset{\boldsymbol{o}_q}{\text{argmax}} \quad & \mathcal{L}(\boldsymbol{s}_\nu) - \mathcal{L}(\boldsymbol{o}_q^\top \boldsymbol{X}), \quad \forall q\in Q \\ & \text{s.t.: } \|\boldsymbol{o}_q\|_2 = 1\end{aligned} \tag{2-2}$$

where $\hat{\boldsymbol{o}}_q \in \mathbb{R}^C$ is a column vector of unmixing weights computed for a row source, $\boldsymbol{s}_\nu \sim \mathcal{N}(0,1)$ is a zero-mean, unit-variance Gaussian random variable ($\boldsymbol{s}_\nu \in \mathbb{R}^T$) and $\mathcal{L}(\nu) = \mathbb{E}\{-\log(p(\nu)) : \forall \nu\}$ is the Shannon entropy. The notation $\mathbb{E}\{\forall \nu\}$ stands for expectation operator across a random variable ν.

Consequently, the maximization procedure described above is performed over every $q \in Q$ component. Here, Q is fixed to C, i.e., the number of EEG-montage channels. Therefore, to recover the sources and separate them between brain or artifact signals [Xu, 2021], the unmixing model yields:

$$\hat{\boldsymbol{S}} = \hat{\boldsymbol{O}}^\top \boldsymbol{X}. \tag{2-3}$$

2.1.3 Subject-Dependent Artifact Removal

In the presence of a reference electrooculography signal $\boldsymbol{a}_{q'} \in \mathbb{R}^T$, $q' \in Q'$, we use a pairwise similarity estimate to remove artifacts from the contaminated EEG data by comparing an ICA source with every available reference. Thus, each $\hat{\boldsymbol{s}}_q$ component is rejected or selected according to the following thresholding rule:

$$\tilde{\boldsymbol{s}}_q = \begin{cases} \hat{\boldsymbol{s}}_q, & \frac{\left|\mathbb{E}\left\{(\hat{\boldsymbol{s}}_q - \mu_{\hat{\boldsymbol{s}}_q})(\boldsymbol{a}_{q'} - \mu_{\boldsymbol{a}_{q'}})\right\}\right|}{\sigma_{\hat{\boldsymbol{s}}_q}\sigma_{\boldsymbol{a}_{q'}}} \leq \varrho \\ 0, & \text{Otherwise} \end{cases} \tag{2-4}$$

where $\mu_{\hat{\boldsymbol{s}}_q}, \mu_{\boldsymbol{a}_{q'}}, \sigma_{\hat{\boldsymbol{s}}_q}, \sigma_{\boldsymbol{a}_{q'}} \in \mathbb{R}$ are the values of the mean and standard deviation computed for $\hat{\boldsymbol{s}}_q$ and $\boldsymbol{a}_{q'}$, respectively; and $\varrho \in \mathbb{R}^+$ is the threshold established to remove (above) or select (under) the ICA components. The notation $|\cdot|$ stands for absolute value. Hence, the cleaned signal is reconstructed from the unmixing model in Equation (2-3). That is, $\hat{\boldsymbol{X}} = \hat{\boldsymbol{O}}\tilde{\boldsymbol{S}}$, where $\tilde{\boldsymbol{S}} \in \mathbb{R}^{Q \times T}$ is the selected ICA matrix that removes the most closely ICA sources related to the reference artifacts.

In addition, applying both SL filtering and ICA approaches to EOG-artifact removal and volume conduction effect relies on the principle of a similar influence over the

whole set of individuals. Instead, for subject-dependent effectiveness, we select either method of preprocessing based on the quality attained by each individual. For this purpose, the *SD-AR* approach introduces the selector coefficient, noted as $\eta_m \in \mathbb{N}[0,1,2,3]$, that gets the value according to the following scenarios of maximal accuracy performed by each $m \in M$ subject:

$$\eta_m = \begin{cases} 0, \boldsymbol{X} \\ 1, \hat{\boldsymbol{X}} \\ 2, \boldsymbol{X}_L \\ 3, \hat{\boldsymbol{X}}_L \end{cases} \tag{2-5}$$

where $\hat{\boldsymbol{X}}_L$ denotes the sequential application of both ICA and SL filtering preprocessing procedures.

The classifier performance is computed using FC as the feature extraction method. In particular, the following FC measurements extracted on a trial basis are considered:

- *Power-based connectivity* correlates between couples of electrodes over time found on power fluctuations. Regarding this FC, the following pairwise measures are evaluated [Shamsi et al., 2021, Stefano-Filho et al., 2017, García-Murillo et al., 2021]:

$$\text{Pearson's Correlation} = \mathbb{E}\left\{(\boldsymbol{x} - \mu_{\boldsymbol{x}})(\boldsymbol{x}' - \mu_{\boldsymbol{x}'})\right\} / \sigma_{\boldsymbol{x}} \sigma_{\boldsymbol{x}'} \tag{2-6a}$$

$$\text{Motifs} = \mathbb{E}\left\{\times \boldsymbol{i}\,(\bar{\boldsymbol{x}}_b = \bar{\boldsymbol{x}}'_b) : \forall b \in B\right\} \tag{2-6b}$$

$$\text{GFC} = \mathbb{E}\left\{\exp(-\|\boldsymbol{x} - \boldsymbol{x}'\|_2^2 / 2\sigma^2)\right\} \tag{2-6c}$$

  where $\boldsymbol{x}, \boldsymbol{x'} \in \mathbb{R}^T$ are the signals captured at a pair of electrodes, $\mu_{\boldsymbol{x}}, \mu_{\boldsymbol{x}'}$, $\sigma_{\boldsymbol{x}}, \sigma_{\boldsymbol{x}'} \in \mathbb{R}$ are the values of mean and standard deviation estimated for $\boldsymbol{x}, \boldsymbol{x'}$, respectively; $\bar{\boldsymbol{x}}, \bar{\boldsymbol{x}}'$ are the motifs series calculated using the synchronization method (each one lasting $B \leq T$), $\times \boldsymbol{i}\,(\bar{\boldsymbol{x}}_b = \bar{\boldsymbol{x}}'_b)$ is the vector of coincidences between the motif series' elements; and $\sigma \in \mathbb{R}^+$ is the kernel bandwidth needed for GFC.

- FC based on *Phase Coupling* between two electrodes. The following measures are evaluated [Billinger et al., 2013, Benzy et al., 2020]:

$$\text{Spectral Coherence (COH)} = \frac{|\mathbb{E}\{\Xi_{xx'}\}|}{\sqrt{\mathbb{E}\{\Xi_{xx}\}\,\mathbb{E}\{\Xi_{x'x'}\}}} \tag{2-7a}$$

$$\text{Phase-Locking Value (PLV)} = |\mathbb{E}\{\Xi_{xx'}/|\Xi_{xx'}|\}| \tag{2-7b}$$

  where $\Xi_{xx'} \in \mathbb{R}^T$ is the cross-spectral density between $\boldsymbol{x}$ and $\boldsymbol{x}'$; while Ξ_{xx}, $\Xi_{x'x'} \in \mathbb{R}^T$ are the estimates of power spectral density computed for $\boldsymbol{x}$ and $\boldsymbol{x}'$, respectively.

In the above-considered FC measurements, the expectation operator averages across the whole time set of each trial.

2.2 Experimental Set-Up

The proposed methodology of selective preprocessing is based on the well-known methods of SL filtering and ICA. Namely, our SD-AR automatically switches each one of the techniques mentioned above concerning the BCI accuracy score. In this sense, SD-AR aims to improve each subject's classification performance and the interpretability of elicited brain activity responses along groups of subjects with different skills and abilities for MI practice. As shown in Figure 2-1, the tested preprocessing approach appraises the following stages:

(i) Subject-dependent preprocessing for artifact removal (*SD-AR*). According to the highest individual classifier accuracy, removing artifacts over each subject is conducted according to one of the following combinations of the ICA and Laplacian filters in Equation (2-5): both filters, one only, or neither. In applying both filters sequentially, the ICA procedure is first performed before the Laplacian algorithm, as suggested in [Hsu, 2013]. For comparison, two additional cases of preprocessing are also evaluated: (*Ind-AR*) using both filters of artifact subtraction over every individual regardless of his achieved classifier performance, and no removal filtering (*Raw*) of all acquired EEG data.

(ii) Feature Extraction for testing the power-based and phase-based FC measurements. As suggested in [Abhang et al., 2016], the set of EEG signals is band-pass filtered within the following four frequency bandwidths (rhythms): $\{\mu \in [8-12], \beta_l \in [12-15], \beta_m \in [15-20]$, and $\beta_h \in [18-40]\}$ *Hz*. The features are extracted within the time window of post cue onset. That is, $0.5-3.5$ *s* for DBI and $0.5-2.5$ *s* for DBII (see Section 1.6). The feature extraction process is built for each label by the vectorized version of the upper triangular matrix, with size $C \times (C-1)/2$, computed over each trial for each FC measure under evaluation. The obtained super vectors within the four considered rhythms are further concatenated to create a single vector, with size $4C \times (C-1)/2$, which is further used as input to the classifier. Regarding the FC parameters, the following values are specified: The kernel bandwidth in GFC, σ, is fixed as the median averaged over the input distances [Valencia-Marin et al., 2021]; and the degree of motifs is set to 3 while the lag to 1, as suggested in [Rosário et al., 2015].

(iii) Estimating classification performance using a LDA algorithm evaluated through a 10-fold cross-validation strategy over the training set provided for DBI and a simple ten-iteration 20–80% training-testing split for DBII. Of note, DBI provides a predefined testing set, which is used to report the final performance. Note that the preprocessing parameters are tuned at this stage according to the achieved classification performance.

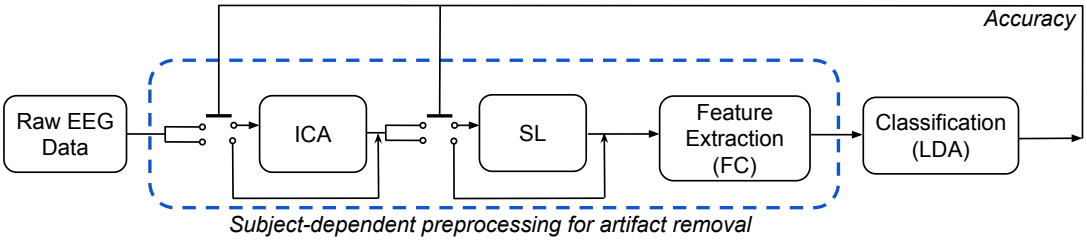

Figure **2-1**. Diagram of the evaluated preprocessing approach to remove the effect of electrooculography and volume conduction. The dashed box highlights the proposed subject-dependent procedure for artifact removal (*SD-AR*) tested in subjects with poor MI skills.

All experiments were carried out in Python 3.8, with the sklearn and MNE libraries, on a Google Collaboratory environment (code repository: https://github.com/mtobonh/SD-AR, accessed on 1 June 2023).

2.2.1 Computation of ICA Decomposition

Initially, a five-order high pass Butterworth filter of $1\,Hz$ is performed to remove low-frequency drifts affecting the quality of the ICA filtering algorithm. In addition, the unmixing matrix $\boldsymbol{O}$ is also orthogonalized via the whitening procedure to improve the accuracy of independent components, which are estimated by a fastICA algorithm (see appendix A). Accordingly, the cost function in Equation (2-2) is approximated as follows [Hyvärinen and Oja, 2000]:

$$\mathcal{L}(\boldsymbol{s}_\nu) - \mathcal{L}(\boldsymbol{o}_q^\top \boldsymbol{X}) \propto \left(\mathbb{E}\left\{-\exp\left(-\left(\boldsymbol{o}_q^\top \boldsymbol{X}\right)^2/2\right)\right\} - \mathbb{E}\left\{-\exp\left(-\boldsymbol{s}_\nu^2/2\right)\right\}\right)^2 \tag{2-8}$$

The source selection is based on the similarity between every ICA source and the electrooculogram available for DBI. Then, the similarity is measured on a trial basis over the whole subject set through the Pearson Correlation value. Since DBII does not provide the EOG data, the similarity with the ICA components is assessed using the three frontal electrodes, as suggested in [Jafarifarmand et al., 2017]. Across the subject set, the correlation values have a Gaussian probability density function, as shown in the right column of Figure **2-2** for either database. Therefore, the rule for source removal is fixed to the 3σ-level computed over the Z-scored values (see red dashed lines). Note that this procedure is twice performed.

As an illustrative example of EOG-removal from the EEG signal, Figure **2-2** shows the channels-noise ratio computed as the median of normalized unmixing matrix weights of sources associated with artifacts. The median value is calculated over the subjects' noisy trials. As seen in both evaluated databases, the ocular artifacts affect the frontal channels because of their proximity to the eyes. However, the

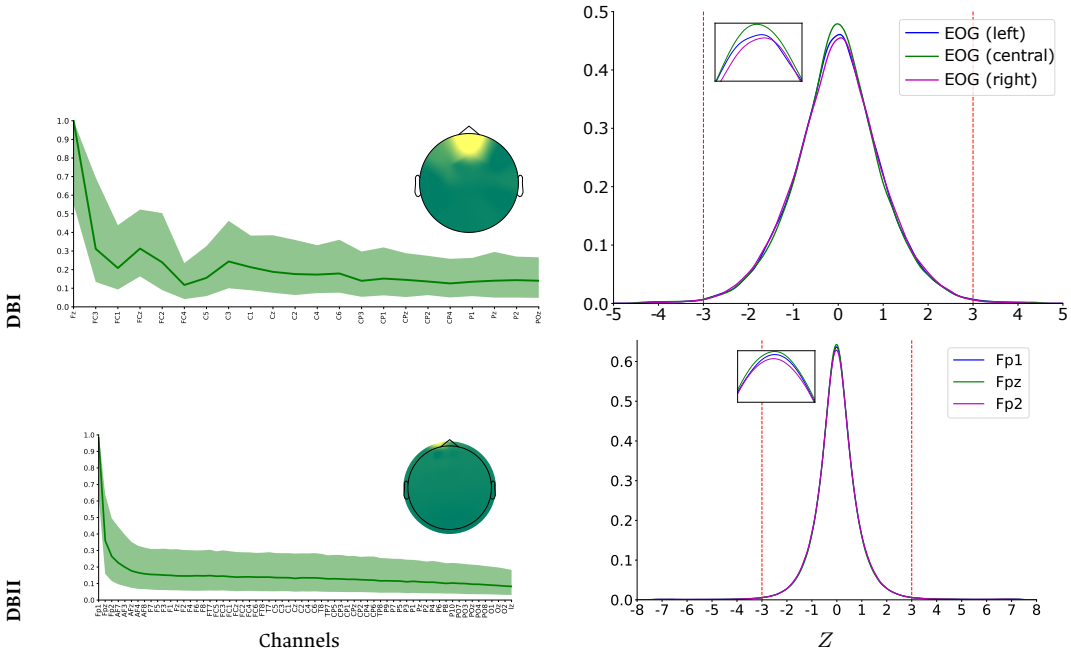

Figure **2-2**. Effect of ICA filtering for EOG removal on both evaluated databases: DBI (**Top row**) and DBII (**bottom row**). Left column: the estimated electrode weights (normalized values are shown) and topograms. Right column: 3σ-level threshold of similarity used for EOG removal.

reconstructed topoplots show that DBI has a larger effect on brain area since the EEG montage holds the third set of electrodes, as does DBII. Moreover, the small montage may produce significant variations in the estimated weights of the electrodes of frontal and centro-parietal areas.

2.2.2 Impact of Surface Laplacian Filtering

The influence of SL Filtering on connectivity measurements is assessed. To this end, we adjust the parameters of the SL filter as suggested in [Cohen, 2014]: the highest Legendre polynomial order o to 10, the smoothing constant ϑ to 4, and the regularization parameter ε to 1×10^{-5}. Further, we conduct the testing methodology developed in [Cohen, 2015] that explores whether the amount of FC estimates

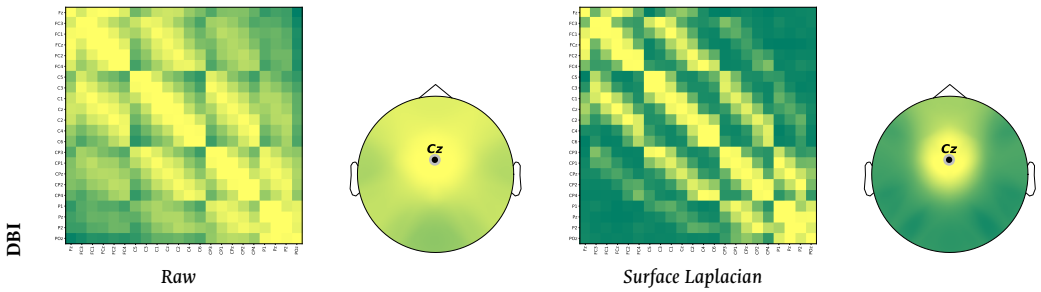

(a) DBI: Effect of SL on FC computation for DBI.

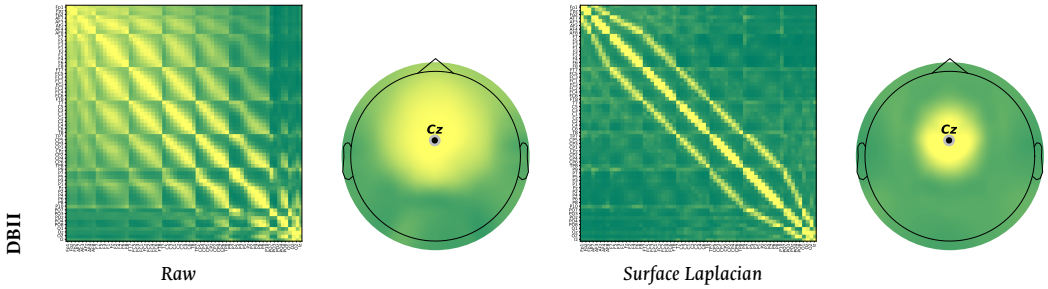

(b) DBII: Effect of SL on FC computation for DBII.

Figure **2-3**. Effect of SL on the FC computation. 2-3a Top row shows the results for DBI. 2-3b Bottom row shows the results for DBII. Spatial FC matrix and the corresponding topoplot calculated without filtering (Left column); after SL filtering (Right column).

decreases after applying the spatial filtering over a specific electrode. Consequently, we check if the number of false links drops due to the field spread effect.

Specifically, the FC between the Cz channel, placed over the sensorimotor area, and the remaining electrodes is examined. For illustration's sake, Figure **2-3** presents the FC matrix extracted using the pairwise Pearson correlation in Equation (2-6a), although other metrics yield similar results. We show the corresponding topogram estimated for the Cz channel along with the FC matrix. Both FC representations are obtained for DBI (**2-3a**) and DBII (**2-3b**) by averaging across the trial and individual sets. As can be seen, the left-side heatmap matrix extracted from the raw data visualizes many more relationships between electrodes so that the resulting topoplots exhibit neural responses spread throughout the scalp surface.

Consequently, the MI rehearsing is masked by a high field spread effect. On the contrary, the SL filter impacts the FCs calculation positively, reducing considerably

the number of links outside the sensorimotor area activated by MI, as shown in the connectivity matrix. Furthermore, the estimated topoplot presents a focused neural activity neighboring the Cz electrode with a reduced amount of spurious connectivities caused by volume conduction. The EEG montage of DBII with a much higher number of electrodes can better illustrate this situation.

2.3 Results and Discussion

By using the FC estimators above-described in Section 2.1.3, the proposed methodology is evaluated in terms of the performance of each feature extraction using the following metrics: Accuracy (ACC), Cohen's Kappa coefficient (kappa), and Area Under the Receiver Operating Characteristics Curve (AUC) [Géron, 2019].

In all performance metrics, we show their testing set values of the mean $\pm$ standard deviation averaged across two different evaluating strategies: (i) Global assessment by averaging over the whole set of individuals; (ii) Group-level assessment by averaging over a concrete category of subjects. Namely, we are interested in evaluating the effectiveness of the suggested preprocessing methodology for enhancing the classifier performance of the so-called inefficient individuals [Park et al., 2021].

2.3.1 Classifier Performance Achieved per Subject

Here, we estimate the performance in three training scenarios for classifying MI tasks: (a) the classifier is fed by EEG data without preprocessing (left column—*Raw*), (b) EEG data after both preprocessing procedures for ICA and SL Filtering (center column—*Ind-AR*), (c) the suggested preprocessing approach that switches either procedure selectively as explained before (right column—*SD-AR*).

Table 2-1 presents the results achieved by the testing set of DBI, for which the best performance values of each estimator are marked in bold. Overall, both power-based

and phase-based connectivity measurements achieve poor results in the four-class classification task of DBI, with the GFC estimator being the best performer. As can be seen, training solely with raw data underperforms the proposal regardless of the FC metric employed. Despite this, *Ind*-AR is the best preprocessing scenario, even though the suggested method gets close results. This weak impact of the proposal may be explained by the fact that the DBI collection faces several troubles during validation: First, the training and testing data distributions differ considerably. Figure 2-4 displays the number of trials strongly affected by artifacts, which have been identified using the ICA-based procedure in the training and testing datasets. As can be observed, there is a high disparity in four subjects (labeled as #2, # 5,# 1, and #3). DBI is a relatively small data set, so four subjects would be more than 40% of the data set. Secondly, the used EEG montage holds a relatively small number of channels, posing a significant restriction for SL procedures, as discussed in [Rathee et al., 2017]. Consequently, validation is adversely affected by all of these issues, resulting in a low classifier performance.

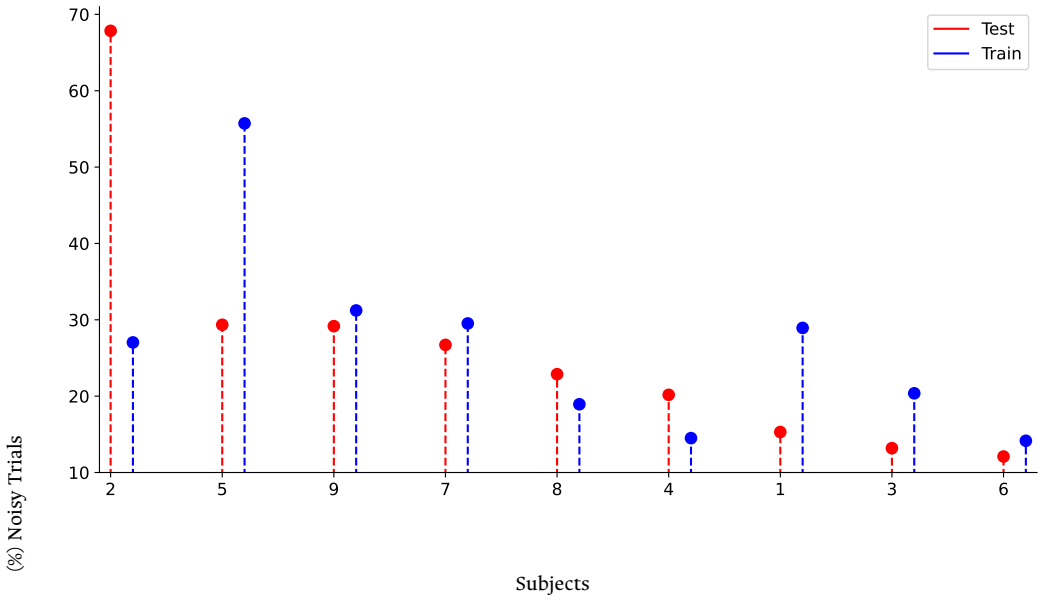

Figure **2-4**. Percentage of noisy trials of each subject identified by the ICA-based artifact removal strategy in the training and testing stage of DBI.

Table 2-2 displays the resulting performance obtained through a 10-fold

Table **2-1**. Performance of each FC measure in DBI for each of the training classifier scenarios. The last row shows the performance values averaged over the whole subject set and across the evaluated FC measures. The notation Pearson stands for Pearson's correlation. Bold stands for the best results.

FC	***Raw***	***Ind*-AR**	***SD*-AR**
	ACC Kappa AUC	ACC Kappa AUC	ACC Kappa AUC
PLV	44.9 ± 8.8 0.27 ± 0.12 0.72 ± 0.09	$\mathbf{53.3 \pm 11.9}$ $\mathbf{0.38 \pm 0.16}$ $\mathbf{0.77 \pm 0.10}$	51.1 ± 12.9 0.35 ± 0.17 0.76 ± 0.11
COH	53.6 ± 12.4 0.38 ± 0.17 0.78 ± 0.10	$\mathbf{57.9 \pm 11.3}$ $\mathbf{0.44 \pm 0.15}$ $\mathbf{0.80 \pm 0.09}$	55.8 ± 12.6 0.41 ± 0.17 0.79 ± 0.09
Pearson	54.6 ± 12.4 0.39 ± 0.17 0.79 ± 0.10	$\mathbf{57.4 \pm 11.8}$ $\mathbf{0.43 \pm 0.16}$ $\mathbf{0.81 \pm 0.09}$	57.2 ± 11.7 $\mathbf{0.43 \pm 0.16}$ $\mathbf{0.81 \pm 0.09}$
Motifs	48.6 ± 9.8 0.32 ± 0.13 0.75 ± 0.09	$\mathbf{55.4 \pm 12.0}$ $\mathbf{0.41 \pm 0.16}$ $\mathbf{0.80 \pm 0.10}$	53.8 ± 13.2 0.38 ± 0.18 0.79 ± 0.10
GFC	62.9 ± 11.6 0.51 ± 0.15 $\mathbf{0.85 \pm 0.09}$	$\mathbf{64.4 \pm 11.9}$ $\mathbf{0.53 \pm 0.16}$ $\mathbf{0.85 \pm 0.09}$	63.5 ± 11.4 0.51 ± 0.15 $\mathbf{0.85 \pm 0.09}$
Average	52.9 ± 12.6 0.37 ± 0.17 0.78 ± 0.10	$\mathbf{57.7 \pm 12.4}$ $\mathbf{0.44 \pm 0.16}$ $\mathbf{0.81 \pm 0.09}$	56.3 ± 13.1 0.42 ± 0.17 0.80 ± 0.19

cross-validation scheme, as commonly validated for DBII [Collazos-Huertas et al., 2021b]. Unfortunately, as shown in the central column, both approaches (i.e., *Ind*-AR) result in the worse bi-class classification scenario and harm average over all individuals rather than improving the performance, as expected. This effect is contrary to the case for subject-dependent preprocessing, which improves classifier performance for all FC metrics considered (see right column). A noteworthy fact is that the mean values of performance achieved by the power-based FC estimators

Table **2-2**. Performance of each FC measure in DBII for each of the training classifier scenarios. The last row shows the performance values averaged over the whole subject set and across the evaluated FC measures. Bold stands for the best results.

FC	***Raw***	***Ind*-AR**	***SD*-AR**
	ACC Kappa AUC	ACC Kappa AUC	ACC Kappa AUC
PLV	62.1 ± 9.7 0.24 ± 0.19 0.62 ± 0.10	61.8 ± 12.8 0.23 ± 0.26 0.61 ± 0.13	$\mathbf{66.7 \pm 11.4}$ $\mathbf{0.33 \pm 0.23}$ $\mathbf{0.67 \pm 0.11}$
COH	64.0 ± 9.4 0.28 ± 0.19 0.64 ± 0.09	63.2 ± 11.3 0.26 ± 0.23 0.63 ± 0.11	$\mathbf{67.6 \pm 10.6}$ $\mathbf{0.35 \pm 0.21}$ $\mathbf{0.67 \pm 0.11}$
Pearson	65.0 ± 10.5 0.30 ± 0.21 0.65 ± 0.11	63.9 ± 12.0 0.27 ± 0.24 0.63 ± 0.12	$\mathbf{68.4 \pm 11.1}$ $\mathbf{0.36 \pm 0.22}$ $\mathbf{0.68 \pm 0.11}$
Motifs	64.5 ± 10.4 0.29 ± 0.21 0.64 ± 0.10	63.7 ± 12.5 0.27 ± 0.26 0.63 ± 0.13	$\mathbf{68.3 \pm 11.6}$ $\mathbf{0.36 \pm 0.23}$ $\mathbf{0.68 \pm 0.12}$
GFC	70.2 ± 11.9 0.40 ± 0.24 0.70 ± 0.12	70.6 ± 12.3 0.41 ± 0.25 0.70 ± 0.12	$\mathbf{73.4 \pm 11.6}$ $\mathbf{0.47 \pm 0.23}$ $\mathbf{0.73 \pm 0.12}$
Average	65.2 ± 10.8 0.30 ± 0.22 0.65 ± 0.11	64.6 ± 12.6 0.29 ± 0.25 0.64 ± 0.13	$\mathbf{68.9 \pm 11.5}$ $\mathbf{0.37 \pm 0.23}$ $\mathbf{0.69 \pm 0.12}$

outperform the corresponding phase-based metrics. As a result, GFC yields the best mean estimates of all feature extraction methods, while PLV comes in last.

2.3.2 Enhanced Performance of Individuals with Poor Skills

Next, the impact of the proposed *SD-AR* preprocessing on the subjects who performed the MI task the worst is assessed. Given the superior performance of the GFC measure (refer to Table 2-2), the impact analysis specifically utilized this FC and was limited to the DBII collection, involving more individuals to ensure statistically significant results.

By analyzing each performance measure (ACC, kappa, and AUC) individually, we cluster the distinctiveness in terms of the variability between subjects. Concretely, clustering is carried out based on the classifier measures through the k-means algorithm (see appendix B), fixing the number of partitions to three, as commonly adjusted [Velasquez-Martinez et al., 2020a]. For evaluation purposes, the k-means algorithm is fitted with the performance criteria estimated for the feature set without processing (i.e., *Raw* scenario).

According to the considered training scenarios of MI classification, the classifier performances (mean and variance values) are grouped into the following three partitions of skills in practicing MI tasks (see Figure 2-5), as also recommended in [Zhang et al., 2020]: (G I) Group of individuals achieving the most consistent performance with very low variability of neural responses (colored in green). (G II) Group with performance exceeding 70% [Cho et al., 2017], containing some response fluctuations (yellow color). (G III) Group producing modest performance and a high unevenness of responses (red color). Figure 2-5a displays the resulting accuracy obtained by each training scenario. For the aim of assessing the gain in performance, the individuals are sorted based on the accuracy estimated by the LDA algorithm for the *Raw* training scenario. Moreover, Figure 2-5b shows the resulting partitions of MI skills. As can be observed, the baseline scenario results in the smallest number of best-performing subjects (11). At the same time, this training with raw data yields the highest number of worse-performing individuals (21) that comprises more than

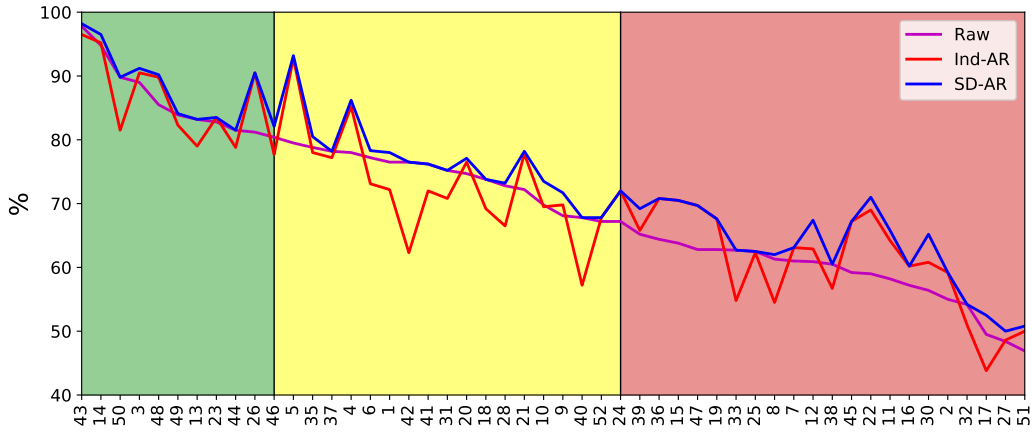

(a) LDA-based Accuracy of MI tasks.

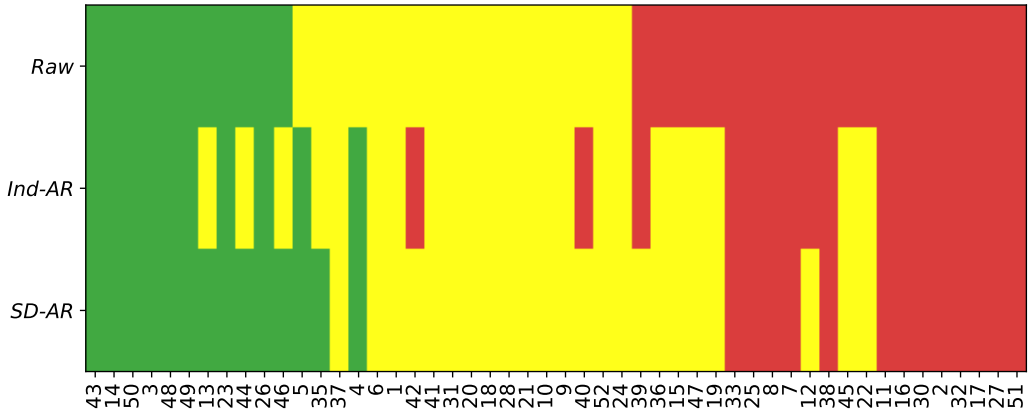

(b) Resulting partitions of MI skills.

Figure **2-5**. Clustering variability of individuals that belong to G I (cells in green), G II (yellow), and G III (red), depending on the preprocessing strategy.

40% of the subjects set. MI training under these conditions becomes very ineffective and costly to implement [Dagdevir and Tokmakci, 2021]. Afterward, the *Ind-AR* scenario delivers even fewer best-performing subjects (10) while reducing the worse-performing set by upgrading six individuals. Nonetheless, some subjects are severely downgraded, as it is the case for #42 and #40.

Lastly, the proposed *SD-AR* approach results in the largest best-performing set (14) while providing the smallest number of individuals with poor skills (13). In other words, *SD-AR* reduces the group of poor-performing individuals from 40% to 25%.

Table **2-3**. The resulting performance of each training classifier scenario obtained by GFC for each considered group of skills in practicing the MI tasks. Bold stands for the best results.

FC	***Raw***	***Ind*-AR**	***SD*-AR**
	ACC kappa AUC	ACC kappa AUC	ACC kappa AUC
G I	86.4 ± 5.50 0.73 ± 0.11 0.86 ± 0.06	85.9 ± 6.50 0.72 ± 0.13 0.86 ± 0.06	$\mathbf{88.3 \pm 5.50}$ $\mathbf{0.76 \pm 0.11}$ $\mathbf{0.88 \pm 0.05}$
G II	73.9 ± 4.10 0.47 ± 0.08 0.74 ± 0.04	72.8 ± 7.80 0.45 ± 0.16 0.72 ± 0.08	$\mathbf{76.5 \pm 5.90}$ $\mathbf{0.52 \pm 0.12}$ $\mathbf{0.76 \pm 0.06}$
G III	58.7 ± 5.10 0.17 ± 0.10 0.58 ± 0.05	60.6 ± 7.60 0.21 ± 0.15 0.61 ± 0.08	$\mathbf{63.0 \pm 6.40}$ $\mathbf{0.26 \pm 0.13}$ $\mathbf{0.63 \pm 0.07}$

Another aspect to highlight is that *SD*-AR does not downgrade individuals compared with the other training scenarios.

Table 2-3 summarizes the classification measures computed per each group, showing once more that *SD*-AR overperforms in all scenarios of preprocessing evaluated for artifact removal. *SD*-AR has also performed better than the average achieved by *Ind*-AR for all individuals.

2.3.3 Improved Interpretability of Elicited MI Responses

As part of the proposed *SD*-AR approach, we will consider the enhanced interpretability of GFC extraction to decode the brain neural responses elicited by MI paradigms. Here, we compute the topoplots based on the absolute value of individual LDA coefficients estimated within all four bandwidths and normalized between $[0, 1]$. In this context, the absolute value of LDA coefficients is a measure of

the relevance of discriminating between MI tasks, i.e., the larger the coefficient, the higher the contribution provided by the extracted FC set. Thus, to compute the relevance of each individual, we first build a supervector by concatenating all ravel versions of the LDA-based discriminant weights concerning the upper triangular GFC feature matrix. Concatenation integrates all four rhythms and produces a vector of size $4C \times (C-1)/2$. Nevertheless, since unsplit versions of μ and β are conventionally explained, the three subbands of the latter rhythm are merged into one plot using the maximum operator. Then, the newly recomputed relevance weight vector has a dimension of $C \times (C-1)$.

Afterward, we compute the group-level GFC representation by joining the relevance-weight vectors estimated for all M_i individuals belonging to each i-th subset of MI skills (i.e., G I, G II, and G III), yielding a matrix with dimension $M_i \times C(C-1)$, being M_i the number of subjects in i-th subset. The group-level relevance GFC matrix summarizes the joint contribution, from which the maximum value in each column (that is, per individual) becomes the connectivity link having the most significant contribution to discriminating between MI tasks.

Figure **2-6** displays the topoplots that reveal the estimated spatial relevance for μ and β rhythms. As can be seen, the fast changes of β enable a higher discriminating ability of neural responses than the μ band. Still, the assessed contribution of the elicited neural responses depends on the evaluated scenario of classifier training. Thus, the case of no removal filtering leads to brain β responses with background activity spreading the sensory-motor and occipital regions. However, the number of relevant GFC links decreases as the group performance of subjects also worsens. With both artifact subtraction filters applied across the entire group of individuals, significantly more β activity spreads across the scalp, overextending the sensory-motor cortex and including the brain activity coming from occipital and temporal lobes. Both regions are not supposed to contribute to the MI paradigm, and this activation may explain the reduced classification performance of *Ind-Ar* among the evaluated training scenarios. Regarding the proposed *SD-AR* approach, the discriminating neural responses are the most localized within the premotor and motor cortex.

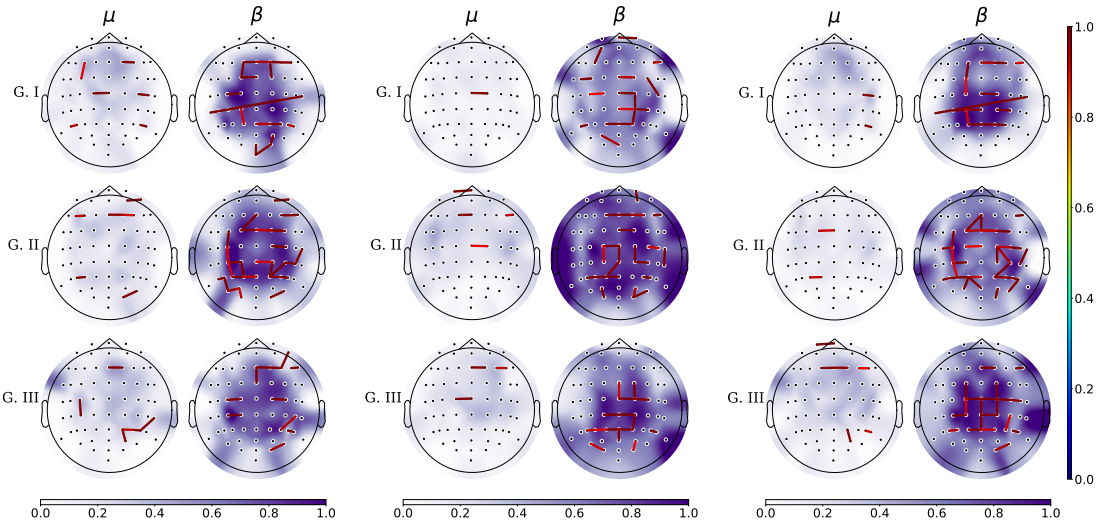

(a) *Raw* (b) *Ind-AR* (c) *SD-AR*

Figure **2-6**. Topoplots show the GFC's spatial relevance for each considered group of skill partition. The GFC links only exceeding relevance weight values of 0.9 are depicted. The strength values over each electrode estimate the background activity elicited by MI responses.

Therefore, the classifier is more accurate since more contributing GFC relationships are evaluated.

Furthermore, to decrease training efforts and encourage user-centered MI responses, the neurophysiological explanation of spatial patterns generated is enhanced by *SD-AR*. In particular, the estimated topoplots show that in comparison with the μ rhythm, β waveforms having a faster behavior benefit more from the artifact removal of the electrooculography and volume conduction effect. Consequently, the discriminating neural responses estimated by *SD-AR* are the most localized within the premotor and motor cortex, as expected in MI paradigms. To illustrate this finding, Figure **2-7** compares the corresponding plots of both rhythms estimated for the subject labeled as # `sbj45` that is included by the *Raw* training scenario in the worst-performing group. After applying *SD-AR*, this subject achieves a high gain in classification accuracy (more than 8%) so that he is newly incorporated into G II with adequate performance. As can be observed, the brain neural activity of β is now localized mainly in the sensorimotor area.

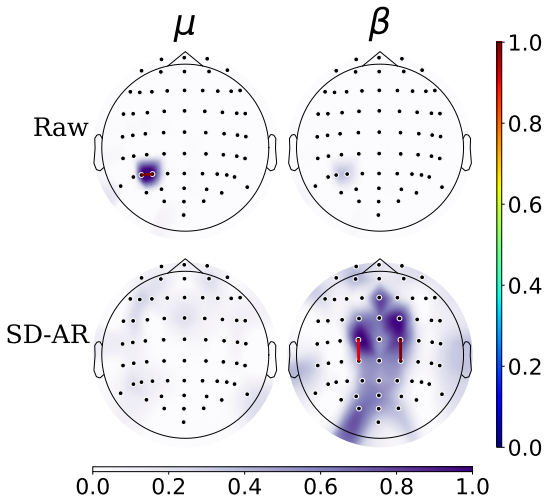

Figure **2-7**. Topographical maps of # `sbj45` with poor skills, having a high gain in classification accuracy provided by *SD-AR*.

2.3.4 Comparison of Results for Motor Imagery Classification Methods

The suggested preprocessing approach entails FC measures for feature extraction that encode most meaningful relationships of elicited brain neural responses between electrodes to tackle better MI tasks performed by poor-performing subjects. Several widely known power-based and phase-based methods of FC are tested, showing that subject-dependent preprocessing improves the classifier's performance, with GFC being the most accurate. As a result, compared with several state-of-the-art methods recently reported for classification of MI tasks, Table **2-4** shows that the proposed *SD-AR* approach achieves a competitive classification accuracy for both EEG databases. In addition, the *SD-AR* approach decreases the group of poor-performing individuals, improving the use of MI paradigms. Still, the validation of DBII reveals that very few subjects may not benefit from the suggested subject-dependent preprocessing for artifact removal.

Table **2-4**. Comparing the *SD-AR* classification accuracy of MI tasks with existing state-of-the-art methods reported for DBI (four classes) and DBII (bi-class). Bold stands for the best results.

	Method	Accuracy [%]
DBI	STR [Rodrigues et al., 2019]	49.2 ± 15.6
	MCSP+SRSG-FasArt [Jafarifarmand and Badamchizadeh, 2020]	62.7 ± 15.9
	3DCNN [Wei and Lin, 2020]	64.9 ± 7.5
	EEGNet [Lawhern et al., 2018, Jeong et al., 2021]	67.3 ± 15.7
	SD-AR	$\mathbf{63.5 \pm 11.4}$
DBII	FBCSP [Ang et al., 2008, Ko et al., 2021]	68.0 ± 15.0
	EEGNet [Lawhern et al., 2018, Ko et al., 2021]	64.0 ± 7.0
	RSTNN [Ko et al., 2018, Ko et al., 2021]	69.0 ± 12.0
	Optical+ [Kumar et al., 2021]	69.6 ± 16.3
	SD-AR	$\mathbf{73.4 \pm 11.6}$

2.4 Summary and Discussion

In this chapter, an approach for *SD-AR* has been proposed to effectively address the issue of low SNR in EEG signals. This issue leads to variations in subjects' performance during the MI task. The approach focused on selectively removing artifacts based on the individual classifier accuracy, tailoring the artifact removal process to the specific needs of each subject. Two preprocessing methods, ICA and SL, were employed. ICA was used to eliminate artifacts associated with EOG signals, while SL addressed the volume conduction effect.

Unlike conventional techniques that primarily rely on commonly-used spatial patterns to extract event-related desynchronization features, our approach explored a range of FC measures across spatially-distributed regions. These measures enabled us to extract MI features to evaluate the differences in subjects' performance based on the relevance of connectivity within specific brain regions for the MI task.

To evaluate the effectiveness of our *SD-AR* approach, experiments were conducted using the datasets described in Section 1.6. The results demonstrated its remarkable

capability to mitigate the impact of artifacts to reduce intertrial/inter-subject amplitude variability. Consequently, the classifier's performance was improved, and the interpretability of the results was improved, particularly for subjects with poor MI skills.

CHAPTER

THREE

KERNEL-BASED REGULARIZED EEGNET USING CENTERED ALIGNMENT AND GAUSSIAN CONNECTIVITY FOR MOTOR IMAGERY DISCRIMINATION

This chapter introduces a novel regularizer designed to tackle the issue of overfitting in end-to-end DL models employed for MI tasks. Overfitting can significantly affect model performance, particularly in subjects with high levels of noise and brain pattern variability, leading to degraded results. Our regularizer aims to mitigate overfitting by guiding DL architectures to focus on intrinsic MI patterns while reducing the influence of noise in EEG signals.

The proposed regularizer is built upon the well-established CKA method and leverages information from EEG signals about FCs. FCs are computed using a data-driven GFC layer seamlessly integrated into the end-to-end DL architecture. The GFC layer functions as a filter, effectively removing spurious connectivities from noise channels while preserving those associated with relevant MI activity. This approach enhances the feature representation of EEG signals and significantly

improves performance in the MI task, particularly for subjects who struggle with their performance.

In evaluating the proposal, the EEGNet architecture was chosen as the baseline. The MI performance of the raw EEGNet model was subsequently compared with the Kernel-based Regularized EEGNe (KREEGNet) on the datasets outlined in Section 1.6. The results demonstrated a notable overall improvement in the MI performance of our regularized approach. Moreover, our regularizer reduced performance variability among subjects and yielded significant benefits for those with poor initial performance.

In addition to evaluating performance, we conducted a comprehensive hyperparameter analysis to investigate the relationship between hyperparameters, performance, and noise levels. This analysis provided valuable insights into the impact of hyperparameter settings on model performance, further validating the effectiveness of our regularizer. Furthermore, we compared our KREEGNet model against other renowned DL architectures regarding MI classification performance. The results consistently demonstrated the superiority of our proposed method, reinforcing its efficacy in addressing the challenge of overfitting in MI tasks.

3.1 Methods

3.1.1 Centered Kernel Alignment Fundamentals

Let $X \subset \mathcal{X}, Y \subset \mathcal{Y}$ be a pair of random variables holding samples $x \in X$ and $y \in Y$, respectively. The kernels $\kappa_X : \mathcal{X} \times \mathcal{X} \to \mathbb{R}$ and $\kappa_Y : \mathcal{Y} \times \mathcal{Y} \to \mathbb{R}$ can be defined to code nonlinear relationships among samples from positive definite functions, yielding:

$$\kappa_X(x, x') = \langle \phi_X(x), \phi_X(x') \rangle_{\mathcal{H}_X}, \tag{3-1}$$

$$\kappa_Y(y, y') = \langle \phi_Y(y), \phi_Y(y') \rangle_{\mathcal{H}_Y}, \tag{3-2}$$

where $\phi_X : \mathcal{X} \to \mathcal{H}_X$ and $\phi_Y : \mathcal{Y} \to \mathcal{H}_Y$, being $\mathcal{H}_X$ and $\mathcal{H}_Y$ the resulting Reproducing Kernel Hilbert Spaces (RKHS). Hence, the statistical alignment between κ_X and κ_Y, $\rho_{CKA}(X, Y) \in [0, 1]$, referred to as Centered Kernel Alignment (CKA), is calculated by taking the normalized inner product between them and averaging it across all pairs of realizations, as shown below [Cortes et al., 2012, Álvarez-Meza et al., 2017]:

$$\rho_{CKA}(X, Y) = \frac{\mathbb{E}\{XY\}\,\tilde{\kappa}_X(x, x')\tilde{\kappa}_Y(y, y')}{\sqrt{\mathbb{E}\{X\}\,\tilde{\kappa}_X(x, x')\mathbb{E}\{Y\}\,\tilde{\kappa}_Y(y, y')}}, \tag{3-3}$$

where $x, x' \in X$ and $y, y' \in Y$, $\mathbb{E}\{\cdot\}$ is the expectation operator, and $\tilde{\kappa}_Z$ stands for centered kernel aiming to provide translation invariance, as follows:

$$\tilde{\kappa}_Z(z, z') = \kappa_Z(z, z') - \mathbb{E}\{z\}\,\kappa_Z(z, z') - \mathbb{E}\{z'\}\,\kappa_Z(z, z') + \mathbb{E}\{zz'\}\,\kappa_Z(z, z'), \tag{3-4}$$

which is defined for a given $Z \subset \mathcal{Z}$ with samples $z, z' \in Z$. In practical applications, when provided with a set of input-output pairs $\{\boldsymbol{x}_n \in \mathbb{R}^P, \boldsymbol{y}_n \in \mathbb{R}^R\}_{n=1}^N$, we can compute the kernel matrices $\boldsymbol{K}_X, \boldsymbol{K}_Y \in \mathbb{R}^{N \times N}$ as: $K_X[n, n'] = \kappa_X(\boldsymbol{x}_n, \boldsymbol{x}_{n'})$ and $K_Y[n, n'] = \kappa_Y(\boldsymbol{y}_n, \boldsymbol{y}_{n'})$. Utilizing Eqs. (3-3) and (3-4), we can calculate the empirical estimate for the CKA alignment $\hat{\rho}_{CKA}(\boldsymbol{K}_X, \boldsymbol{K}_Y) \in [0, 1]$:

$$\hat{\rho}_{CKA}(\boldsymbol{K}_X, \boldsymbol{K}_Y) = \frac{\langle \tilde{\boldsymbol{K}}_X, \tilde{\boldsymbol{K}}_Y \rangle_F}{\sqrt{\|\tilde{\boldsymbol{K}}_X\|_F, \|\tilde{\boldsymbol{K}}_Y\|_F}}, \tag{3-5}$$

where $\|\cdot\|_F$ and $\langle \cdot, \cdot \rangle_F$ are the Frobenius norm and inner product, respectively. Besides, the centered kernel matrices in Eq. (3-5) are calculated as: $\tilde{\boldsymbol{K}}_X = \boldsymbol{H}\boldsymbol{K}_X\boldsymbol{H}$ and $\tilde{\boldsymbol{K}}_Y = \boldsymbol{H}\boldsymbol{K}_Y\boldsymbol{H}$, with $\boldsymbol{H} = \boldsymbol{I} - \frac{1}{N}\mathbf{1}^\top\mathbf{1}$ ($\boldsymbol{I}$ and $\mathbf{1}$ are the identity matrix and the all-one vector of proper size, respectively). As a result, the alignment described in Eq. (3-5) serves as a data-driven estimator, enabling us to quantify the similarity between the random variables X and Y.

3.1.2 Gaussian Functional Connectivity from EEG records

Let us examine a collection of multi-channel EEG recordings referred to as $\{\boldsymbol{X}_n \in \mathbb{R}^{C\times T}\}_{n=1}^{N}$, where C denotes the number of channels, T represents the samples within EEG recordings, and N the number of trials.

Next, let us consider two EEG channels of a given trial $\boldsymbol{x}_c, \boldsymbol{x}_{c'} \in \boldsymbol{X}$, with $c, c' \in \{1, 2, \ldots, C\}$, a pairwise correlation between the EEG channels can be computed as:

$$\hat{\rho}_L(\boldsymbol{x}_c, \boldsymbol{x}_{c'}) = \frac{1}{T}\langle \boldsymbol{x}_c, \boldsymbol{x}_{c'} \rangle_2, \tag{3-6}$$

where $\langle \cdot, \cdot \rangle_2$ stands for the inner product. The pairwise linear relationships in Eq. (3-6) allow computing functional connections between EEG channels as an undirected graph representation.

However, we can effectively capture nonlinear interactions among various channels by operating a generalized stationary kernel that transforms the input space into an RKHS. This approach enables us to obtain a more precise depiction of the underlying neural activity. Moreover, employing a stationary kernel guarantees that the proposed technique can effectively capture the temporal dynamics of EEG signals.

Given these considerations, the Gaussian kernel is widely preferred in pattern analysis and machine learning. It can approximate any function and offers mathematically tractable properties [Géron, 2022]. Therefore, it is an excellent choice for computing pairwise connections as a Gaussian-based Functional Connectivity (GFC) measure from the kernel function $\kappa_G : \mathbb{R}^T \times \mathbb{R}^T \to [0, 1]$, as [García-Murillo et al., 2023]:

$$\kappa_G(\boldsymbol{x}_c - \boldsymbol{x}_{c'}; \gamma) = \exp\left(-\frac{1}{2}\gamma \|\boldsymbol{x}_c - \boldsymbol{x}_{c'}\|_2^2\right), \tag{3-7}$$

where $\|\cdot\|_2$ denotes the ℓ_2-norm operator and $\gamma \in \mathbb{R}^+$ represents a scale parameter. The inclusion of a Gaussian function in Eq. (3-7) facilitates accurate and efficient calculation of nonlinear interactions between $\boldsymbol{x}_c$ and $\boldsymbol{x}_{c'}$.

3.1.3 KREEGNet: Kernel-based Regularized EEG Network

Let us consider an input-output set consisting of multi-channel EEG records and labels denoted as $\{\boldsymbol{X}_n \in \mathbb{R}^{C\times T}, \boldsymbol{y}_n \in \{0,1\}^R\}_{n=1}^N$. Here, $\boldsymbol{y}_n$ gathers the target labels for MI tasks encoded using the one-hot encoding (with R classes being considered). Our Kernel-based Regularized EEG Network (KREEGNet), an enhanced version of the well-known EEGNet [Lawhern et al., 2018], enables accurate prediction of the MI label $\hat{\boldsymbol{y}} \in [0,1]^R$ for a given EEG trial $\boldsymbol{X}$. This prediction is accomplished through two primary blocks. Initially, the class membership prediction is performed as follows:

$$\hat{\boldsymbol{y}} = (\varphi_Q \circ \varphi_T \circ \varphi_C \circ \varphi_{\breve{F}})(\boldsymbol{X}), \tag{3-8}$$

where notation $\varphi(\tilde{\boldsymbol{X}}) = \xi_\varphi\left(\boldsymbol{W}_\varphi \otimes \tilde{\boldsymbol{X}} + \boldsymbol{b}_\varphi\right)$ stands for DL-based layer mapping, $\circ$ is the function composition operator, $\otimes$ is the tensor product, e.g., convolutional or fully connected layer-based operations. Besides, $\tilde{\boldsymbol{X}}$ is a given network's feature map of proper size, $\boldsymbol{W}_\varphi, \boldsymbol{b}_\varphi$ gather the weight matrix and bias vector of the layer, and $\xi(\cdot)$ is a nonlinear activation function. Namely, each layer function in Eq. (3-8) is described as:

- $\varphi_{\breve{F}} : \mathbb{R}^{C\times T} \to \mathbb{R}^{\breve{F},C,T}$ is a convolutional layer holding $\breve{F}$ filters, a batch normalization, and a linear activation.
- $\varphi_C : \mathbb{R}^{\breve{F}\times C\times T} \to \mathbb{R}^{\alpha\breve{F},C,\frac{T}{4}}$ is a depthwise convolutional layer holding ELU activation (α gathers the number of spatial filters), followed by an average pooling and a dropout operation.
- $\varphi_T : \mathbb{R}^{\alpha\breve{F},C,\frac{T}{4}} \to \mathbb{R}^{\breve{F}'\frac{T}{32}}$ is a separable convolutional layer with ELU activation ($\breve{F}'$ is the number of pointwise filters), setting a batch normalization, an average pooling, and a dropout.
- $\varphi_R : \mathbb{R}^{\breve{F}'\frac{T}{32}} \to [0,1]^R$ is a fully connected classification layer fixing a flatten operation and a softmax activation.

In turn, a kernel-based regularizer is applied by properly computing the data-driven GFC:

$$\boldsymbol{K}^{\dagger} = (\widetilde{\kappa} \circ \varphi_{\breve{F}})(\boldsymbol{X}), \tag{3-9}$$

where $\varphi_{\breve{F}}$ is defined as in Eq. (3-8), $\widetilde{\kappa} : \mathbb{R}^{\breve{F},C,T} \rightarrow [0,1]^{\breve{F},C,C}$ extracts the GFC among EEG channels (see Eq. 3-7) along each of the $\breve{F}$ filters, and $\boldsymbol{K}^{\dagger} \in [0,1]^{\breve{F},C,C}$.

Furthermore, the parameter set θ, stacking the weight matrices and bias vectors in Eq. (3-8), and the scale parameter γ of the GFC in Eqs. (3-7) and (3-9), is optimized using a gradient descent-based framework with back-propagation [Zhang et al., 2021]:

$$\theta^{*} = \arg\min_{\theta} \frac{(1-\lambda)}{N} \sum_{n=1}^{N} CE(\boldsymbol{y}_n, \hat{\boldsymbol{y}}_n(\theta)) - \frac{\lambda}{\breve{F}} \sum_{f=1}^{\breve{F}} \hat{\rho}_{CKA}(\breve{\boldsymbol{K}}_f(\theta), \boldsymbol{K}_{\delta}), \tag{3-10}$$

where $\lambda \in [0,1]$ is a trade-off hyperparameter and $CE(\cdot,\cdot)$ stands for the cross-entropy loss defined as:

$$CE(\boldsymbol{y}_n, \hat{\boldsymbol{y}}_n(\theta)) = -\sum_{r=1}^{R} y_{nr} \log\left(\hat{y}_{nr}(\theta)\right), \tag{3-11}$$

with $y_{nr} \in \boldsymbol{y}_n$ and $\hat{y}_{nr}(\theta) \in \hat{\boldsymbol{y}}_n$. Moreover, the kernel-matrix $\breve{\boldsymbol{K}}_f(\theta) \in [0,1]^{N \times N}$ is computed as:

$$\breve{K}_f[n,n'] = \left\langle \text{triu}(\boldsymbol{K}_n^{\dagger}(\theta; f)), \text{triu}(\boldsymbol{K}_{n'}^{\dagger}(\theta; f)) \right\rangle_2 \tag{3-12}$$

where $\text{triu}(\boldsymbol{K}^{\dagger}(\theta; f)) \in [0,1]^{C\frac{(C-1)}{2}}$ holds the upper triangular matrix of the GFC stored in $\boldsymbol{K}^{\dagger}$ for filter f. Likewise, the target kernel matrix $\boldsymbol{K}_{\delta} \in \{0,1\}^{N \times N}$ is built as:

$$K_{\delta}[n,n'] = \delta(|\boldsymbol{y}_n - \boldsymbol{y}_{n'}|_1), \tag{3-13}$$

being $\delta(\cdot)$ the delta function and $|\cdot|_1$ the 1-norm.

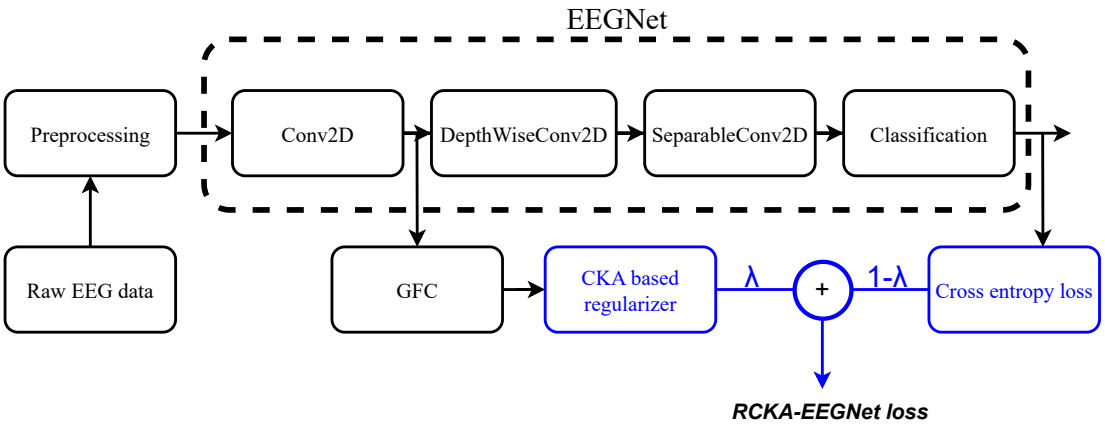

Figure **3-1**. KREEGNet pipeline for Motor Imagery classification from EEG records.

The optimization problem outlined in Eq. (3-10) enables the training of our KREEGNet for MI discrimination. Figure **3-1** summarizes the KREEGNet pipeline. To ensure numerical stability and simplicity, the GFC scale parameter is learned as a mapping of 10^{γ}. It is worth mentioning that a preprocessing stage is included to align the various database conditions, such as sample frequency, band-pass filtering, and EEG window size (refer to section 3.2.1 for more details).

3.2 Experimental Set-up

We provide a comprehensive overview of the pipeline used to develop and evaluate the KREEGNet model for MI discrimination. It includes the training phase of the model and the techniques employed to assess the effectiveness of the proposal.

3.2.1 KREEGNet Training Details and Assessment

The training of our KREEGNet consists of two stages: i) preprocessing of EEG records, and ii) fine-tuning the network hyperparameters to enhance the classification performance.

To initiate EEG preprocessing, a custom database loader module, see https://github.com/UN-GCPDS/python-gcpds.databases (accessed on 8 April 2023), was utilized to load the recordings. Only EEG channels were considered, and the signals were scaled to μV to ensure suitability for analysis. Any trials marked as bad in the datasets were rejected. A fifth-order Butterworth bandpass filter was applied to all channels within the $[4, 40]H_z$ range, where MI activity was observed [García-Murillo et al., 2023]. Additionally, each channel's signal was clipped within the post-cue onset time window, retaining only information from the MI task. For DBI, the time window was $0.5 - 3.5s$, while for DBII, it was $0.5 - 2.5s$ (see section 1.6). Then, to ensure the network parameters remained consistent, the signal from each EEG channel was downsampled in both databases from $256H_z$ in DBI and $512H_z$ in DBII to $128H_z$. Our preprocessing step is similar to the one described by the authors in [Lawhern et al., 2018].

Next, to ensure a reliable model evaluation, the stratified shuffle split 5-fold $80 - 20$ scheme was applied within each subject's data. This process involved shuffling the data and selecting 80% for training while holding out the remaining 20% for testing. This procedure was repeated five times. Model performance was evaluated using accuracy, Cohen's kappa, and the area under the ROC curve for both datasets [Géron, 2022]. In particular, the $F1$-scores for movements of the left and right hand (denoted as $F1_L$ and $F1_R$) were computed exclusively for DBII. An exhaustive search strategy for hyperparameter tuning was implemented, and the mean accuracy score across the folds was used to evaluate each hyperparameter's performance. In order to train our model, we formulated the loss function as a combination of the cross-entropy (CE) and the CKA-based regularization, with each component accordingly weighted. On the one hand, the CE component served as a guide for the model to perform the classification task effectively. On the other hand, the CKA component played a role in mitigating overfitting by considering the spatial information of the FCs computed in the GFC layer. The contribution of each term in the cost function was defined as $(1 - \lambda)$ for the CE component and λ for the CKA component. The value of λ was searched within the set $\{0, 0.2, 0.4, 0.6, 0.8\}$. We employed the Adam optimizer with an initial learning rate of $1e - 3$ to optimize the network parameters. Additionally, a

callback mechanism was implemented to decrease the learning rate by 10 when the loss function no longer exhibited improvement. The KREEGNet was trained for 500 epochs, utilizing all available samples in the training set.

The experiments conducted in this study were performed using Python version 3.8 in both Google Collaboratory and Kaggle environments. We employed TensorFlow version 2.8.2 to build models, define losses, create custom layers, and implement training strategies. To ensure reproducibility and facilitate further analysis and experimentation, we systematically saved the model weights and performance scores. For those interested in reproducing the training of our KREEGNet, we have provided a Kaggle notebook accessible at the following link: `https://www.kaggle.com/mateotobonhenao/kreegnet-training` (accessed on 8 April 2023). This resource contains all necessary details and code to replicate our training procedure.

3.2.2 Method Comparison

To assess the efficacy of our KREEGNet, we conducted a comprehensive analysis of its classification performance. Additionally, we categorized subjects into groups (for DBII) based on their classification performance to gain insights into the impact of our proposal against four classical end-to-end DL models that incorporate both temporal and spatial information from EEG signals using stacked 1D convolutions. The first model, the baseline EEGNet [Lawhern et al., 2018], utilizes separable convolutions to reduce parameters while maintaining performance similar to traditional convolutional layers. In addition, it includes a depthwise convolution layer to capture spatial information and a fully connected layer with softmax activation for classification. The second model, Shallowconvnet [Schirrmeister et al., 2017], is a simpler architecture consisting of a single convolutional layer followed by non-linear activation, batch normalization, and pooling layers. Despite its simplicity, it effectively classifies EEG signals. The third model,

Deepconvnet [Schirrmeister et al., 2017], is a deeper architecture comprising five convolutional layers, followed by non-linear activation, batch normalization, and pooling layers. Although it performs well in EEG signal classification, it is computationally more expensive than Shallowconvnet and EEGNet. Finally, we consider the TCFussionnet proposed in [Musallam et al., 2021]. This model consists of three main components: a temporal component that learns various bandpass frequencies, a depth-wise separable convolution that extracts spatial features for each temporal filter, and a Temporal Convolutional Network (TCN) block that captures temporal features. These features are combined to generate comprehensive feature maps, which are then classified into different MI classes using a dense layer with softmax activation. The Kaggle notebook available at (`https://www.kaggle.com/mateotobonhenao/dl-methods-comparison` - accessed on 8 April 2023) contains the code necessary to assess the MI classification effectiveness of the aforementioned DL models. Besides, the following GitHub repository holds the complete codes related to our experiments (`https://github.com/mtobonh/KREEGNet` - accessed on 8 April 2023).

3.3 Results and Discussion

3.3.1 Baseline EEGNet vs. KREEGNet: Subject and Group-Level Results

A comparative analysis is conducted between KREEGNet and the widely recognized benchmark, EEGNet, for both DBI and DBII datasets in the context of binary MI classification tasks. The analysis specifically focuses on distinguishing between left and right-hand imagery movements. A subject-specific examination is executed across both databases, while the group-level analysis is limited solely to DBII due to DBI's composition of a mere nine subjects. A scoring matrix is constructed for robust validation, where the rows correspond to the dataset's subject count (50 for

DBII), and six columns represent accuracy, Cohen's kappa, the area under the ROC curve scores, and their corresponding standard deviations. To maintain the principle of 'the higher, the better' and restrict all column values within the $[0, 1]$ range in the scoring matrix, the substitution of the standard deviation with its complement and normalize Cohen's kappa by adding one and dividing by two. Following that, we utilize this scoring matrix and the k-means clustering algorithm [Géron, 2022], setting k to three, to train a model that categorizes subject results based on the benchmark model EEGNet into three groups: top performers (GI), average performers (GII), and low performers (GIII). Subsequently, our KREEGNet's subject analysis results are clustered using the trained k-means and the score matrix. The ultimate goal is to examine and discern how subject classification shifts between the EEGNet and the KREEGNet-based groups [García-Murillo et al., 2023].

Figure **3-2**a and **3-2**b present a comparative accuracy analysis of subject-specific and group-level analysis. The dotted orange line in the figures corresponds to the EEGNet; in contrast, the dotted blue line illustrates the proposed KREEGNet. The blue and red bars in the figures indicate the impact of employing the KREEGNet on individual subject accuracy. Specifically, the blue bars denote improvements in accuracy, while the red bars indicate decreases. These visual cues provide valuable insights into the performance enhancements achieved by our approach across specific subjects. Moreover, in the context of DBII, the figure's background incorporates bars with low opacity in opal green, lemon yellow, and salmon pink. These color-coded backgrounds denote the grouping of subjects into top-performing, average-performing, and low-performing subjects.

Our KREEGNet model's performance regarding DBI reveals a subject-dependent average accuracy of 78.0%, surpassing the baseline EEGNet by 1.6%. Notably, out of all the subjects, only Subject seven (S7) experienced a marginal decrease in performance, with a decline of less than 1%. Conversely, the remaining subjects demonstrated improvements in accuracy. Particularly impressive was Subject four (S4), exhibiting a remarkable performance increase of 4.7%, showcasing the effectiveness of our KREEGNet model in enhancing subject-specific analysis by coding relevant functional connections among channels within an end-to-end regularized network.

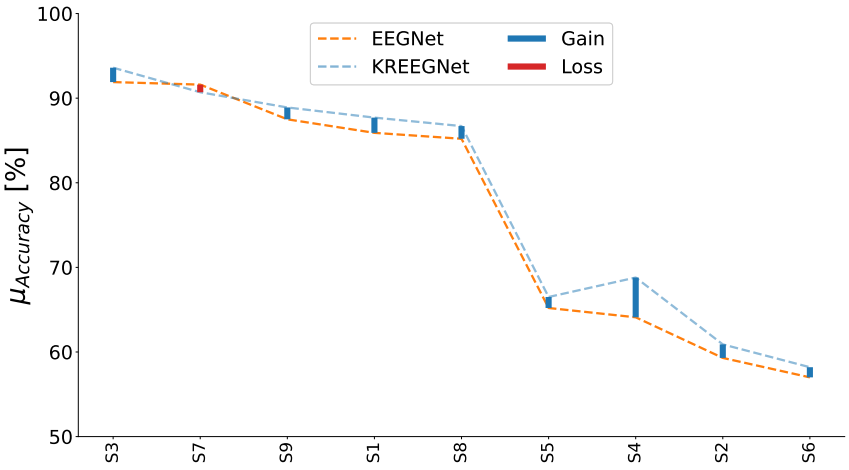

(a) Average Accuracy: EEGNet 76.4%, KREEGNet A 78.0%.

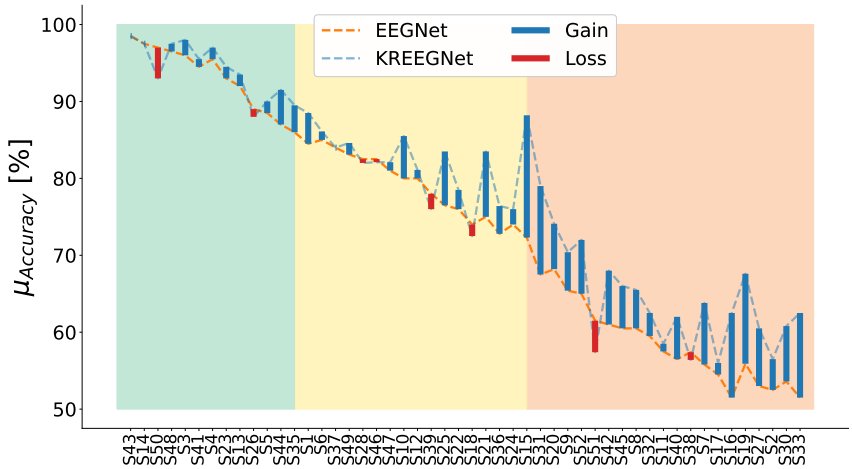

(b) Average Accuracy: EEGNet 74.4%, KREEGNet A 77.9%.

Figure **3-2**. EEGNet vs. KREEGNet comparison results. The Figure 3-2a demonstrates the subject-specific analysis for DBI, while the Figure 3-2b exhibits the group-level evaluation for DBII (KREEGNet gain: GI 1.0%, GII 2.9%, and GIII 5.7%). The reported mean accuracy corresponds to a binary MI classification of left versus right-hand movement. Subjects have been organized following their EEGNet performance. The blue bars show improvements in the performance achieved by our proposed KREEGNet, whereas the red bars highlight cases of reduced performance. The backdrop for the DBII results visually represents the group membership, with top performers in GI, average performers in GII, and low performers in GIII.

For DBII, the EEGNet and KREEGNet models achieved subject-dependent average accuracies of 74.4% and 77.9%, respectively, indicating an incremental improvement of 3.5% for our proposal. The standard deviations for EEGNet and KREEGNet were 14.9% and 13.2%, respectively, suggesting that our approach resulted in less variability among subjects' performance. Interestingly, the accuracy of KREEGNet varied across the subjects, with three scenarios emerging from the results. Firstly, eight subjects showed a decrease in accuracy, with only three experiencing a reduction of 2% or more. Secondly, two subjects did not show any change in accuracy. Lastly, the remaining subjects demonstrated an increase in accuracy, with nineteen of them experiencing an increase of more than 5%.

Now, the impact of our method on the performance of different subject groups in DBII was substantial. In the case of Group GIII, the KREEGNet outperformed the baseline in all but two instances, with a remarkable increase of over 5% observed in fourteen cases. As for Group GII, four subjects experienced a minor decrease of less than 2%, while one remained unchanged. On the other hand, twelve subjects showed a performance improvement, with half achieving an increase of over 3%. Of particular note is Subject 15, which exhibited an impressive performance boost of 16%, highlighting the strong influence of our CKA-based regularizer on specific individuals. In Group G III, only two subjects witnessed a decrease in accuracy, while nine subjects demonstrated improved performance, including two with increases exceeding 3%. So then, our strategy yielded significant performance enhancements for most subjects across all groups, with a notable benefit observed in the poorly performing subject group.

Similarly, Figure **3-3** presents the categorization of the subject group and the influence of the KREEGNet. The initial row displays the arrangement of subjects as per the results of EEGNet, while the final row illustrates the shift or constancy of each subject's group derived from the KREEGNet outcomes. For example, in GIII, our approach promoted four subjects to GII. Likewise, two individuals were elevated from GII to GI. Importantly, no individual experienced an in-group demotion status, underlining the equal or superior performance of KREEGNet compared to the standard EEGNet.

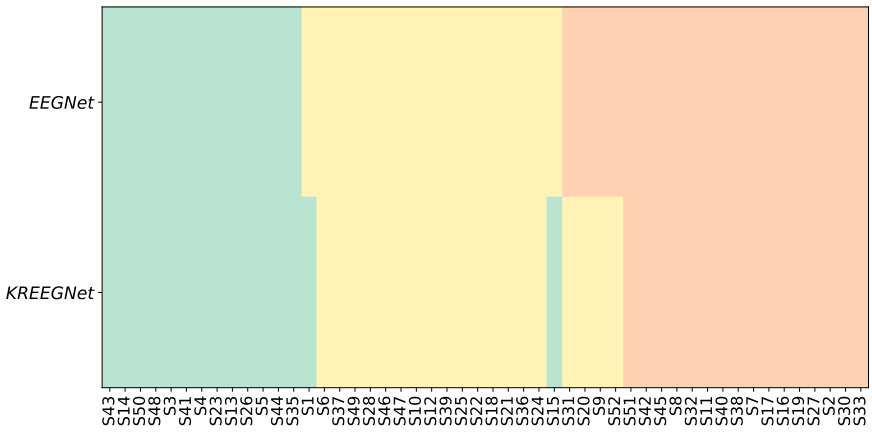

Figure **3-3**. KREEGNet subject group enhancement (Baseline: EEGNet). Note that green, yellow, and red represent top, average, and low performance regarding the average accuracy along subjects. First row: The arrangement of subjects according to EEGNet classification. Second row: Alterations in subject group affiliations based on the results of KREEGNet.

3.3.2 Hyperparameter Analysis

Subsequently, we scrutinized the complex behavior of the hyperparameters λ and γ across different subject groups in DBII. λ symbolizes the importance given to the CKA-based regularizer in the cost function of KREEGNet, contributing to enhancing the network's classification capabilities. Conversely, γ sets the bandwidth scale for the Gaussian kernel employed in the GFC layer that calculates the FCs. By investigating the dynamics of these hyperparameters, we seek to understand their influence on performance and the GFC layer's FC estimation. Figure **3-4**a presents a boxplot depicting the statistical distribution of the λ hyperparameter among the subject groups, with the background boxes denoting group membership. Firstly, most tend to posse lower λ values in GI, specifically below 0.6. This is attributed to the fact that subjects within this group display more evident MI patterns, readily captured by the standard EEGNet model. Secondly, GII exhibits a more evenly distributed set of values, with half of the subjects presenting λ values exceeding 0.3. This could imply that some subjects at this stage demonstrate noisy MI patterns that heighten the

risk of overfitting the training data, thereby reducing the classification performance. Lastly, for GIII, λ values are predominantly higher. Specially, half of the subjects in this group have λ values above 0.5, with the majority of the remainder having values ranging between 0.4 and 0.5. The latter suggests that most of the subjects' data in this group present noisy patterns. Nevertheless, the CKA-based regularizer, working on the FCs computed by the GFC layer, aids in eliminating this unwanted effect, leading to improved classification performance.

In the same way, Figure 3-4b displays the boxplot of the γ hyperparameter among different subject groups. This bandwidth filters the relationships between channels, suggesting that channels with higher noise levels have lower bandwidth values to circumvent unwarranted connections. The findings imply that subjects in GIII require more filtering through the γ parameter, hinting that these individuals typically have higher noise in their MI patterns. Our CKA-based regularizer and the GFC layer contribute to the reduction of these noises, thereby enhancing classification performance. Notably, our results demonstrate an inverse linear relationship between the fixed λ and γ values. Specifically, subjects with good performance, i.e., those in G I and some in G II, exhibit lower values of λ and higher values of γ, indicating a low contribution of the CKA-based regularizer and that the bandwidth of the GFC layer is more flexible in filtering out the relationship between channels. This suggests that the MI patterns for these subjects are cleaner and less affected by noise. Conversely, subjects with poor performance, i.e., those in G III, exhibit higher values of λ and lower values of γ, indicating that the CKA-based regularizer contributes more to the cost function to reduce the effect of overfitting due to the presence of noise. Additionally, γ shrinks the value of the bandwidth in the GFC layer to be more rigid in filtering out the relationship between channels, thereby avoiding spurious connectivities. These findings highlight our KREEGNet's importance in optimizing the performance and interpretability of EEG-based MI tasks.

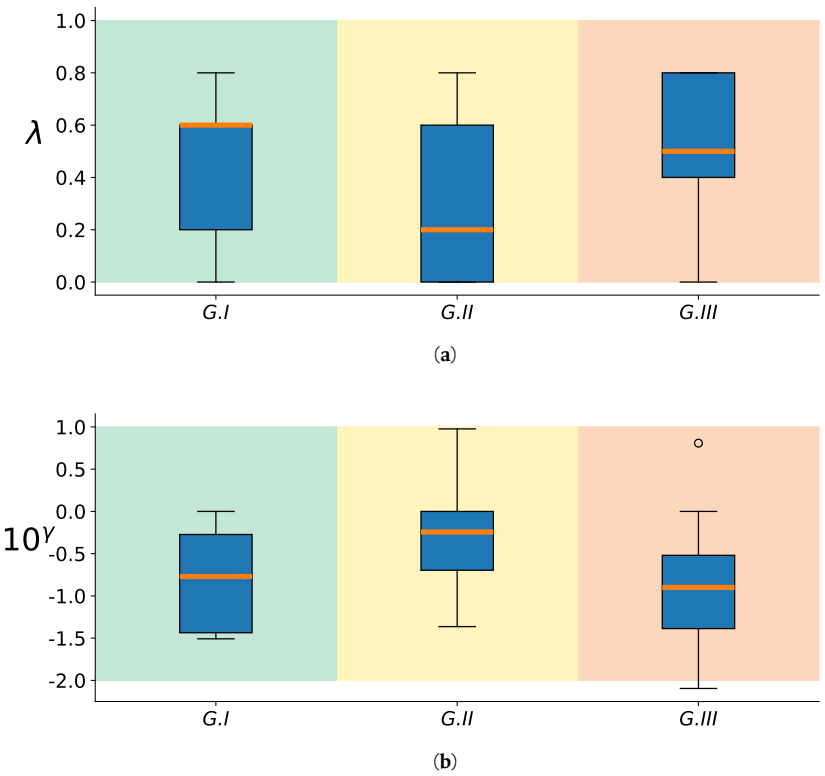

Figure **3-4**. Analysis of KREEGNet hyperparameters at the group level for DBII. Boxplot diagrams are provided for the tuned λ and γ values in relation to the top (GI), average (GII), and low (GIII) performing subjects.

3.3.3 Method Comparison Results: Binary and Multi-Class MI Classification

The classification performance of the DL models discussed in Section 3.2.2 for DBI and DBII are presented in Tables **3-1** and **3-2**, respectively. The results indicate that the DeepConvenet model performs the worst for both databases, while our proposed KREEGNet achieves the highest MI classification results. Notably, the Shallowconvnet, EEGNet, and TCFusionnet networks conduct similarly in both databases. Our KREEGNet attains outstanding results in all classification measures for DBII, demonstrating its superior performance. Although our model also achieves the best results for DBI, the difference in performance compared to other models is

Table **3-1**. Multi-class MI classification results for DBI. Average Accuracy, Kappa, and AUC are displayed ± the standard deviation.

Approach	**Accuracy**	**Kappa**	**AUC**
Deepconvnet [Schirrmeister et al., 2017]	55.5 ± 24.3	40.6 ± 32.4	78.1 ± 20.4
Shallowconvnet [Schirrmeister et al., 2017]	74.9 ± 13.3	66.7 ± 17.7	91.6 ± 7.2
EEGNet [Lawhern et al., 2018]	76.4 ± 14.6	68.6 ± 19.5	92.5 ± 0.71
TCFussionnet [Musallam et al., 2021]	77.3 ± 13.4	69.7 ± 17.9	92.6 ± 0.68
KREEGNet (ours)	$\mathbf{78.0 \pm 14.1}$	$\mathbf{70.7 \pm 18.8}$	$\mathbf{92.6 \pm 0.7}$

Table **3-2**. Binary MI classification results for DBII. Average Accuracy, Kappa, $F1_L$, $F1_R$ and AUC are displayed ± the standard deviation.

Approach	**Accuracy**	**Kappa**	**$F1_L$**	**$F1_R$**	**AUC**
Deepconvnet [Schirrmeister et al., 2017]	61.9 ± 12.4	23.6 ± 24.9	59.5 ± 13.8	63.0 ± 13.0	66.0 ± 16.0
Shallowconvnet [Schirrmeister et al., 2017]	72.5 ± 14.1	44.6 ± 28.3	71.8 ± 14.7	72.4 ± 14.4	77.9 ± 15.3
TCFussionnet [Musallam et al., 2021]	73.9 ± 14.8	48.0 ± 30.0	73.8 ± 15.3	74.0 ± 14.7	80.0 ± 16.3
EEGNet [Lawhern et al., 2018]	74.4 ± 14.9	48.6 ± 29.8	73.3 ± 15.8	74.4 ± 15.5	79.6 ± 16.4
KREEGNet (ours)	**77.9 ± 13.2**	**55.7 ± 26.5**	**77.1 ± 13.8**	**77.6 ± 14.0**	**82.5 ± 14.5**

less significant. This can be attributed to the fact that DBI has fewer channels, with most of them concentrated in the central brain area, which limits the effect of the estimated FC by the GFC layer and the CKA-based regularizer. Then, only interactions between channels located in the same brain region are considered, reducing the diversity of information.

3.4 Summary and Discussion

This chapter introduced a novel regularizer to mitigate overfitting in end-to-end DL models for MI tasks. Our regularizer effectively filtered out noise-related artifacts by leveraging the CKA method and incorporating a data-driven GFC layer while preserving relevant MI activity in EEG signals. The experimental results confirmed the significant improvements achieved by our regularized approach, enhancing overall MI performance and reducing performance variability among subjects, particularly for those with initially poor performance. Furthermore, the hyperparameter analysis further strengthened the reliability and effectiveness of our regularizer, and the comparison against other DL architectures confirm its superiority in the context of MI classification tasks.

CHAPTER

FOUR

FC AND KOLMOGOROV-SMIRNOV TEST-BASED METHOD TO UNDERSTAND DIFFERENCES AMONG MI TASK PERFORMERS.

This chapter introduces a new method to thoroughly explore the variations in brain processes among subjects with different performance levels. Our method allows for a qualitative assessment of the distinct brain patterns exhibited by each subject, achieved by representing them as discriminative FC matrices.

To accomplish this, we start by converting the EEG signals of each subject into graph-structured data using an FC estimator (specifically, the FCs estimated in Chapter 3 using the GFC layer). This conversion enables us to capture the complex connections among various brain regions. We then group the FCs based on MI classes and utilize a Kolmogorov-Smirnov (KS) test to measure the distinguishability of these classes at the connectivity level. As a result, we obtain a single FC matrix that highlights the most significant connections for each subject concerning the MI task.

Subsequently, we utilize the obtained discriminative FC matrices and the classification scores (obtained in Chapter 3) to comprehensively analyze the variations in FC patterns across individuals and groups of subjects. Additionally, we utilize the discriminative FC matrices to measure the differences in noise levels among subjects and create topographical maps that provide valuable insights into the most discriminative brain regions.

4.1 Methods

4.1.1 Kolmogorov-Smirnov test

The KS test is a non-parametric statistical test used to determine if two datasets follow the same underlying probability distribution [Berger and Zhou, 2014]. It compares the cumulative distribution functions of the two samples and quantifies the maximum difference, known as the KS statistic [Vrbik, 2020]. This test is particularly useful when the distribution assumptions of parametric tests are not met or when the data are measured on an ordinal or interval scale.

The KS test can be performed as a one-sample or two-sample test. This section focuses on the two-sample KS test, which assesses whether two independent samples are drawn from the same population distribution [Engmann and Cousineau, 2011].

In the two-sample KS test, the null hypothesis H_0 assumes that the two samples are drawn from the same distribution, while the alternative hypothesis H_1 suggests that the distributions differ. The KS statistic, $d_{a,b}$, is defined as

$$d_{a,b} = \sup_{\nu} |L_{1,a}(\nu) - L_{2,b}(\nu)| \tag{4-1}$$

Where $L_{1,a}(\nu)$ and $L_{2,b}(\nu)$ are the empirical distribution functions of the first and the second sample ν, respectively, and sup denotes the supremum function.

For large samples, the null hypothesis is rejected at level $\jmath$ if

$$d_{a,b} > t(\jmath)\sqrt{\frac{a+b}{a.b}} \tag{4-2}$$

Where a and b are the sizes of the first and second samples, respectively, the critical value $t(\jmath)$ is obtained from the KS distribution and depends on the chosen significance level.

4.1.2 Construction of Topographic Maps from EEG Signals

Topographic maps provide a spatial representation of the electrical activity in the brain based on EEG signals. These maps offer valuable insights into the distribution and localization of neural activity across the scalp [Hooi et al., 2015]. In this section, we describe the methodology for constructing topographic maps from EEG data.

Scalp Potential Model

To construct topographic maps, we begin by considering the scalp potential distribution resulting from neural activity. The scalp potential at any point on the scalp can be represented as a linear summation of the contributions from underlying electrical sources. The general equation for the scalp potential at a given electrode location, denoted by $v(i,j)$, can be expressed as:

$$v(i,j) = \sum_{q=1}^{Q} \hat{o}_q \cdot s_q(i,j)$$

where Q is the total number of electrical sources, $\hat{o}_q$ represents the weight or strength of the q-th source, and $s_q(i,j)$ denotes the contribution of the q-th source at location (i,j) on the scalp.

Interpolation Techniques

To construct topographic maps, the scalp potential distribution needs to be estimated at locations where electrode measurements are not available. Interpolation techniques are commonly used for this purpose. One widely used method is the spline interpolation, which assumes that the scalp potential can be represented by a smooth surface. The interpolated scalp potential, denoted by $\hat{v}(i, j)$, can be obtained using the following equation:

$$\hat{v}(i, j) = \sum_{q=1}^{Q} \hat{o}_q \cdot \hat{s}_q(i, j)$$

where $\hat{s}_q(i, j)$ represents the interpolated contribution of the q-th source at location (i, j).

Weighting Scheme

The weights assigned to each electrical source in the scalp potential model play a crucial role in constructing topographic maps. The choice of weighting scheme depends on the specific research question and analysis goals. Commonly used weighting schemes include the dipole model, Laplacian transformation, and PCA. These schemes aim to enhance the sensitivity to particular neural sources or highlight specific patterns of activity.

Visualization

Once the scalp potential distribution is estimated at all locations, a topographic map can be generated by assigning colors or contour lines to represent the magnitude of the scalp potential at each electrode site. The color scale or contour lines are chosen to reflect the range of values observed in the data, allowing for visual interpretation of the spatial distribution of neural activity.

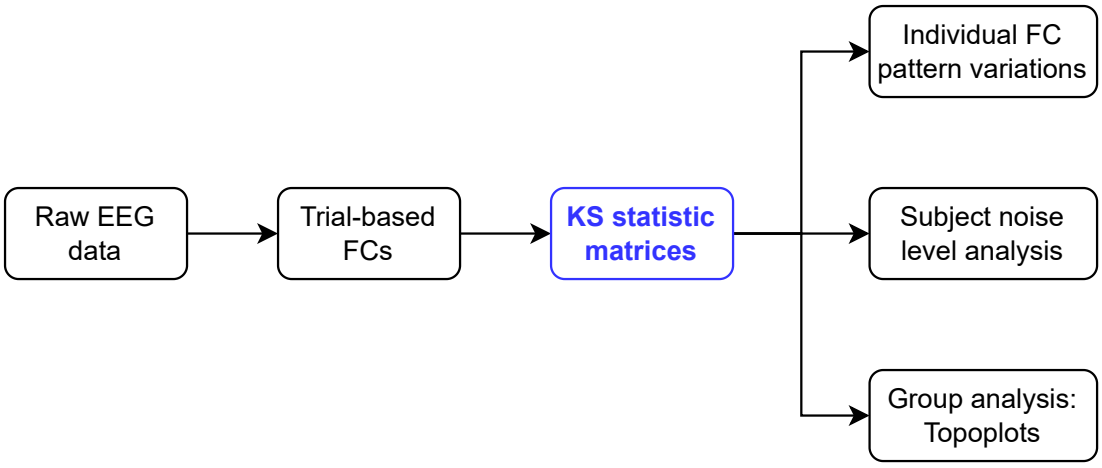

Figure **4-1**. Schematic diagram illustrating the proposed methodology to examine inter-subject variations in brain processes across different performance levels. The blue box indicates the key step.

4.2 Experimental Set-up

We evaluated the FC variations across subjects, focusing on determining which connections significantly influence the ability to distinguish between the MI classes. Acknowledging that a strong correlation in the FC matrix does not automatically translate into enhanced class distinction is essential. In this endeavor, we utilized the KS statistic 4.1.1, a tool that quantifies the disparity between the class distributions for each FC. Our KS-based connectivity pruning, illustrated in Figure **4-1**, proceeds as follows:

- We categorized each connection's trials for an individual based on the label, forming the right and left sample sets (in case of DBII).

- Following this, we calculated the KS statistic for the connectivity between each pair of EEG channels along the training set trials. A KS value nearing 1 signifies a high level of distinguishability for the connectivity between two channels, whereas a value approaching 0 suggests a low level of separability.

- Moreover, we utilized the maximum operator across the estimated FCs for each feature map to establish a KS statistic matrix. This matrix denotes the class-separability of each connectivity.

- In order to illustrate the variations in each KS statistic matrix across subjects and groups, we depicted each matrix of KS statistic values on a two-dimensional scatter representation. Both dimensions were calculated employing the widely accepted t-SNE algorithm (see appendix C) over the RCKA-EEGNet score matrix obtained in chapter 3.

- Lastly, to fully comprehend the key connectivities and channels involved in the MI classification, we used topoplots 4.1.2 from the KS statistic matrix. To compute topoplots, we initially quantified channel contribution using normalized node degree. Then, we highlighted relevant connectivities above 0.8. For DBII, representative KS matrices were obtained for each group using the median operator, identifying prominent connectivities and channels.

4.3 Results and Discussion

4.3.1 Individual FC pattern variations

Figures **4-2** and **4-3** depict the t-SNE 2D projections of the KS statistic matrices of each subject for DBI and DBII, respectively. In particular, the color-coded outer square of Figure **4-3** represents the group affiliation (GI, GII, and GIII). This visual representation enhances our comprehension of the significant connectivity patterns in the MI classification task. Figure **4-2** depicts the optimal performing subjects at the bottom, intermediate performers towards the left-middle, and the poorly performing ones at the top-left. Notably, the KS statistic matrices of high-performing subjects are more distinct, except for subject 7. This finding suggests that the FCs estimated by the GFC layer hold more significance in the MI classification. On the

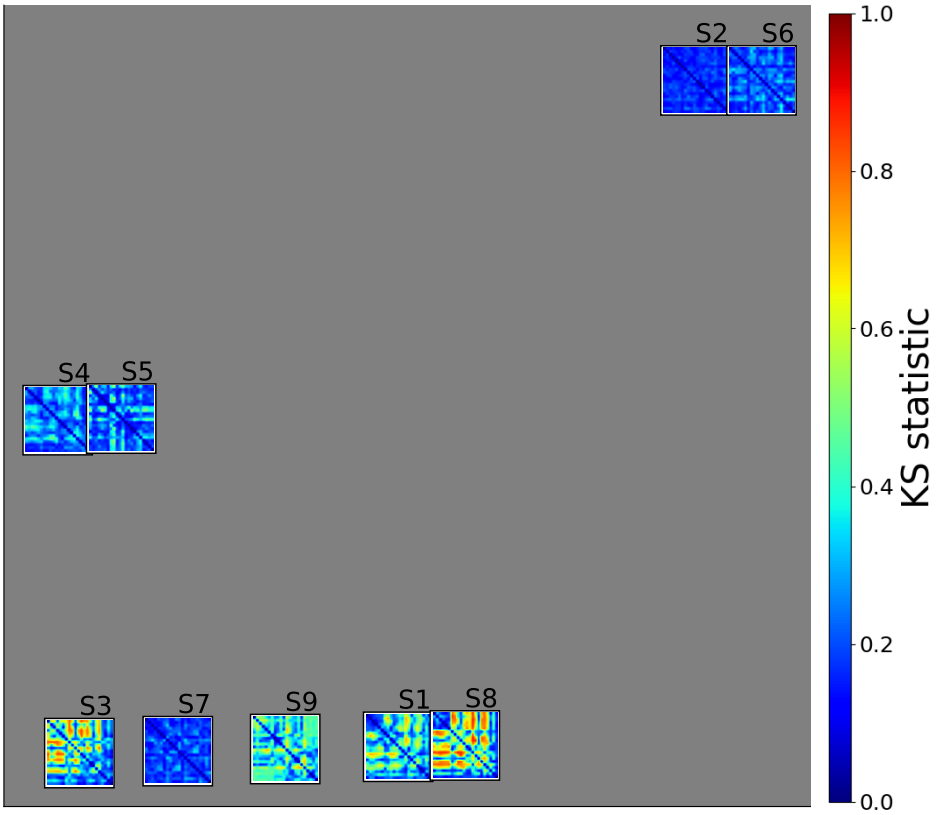

Figure **4-2**. DBI-2D t-SNE projection of KS-based pruned FC matrices utilizing our RCKA-EEGNet. A gradation of colors ranging from blue to red represents a continuum from low to high separability.

contrary, intermediate and poor performers show sparse KS matrices, implying their data has a higher noise level, which results in erroneous FCs that overlap with MI class distributions.

Likewise, Figure **4-3** shows how G III exhibits sparse KS statistic matrices in the bottom-right corner, indicating that the FCs estimated are not discriminative among classes. This observation can be explained by the fact that the γ parameter took lower values for this particular group of subjects (see 3.3.2), which tend to produce sparse matrices regardless of MI classes. In contrast, the subjects in G I in the top-left tend to have more fired KS statistics, with a notable concentration over the MI area. Finally, G II reveals more erratic behavior, with the subjects near G III. The latter may be attributed to individual differences in brain activity during the MI tasks.

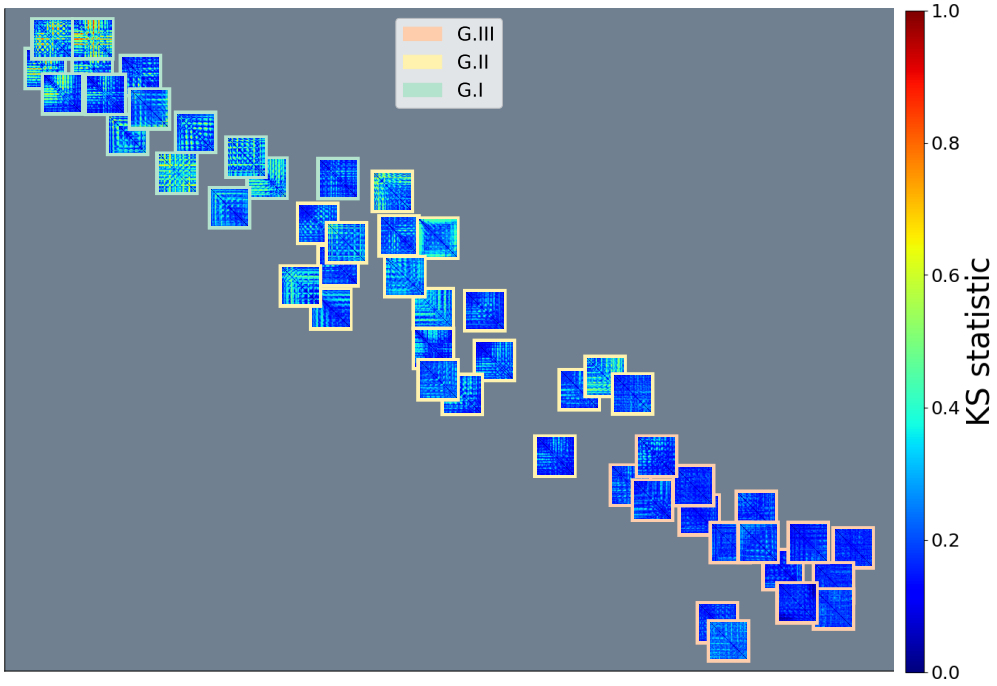

Figure **4-3**. DBII-2D t-SNE projection of KS-based pruned FC matrices utilizing our RCKA-EEGNet. A gradation of colors ranging from blue to red represents a continuum from low to high separability. Outer boxes indicate subject group belongingness: green G I, yellow G II, and red G III.

4.3.2 Subject noise level analysis

In order to evaluate the informational dynamics of pruned FCs, we utilized quadratic Rényi's entropy, computed over the KS statistic matrices [Giraldo et al., 2014]. Our observations suggested that sparse KS statistic matrices corresponded with higher noise levels, whereas the KS matrices that had been freed up corresponded to lower noise levels. These statements are corroborated by Figures **4-4**a and **4-4**b. Furthermore, our findings align with the mentioned statements from Chapter 3. Specifically, the subjects that perform poorly in DBI tend to display higher entropy values, which is also true for the subjects classified under G III in DBII.

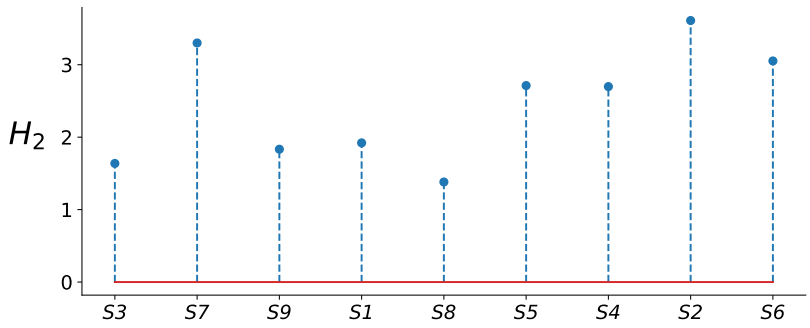

(a) DBI results.

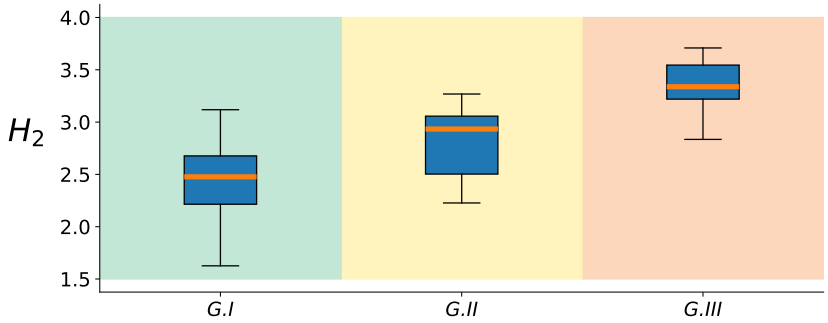

(b) DBII results.

Figure **4-4**. Renyi's entropy-based retained information within the estimated functional connectivity matrices (H_2 stands for quadratic entropy value). **4-4**a: DBI results sorted regarding the classification performance. **4-4**b: DBII results where the background codes the group membership (best, medium, and poor-performing subjects. Boxplot representation is used to present the retained information within each group.

4.3.3 Group analysis: Topoplots

Next, the topoplots in Figures **4-5**a and **4-5**b show the distribution of relevant connectivities and channels. Certain subjects are selected for visualization purposes in DBI. Meanwhile, the median KS statistic matrix of each group in DBII is employed. The results indicate that the sensorimotor area is the most critical region for both databases. It suggests that our RCKA-EEGNet effectively improves classification

performance and model interpretability by incorporating a CKA-based regularizer and a GFC layer.

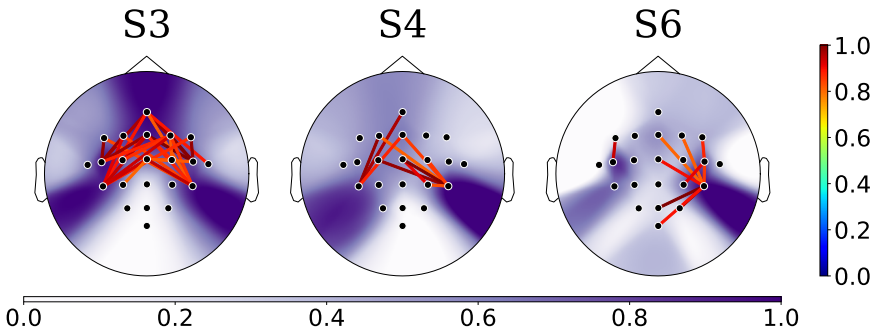

(a)

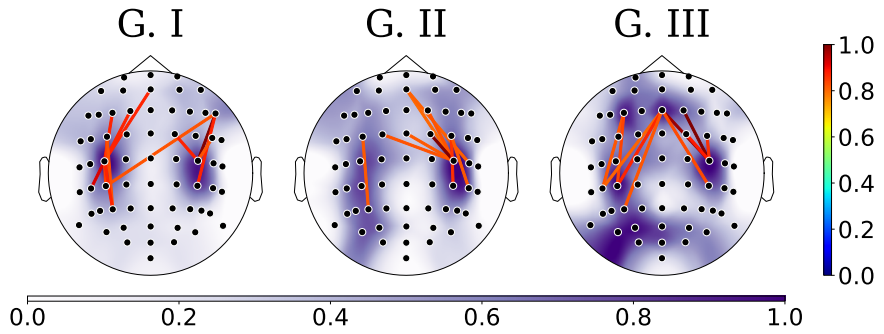

(b)

Figure **4-5**. Visual outcomes of the topographical maps (DBI and DBII results). Figure 4-5a illustrates the results related to significant subjects for the DBI. Figure 4-5b displays group-oriented visualizations for the DBII. Only those connections that hold a value surpassing the 95th percentile are highlighted. The backdrop of these visualizations corresponds to the normalized cumulative connection strength across channels, which is projected onto the topographical map.

For DBI, we analyzed S3, S4, and S6 to represent high-performing, intermediate, and low-performing subjects. Notably, S3 exhibited a higher number of relevant FCs compared to S4 and S6. Furthermore, the FCs of S3 and S4 are thickened in the central-brain region, consistent with the MI paradigm. However, S6 displayed a concentration of FCs in a single channel in the left-central region. Concerning DBII, the analysis of connectivities and channels in G I subjects revealed that the primary areas of interaction during MI tasks are located in the left-right central regions. This

finding suggests that these subjects exhibit more distinct and reliable patterns of MI activity. The subjects belonging to G II displayed a pattern of connectivities and channels in the right-central brain region. However, a diffuse pattern was observed in the left hemisphere, covering some posterior and brain regions not strongly associated with MI activity. This diffuse pattern may be attributed to noise-induced EEG features, affecting classification performance. Finally, for the subjects in G III, the connectivities are concentrated in the central region of both hemispheres, which aligns with the MI paradigm. Similar to G II, the main channels are located in the right-left central brain areas, but robust patterns are observed in the left-posterior and frontal areas, highlighting noisy behavior.

4.4 Summary and Discussion

Our chapter presented a new method for investigating the differences in brain processes among individuals with varying levels of performance in MI tasks. The study converted EEG signals into graph-structured data using a FC estimator, which allowed for capturing the complex connections between different brain regions. The KS test was used to measure the distinguishability of FCs between MI classes. This resulted in distinguishing FC matrices that highlighted the most discriminative connections for each subject. The analysis of individual FC pattern variations showed that high-performing subjects had more distinct KS matrices, indicating the importance of the estimated FCs for accurate classification. Additionally, examining the noise levels of subjects using Renyi's entropy revealed that sparse KS matrices corresponded to higher noise levels. The group analysis, conducted using topographic maps, identified the sensorimotor area as the most critical region for MI tasks in both databases. In summary, the proposed method offered valuable insights into the variations in FC patterns and the impact of noise on distinguishing performers in MI tasks.

CHAPTER

FIVE

FINAL REMARKS

5.1 Conclusions

In conclusion, this thesis presents a comprehensive ML framework designed to support multi-channel time series classification in BCIs while preserving interpretability. The main contributions of this work can be summarized as follows:

Firstly, we introduced a Subject-Dependent Artifact Removal strategy (*SD-AR*) to address the challenge of low SNR in EEG signals, which leads to variations in subjects' performance during MI tasks. The *SD-AR* approach selectively removes artifacts based on individual classifier accuracy, providing a subject-specific artifact removal process that effectively enhances the quality of EEG data.

Secondly, a novel regularizer was developed to address the issue of overfitting in end-to-end DL models used for MI tasks. This regularizer leverages the well-established CKA method and incorporates information from EEG signals about FCs to guide DL

architectures in focusing on intrinsic MI patterns while reducing the influence of noise in EEG signals.

Additionally, we presented a new method for investigating the differences in brain processes among individuals with varying levels of performance in MI tasks. By converting EEG signals into graph-structured data using an FC estimator, we were able to capture complex connections between different brain regions. The use of the KS test resulted in discriminative FC matrices that highlighted significant connections for each subject, contributing to the explainability of end-to-end DL models.

Collectively, these contributions significantly advance the field of BCI and multi-channel time series classification. The *SD-AR* strategy and regularizer effectively address the problem of ISV, enhancing the reliability and generalization of BCI systems. Moreover, the proposed method for investigating brain process differences adds a new dimension of interpretability to end-to-end DL models.

Furthermore, the availability of the implementation code in a GitHub repository facilitates the research community's adoption and fosters further development of these techniques. The open-source nature of the code promotes collaboration, enables reproducibility, and empowers researchers to build upon these methods for future advancements in BCI systems.

5.2 Future Work

As part of the future work, this thesis proposes a comprehensive research path aimed at further enhancing the developed approach and expanding its applicability in Brain-Computer Interface (BCI) systems. The following key research directions are outlined:

- Evaluation with Diverse Databases: To validate the effectiveness and generalizability of the subject-dependent preprocessing approach, the authors

plan to evaluate it on databases containing more subjects and lower-quality EEG data. By testing the approach in diverse datasets, the research can ensure its robustness and applicability to a broader range of real-world scenarios. This evaluation will shed light on the approach's performance and reliability in different contexts, providing insights into its potential practical use.

- Elaborate Feature Extraction Methods: In order to tackle the issue of low Signal-to-Noise Ratio (SNR) in subjects performing poor motor imagery tasks, the authors aim to explore more elaborate feature extraction methods. By investigating advanced techniques for extracting relevant information from EEG signals, the thesis can further improve the quality of processed data, leading to enhanced classification accuracy and more reliable BCI systems.

- Investigation of Artifact Removal in Modern DL Architectures: To ensure the compatibility of the developed artifact removal approach with modern DL architectures, future work will focus on exploring its effectiveness in such architectures. This investigation is crucial as DL models are continually evolving, and the proposed approach should be adaptable to leverage the advancements in DL techniques. Ensuring compatibility with modern architectures will enhance the approach's potential for broader adoption and integration into state-of-the-art BCI systems.

- Integration of Eye-Tracking and Cognitive Psychological Attention Test Data: To further enhance the artifact removal approach and improve both BCI performance and interpretability, the authors plan to integrate eye-tracking and cognitive psychological attention test data. By incorporating additional sources of information related to users' attention and cognitive states, the thesis can refine the artifact removal process, leading to more accurate and reliable BCI predictions. This integration can also provide valuable insights into users' cognitive processes during MI tasks, contributing to the overall interpretability of the BCI system.

- Augmentation of KREEGNet with Graph Convolutional Networks: As part of future research, the authors aim to augment KREEGNet to achieve end-to-end functional connectivity estimation via graph convolutional networks. By leveraging graph-based neural networks, the BCI system can better capture complex connections between brain regions, leading to improved classification performance and enhanced interpretability. This augmentation can facilitate a more comprehensive understanding of brain dynamics during MI tasks.
- Investigation of Causal Connectivity with Information-Theoretic Learning: Future work also involves investigating causal connectivity rooted in information-theoretic learning for deep-learning-based estimations. By exploring causal relationships between brain regions, the research can uncover meaningful interactions and dependencies, providing deeper insights into the underlying neural mechanisms during MI tasks. This investigation can lead to a more detailed understanding of the brain's functional connectivity and contribute to improved BCI system performance.
- Subject-Independent Experiments and Testing Transformer Networks: To validate the generalizability of the proposed methods, the authors plan to conduct subject-independent experiments. This will test the models' performance on unseen subjects, verifying their ability to adapt to different individuals. Additionally, the research will explore the use of transformer networks, which have demonstrated success in various domains. Integrating transformer networks into the BCI system can enhance its ability to capture long-range dependencies in EEG signals and lead to improved multi-channel time series classification.

5.3 Limitations

Even though the work is of high quality and relevance, certain limitations are acknowledged in this section:

- Although subject variability was investigated, the creation of a universal, subject-independent model remains challenging, as the solutions require a model for each subject to capture specific brain dynamics.
- To understand MI dynamics, the work presented crucial frequency bands and brain interconnections for each subject in the MI classification task, grouping and comparing subjects based on performance. However, the omission of crucial time segments for the MI classification task hinders a comprehensive understanding of temporal dynamics.
- The exclusive reliance on MI time segments for classifying EEG signals limits the real-time applicability of the proposed MI-EEG-based system.

5.4 Academic Products

- Tobón-Henao, M., Álvarez-Meza, A. M., & Castellanos-Dominguez, C. G. (2023). Kernel-Based Regularized EEGNet Using Centered Alignment and Gaussian Connectivity for Motor Imagery Discrimination. Computers, 12(7), 145. (Q2/A2/Minciencias)
- Tobón-Henao, M., Álvarez-Meza, A., & Castellanos-Domínguez, G. (2022). Subject-dependent artifact removal for enhancing motor imagery classifier performance under poor skills. Sensors, 22(15), 5771. (Q1/A1/Minciencias)
- B. Lotero-Londoño, M. Loaiza-Arias, M. Tobon-Henao, D. Collazos-Huertas, J. Daza-Castillo, N. Valencia-Marulanda, M. Calderón-Marulanda, O. Aguirre-Ospina, A. Alvarez-Meza, and G. Castellanos-Dominguez. FeetGUI: A Python-based Computer Vision Tool to Support Anesthesia Assessment Procedures Using Infrared Thermography. Advances in Artificial Intelligence–IBERAMIA 2022: 17th Ibero-American Conference on AI, Cartagena de Indias, Colombia, November 23–25, 2022, Proceedings. Cham: Springer International Publishing, 2023. (Conference paper)

APPENDIX

A

APPENDIX 1: FASTICA

Algorithm 1 FastICA

Input: Q Number of desired sources
Input: $\boldsymbol{X} \in \mathbb{R}^{C \times T}$ Prewhitened EEG signal, where $Q \leqq C$
Output: $\boldsymbol{O} \in \mathbb{R}^{C \times Q}$ Mixing matrix
Output: $\boldsymbol{S} \in \mathbb{R}^{Q \times T}$ Sources' matrix
for $q \leftarrow 1, Q$ **do**
    $\boldsymbol{o}_q \leftarrow$ Random vector $\in \mathbb{R}^{C \times 1}$
    while $\boldsymbol{o}_q$ Converges **do**
        $\boldsymbol{o}_q \leftarrow \frac{1}{T}\boldsymbol{X}\mathcal{G}'(\boldsymbol{o}_q^T\boldsymbol{X})^T - \frac{1}{T}\mathcal{G}''(\boldsymbol{o}_q^T\boldsymbol{X})\mathbf{1}_T\boldsymbol{o}_q$
        $\boldsymbol{o}_q \leftarrow \boldsymbol{o}_q - \sum_{j=1}^{q-1}(\boldsymbol{o}_q^T\boldsymbol{o}_j)\boldsymbol{o}_j$
        $\boldsymbol{o}_q \leftarrow \frac{\boldsymbol{o}_q}{\|\boldsymbol{o}_q\|_2}$
    end while
end for
Output $\boldsymbol{O} \leftarrow [\boldsymbol{o}_1, \ldots, \boldsymbol{o}_q]$
Output $\boldsymbol{S} \leftarrow \boldsymbol{O}^T\boldsymbol{X}$

where $\mathcal{G}'$ and $\mathcal{G}''$ represent the first and second derivatives of equation 2.2.1.

APPENDIX

B

APPENDIX 1: K-MEANS

In this appendix, we provide a detailed mathematical formulation of the K-means algorithm, a widely used clustering technique. The algorithm aims to partition a given dataset into $K \in \mathbb{N}$ distinct clusters based on their similarity. We present the main equations associated with the K-means algorithm, including the model, cost function, and the optimization procedure.

B.1 Model

Let us consider a dataset $\mathbf{X} = \{\mathbf{x}_n \in \mathbb{R}^D\}_{n=1}^N$ consisting of $N \in \mathbb{N}$ data points, where each $\mathbf{x}_n$ represents a $D \in \mathbb{N}$-dimensional feature vector. The goal of the K-means algorithm is to assign each data point to one of K clusters, with each cluster being represented by its centroid.

We denote the centroids of the clusters as $\mathbf{C} = \{\mathbf{c}_k \in \mathbb{R}^D\}_{k=1}^K$, where each $\mathbf{c}_k$ is a D-dimensional vector representing the centroid of the k-th cluster. The K-means algorithm seeks to find the optimal set of centroids that minimizes the within-cluster sum of squared distances.

B.2 Cost Function

The cost function used in the K-means algorithm quantifies the total sum of squared Euclidean distances between each data point and its assigned centroid. Let us define a binary indicator variable $r_{nk} \in \{0, 1\}$, which takes the value of 1 if data point $\mathbf{x}_n$ is assigned to cluster k and 0 otherwise. The cost function, denoted by J, is given by:

$$J = \sum_{n=1}^{N} \sum_{k=1}^{K} r_{nk} \|\mathbf{x}_n - \mathbf{c}_k\|_2^2 \tag{B-1}$$

The objective of the K-means algorithm is to minimize this cost function by finding the optimal assignments of data points to clusters and the corresponding centroids.

B.3 Optimization

To optimize the K-means cost function, we employ an iterative procedure that alternates between two steps: the assignment step and the update step.

B.3.1 Assignment Step

In the assignment step, each data point is assigned to the cluster with the nearest centroid. This assignment is based on the squared Euclidean distance between the data point and each centroid. The assignment of data point $\mathbf{x}_n$ to cluster k is determined by:

$$r_{nk} = \begin{cases} 1 & \text{if } k = \arg\min_j \|\mathbf{x}_n - \mathbf{c}_j\|_2^2 \\ 0 & \text{otherwise} \end{cases} \tag{B-2}$$

B.3.2 Update Step

In the update step, the centroids are recomputed based on the current assignments. The new centroid for cluster k is calculated as the mean of all data points assigned to that cluster:

$$\mathbf{c}_k = \frac{1}{\tau_k} \sum_{n=1}^{N} r_{nk} \mathbf{x}_n \tag{B-3}$$

where $\tau_k \in \mathbb{N}$ represents the number of data points assigned to cluster k.

These assignment and update steps are iteratively performed until convergence, which occurs when there is minimal change in the assignment of data points and the corresponding

APPENDIX

C

APPENDIX 1: T-SNE

In this appendix, we present the main equations and concepts related to the t-SNE algorithm. t-SNE is a powerful dimensionality reduction technique used for visualizing high-dimensional data in lower-dimensional space while preserving the local and global structure of the data. The algorithm is widely employed in various domains, including machine learning, data visualization, and exploratory data analysis.

C.1 Model

The t-SNE algorithm constructs a probability distribution over pairs of high-dimensional objects (e.g., data points) in such a way that similar objects have a high probability of being selected, while dissimilar objects have a low probability. It then constructs a similar probability distribution over pairs of points in a lower-dimensional map. The goal is to minimize the Kullback-Leibler (KL)

divergence between these two distributions, thereby preserving the neighborhood relationships between data points.

The t-SNE model computes pairwise similarities in the high-dimensional space using a Gaussian kernel. Let $\mathbf{X} = \{\mathbf{x}_n \in \mathbb{R}^D\}_{n=1}^N$ be the set of $N \in \mathbb{N}$ data points, where each $\mathbf{x}_n$ represents a $D \in \mathbb{N}$-high-dimensional vector. The pairwise similarity between $\mathbf{x}_n$ and $\mathbf{x}_m$ in the high-dimensional space is defined as:

$$p_{nm} = \begin{cases} \frac{\exp(-\|\mathbf{x}_n - \mathbf{x}_m\|^2 / 2\sigma_n^2)}{\sum_{j \neq n} \exp(-\|\mathbf{x}_n - \mathbf{x}_j\|^2 / 2\sigma_N^2)} & \text{if } n \neq m \\ 0 & \text{otherwise} \end{cases} \tag{C-1}$$

Note that $\sum_{m=1}^N p_{nm} = 1$ for all n.

Here, σ_n is the variance of the Gaussian kernel centered at $\mathbf{x}_n$. By default, σ_n is set to the median of the pairwise distances between $\mathbf{x}_n$ and all other data points.

In the low-dimensional space, the similarity between two points $\mathbf{y}_n$ and $\mathbf{y}_m \in \mathbb{R}^V$, where $V < D$, is defined using the Student t-distribution with a single degree of freedom. The pairwise similarity in the low-dimensional space is given by:

$$q_{nm} = \begin{cases} \frac{(1 + \|\mathbf{y}_n - \mathbf{y}_m\|^2)^{-1}}{\sum_j \sum_{j \neq l} (1 + \|\mathbf{y}_j - \mathbf{y}_l\|^2)^{-1}} & \text{if } n \neq m \\ 0 & \text{otherwise} \end{cases} \tag{C-2}$$

C.2 Cost Function and Optimization

To optimize the t-SNE model, we aim to minimize the KL divergence between the two distributions P and Q in the high-dimensional and low-dimensional spaces, respectively. The cost function for t-SNE is defined as:

$$\text{KL}(P \| Q) = \sum_{n \neq m} p_{nm} \log \frac{p_{nm}}{q_{nm}}$$

The optimization process involves finding a set of low-dimensional points $\mathbf{Y} = \{\mathbf{y}_n \in \mathbb{R}^V\}_{n=1}^N$ that minimizes the cost function $\mathrm{KL}(P\|Q)$. This is typically achieved using gradient descent optimization techniques.

BIBLIOGRAPHY

[Abhang et al., 2016] Abhang, P., Gawali, B., and Mehrotra, S. (2016). *Introduction to EEG-and speech-based emotion recognition*. Academic Press. (page 29)

[Abiri et al., 2019] Abiri, R., Borhani, S., Sellers, E. W., Jiang, Y., and Zhao, X. (2019). A comprehensive review of eeg-based brain–computer interface paradigms. *Journal of neural engineering*, 16(1):011001. (page 1)

[Achanccaray and Hayashibe, 2020] Achanccaray, D. and Hayashibe, M. (2020). Decoding hand motor imagery tasks within the same limb from eeg signals using deep learning. *IEEE Transactions on Medical Robotics and Bionics*, 2(4):692–699. (page 13)

[Altaheri et al., 2021] Altaheri, H., Muhammad, G., Alsulaiman, M., Amin, S. U., Altuwaijri, G. A., Abdul, W., Bencherif, M. A., and Faisal, M. (2021). Deep learning techniques for classification of electroencephalogram (eeg) motor imagery (mi) signals: A review. *Neural Computing and Applications*, pages 1–42. (page 10)

[Álvarez-Meza et al., 2017] Álvarez-Meza, A. M., Lee, J. A., Verleysen, M., and Castellanos-Dominguez, G. (2017). Kernel-based dimensionality reduction using renyi's α-entropy measures of similarity. *Neurocomputing*, 222:36–46. (page 47)

[Ang et al., 2008] Ang, K., Chin, Z., Zhang, H., and Guan, C. (2008). Filter bank common spatial pattern (FBCSP) in brain-computer interface. In *2008 IEEE international joint conference on neural networks*, pages 2390–2397. IEEE. (page 43)

[Artoni et al., 2018] Artoni, F., Delorme, A., and Makeig, S. (2018). Applying dimension reduction to eeg data by principal component analysis reduces the quality of its subsequent independent component decomposition. *NeuroImage*, 175:176–187. (page 8)

[Baig et al., 2017] Baig, M. Z., Aslam, N., Shum, H. P., and Zhang, L. (2017). Differential evolution algorithm as a tool for optimal feature subset selection in motor imagery eeg. *Expert Systems with Applications*, 90:184–195. (page 3)

[Bang and Lee, 2022] Bang, J.-S. and Lee, S.-W. (2022). Interpretable convolutional neural networks for subject-independent motor imagery classification. In *2022 10th International Winter Conference on Brain-Computer Interface (BCI)*, pages 1–5. IEEE. (page 14)

[Bashashati et al., 2007] Bashashati, A., Fatourechi, M., Ward, R. K., and Birch, G. E. (2007). A survey of signal processing algorithms in brain–computer interfaces based on electrical brain signals. *Journal of Neural engineering*, 4(2):R32. (pages 3 and 10)

[Benzy et al., 2020] Benzy, V., Vinod, A., Subasree, R., Alladi, S., and Raghavendra, K. (2020). Motor imagery hand movement direction decoding using brain computer interface to aid stroke recovery and rehabilitation. *IEEE Transactions on Neural Systems and Rehabilitation Engineering*, 28(12):3051–3062. (page 28)

[Berger and Zhou, 2014] Berger, V. W. and Zhou, Y. (2014). Kolmogorov–smirnov test: Overview. *Wiley statsref: Statistics reference online*. (pages 19 and 64)

[Berton et al., 2015] Berton, L., Valverde-Rebaza, J., and de Andrade Lopes, A. (2015). Link prediction in graph construction for supervised and semi-supervised learning. In *2015 International Joint Conference on Neural Networks (IJCNN)*, pages 1–8. IEEE. (page 11)

[Billinger et al., 2013] Billinger, M., Brunner, C., and Müller-Putz, G. R. (2013). Single-trial connectivity estimation for classification of motor imagery data. *Journal of neural engineering*, 10(4):046006. (page 28)

[Brunner et al., 2008] Brunner, C., Leeb, R., Müller-Putz, G., Schlögl, A., Pfurtscheller, G., and Competition, B. (2008). Graz data set a, provided by the institute for knowledge discovery (laboratory of brain–computer interfaces). *Graz University of Technology*. (page 19)

[Cai et al., 2010] Cai, D., He, X., Han, J., and Huang, T. S. (2010). Graph regularized nonnegative matrix factorization for data representation. *IEEE transactions on pattern analysis and machine intelligence*, 33(8):1548–1560. (page 11)

[Caicedo-Acosta et al., 2021] Caicedo-Acosta, J., Castaño, G. A., Acosta-Medina, C., Alvarez-Meza, A., and Castellanos-Dominguez, G. (2021). Deep neural regression prediction of motor imagery skills using eeg functional connectivity indicators. *Sensors*, 21(6):1932. (page 6)

[Carvalhaes and De Barros, 2015] Carvalhaes, C. and De Barros, J. (2015). The surface laplacian technique in EEG: Theory and methods. *International Journal of Psychophysiology*, 97(3):174–188. (page 25)

[Cho et al., 2017] Cho, H., Ahn, M., Ahn, S., et al. (2017). Supporting data for "eeg datasets for motor imagery brain computer interface.". *GigaScience Database*. (pages 19 and 37)

[Cohen, 2014] Cohen, M. (2014). *Analyzing neural time series data: theory and practice*. MIT press. (page 31)

[Cohen, 2015] Cohen, M. (2015). Effects of time lag and frequency matching on phase-based connectivity. *Journal of neuroscience methods*, 250:137–146. (page 31)

[Collazos-Huertas et al., 2020] Collazos-Huertas, D., Caicedo-Acosta, J., Castaño-Duque, G. A., and Acosta-Medina, C. D. (2020). Enhanced multiple instance representation using time-frequency atoms in motor imagery classification. *Frontiers in Neuroscience*, 14:155. (page 13)

[Collazos-Huertas et al., 2023] Collazos-Huertas, D. F., Álvarez-Meza, A. M., Cárdenas-Peña, D. A., Castaño-Duque, G. A., and Castellanos-Domínguez, C. G. (2023). Posthoc interpretability of neural responses by grouping subject motor imagery skills using cnn-based connectivity. *Sensors*, 23(5):2750. (pages 4 and 7)

[Collazos-Huertas et al., 2021a] Collazos-Huertas, D. F., Álvarez-Meza, A. M., and Castellanos-Dominguez, G. (2021a). Spatial interpretability of time-frequency relevance optimized in motor imagery discrimination using deep&wide networks. *Biomedical Signal Processing and Control*, 68:102626. (page 5)

[Collazos-Huertas et al., 2021b] Collazos-Huertas, D. F., Velasquez-Martinez, L. F., Perez-Nastar, H. D., Alvarez-Meza, A. M., and Castellanos-Dominguez, G. (2021b). Deep and wide transfer learning with kernel matching for pooling data from electroencephalography and psychological questionnaires. *Sensors*, 21(15):5105. (pages 12 and 35)

[Cona et al., 2009] Cona, F., Zavaglia, M., Astolfi, L., Babiloni, F., and Ursino, M. (2009). Changes in eeg power spectral density and cortical connectivity in healthy and tetraplegic patients during a motor imagery task. *Computational intelligence and neuroscience*, 2009. (page 12)

[Cortes et al., 2012] Cortes, C., Mohri, M., and Rostamizadeh, A. (2012). Algorithms for learning kernels based on centered alignment. *The Journal of Machine Learning Research*, 13(1):795–828. (page 47)

[Dagdevir and Tokmakci, 2021] Dagdevir, E. and Tokmakci, M. (2021). Optimization of preprocessing stage in EEG based BCI systems in terms of accuracy and timing cost. *Biomedical Signal Processing and Control*, 67:102548. (page 38)

[Dai et al., 2020] Dai, G., Zhou, J., Huang, J., and Wang, N. (2020). Hs-cnn: a cnn with hybrid convolution scale for eeg motor imagery classification. *Journal of neural engineering*, 17(1):016025. (page 1)

[Deng et al., 2021] Deng, X., Zhang, B., Yu, N., Liu, K., and Sun, K. (2021). Advanced tsgl-eegnet for motor imagery eeg-based brain-computer interfaces. *IEEE Access*, 9:25118–25130. (page 14)

[dos Santos et al., 2020] dos Santos, E. M., Cassani, R., Falk, T. H., and Fraga, F. J. (2020). Improved motor imagery brain-computer interface performance via adaptive modulation filtering and two-stage classification. *Biomedical Signal Processing and Control*, 57:101812. (page 9)

[Engmann and Cousineau, 2011] Engmann, S. and Cousineau, D. (2011). Comparing distributions: the two-sample anderson-darling test as an alternative to the kolmogorov-smirnoff test. *Journal of applied quantitative methods*, 6(3). (page 64)

[Ganin et al., 2016] Ganin, Y., Ustinova, E., Ajakan, H., Germain, P., Larochelle, H., Laviolette, F., Marchand, M., and Lempitsky, V. (2016). Domain-adversarial training of neural networks. *The journal of machine learning research*, 17(1):2096–2030. (page 11)

[García-Murillo et al., 2021] García-Murillo, D., Alvarez-Meza, A., and Castellanos-Dominguez, G. (2021). Single-trial kernel-based functional connectivity for enhanced feature extraction in motor-related tasks. *Sensors*, 21(8):2750. (pages 18 and 27)

[García-Murillo et al., 2023] García-Murillo, D. G., Álvarez-Meza, A. M., and Castellanos-Dominguez, C. G. (2023). Kcs-fcnet: Kernel cross-spectral functional connectivity network for eeg-based motor imagery classification. *Diagnostics*, 13(6):1122. (pages 4, 14, 48, 52, and 55)

[Gaur et al., 2021] Gaur, P., McCreadie, K., Pachori, R. B., Wang, H., and Prasad, G. (2021). An automatic subject specific channel selection method for enhancing motor imagery classification in eeg-bci using correlation. *Biomedical Signal Processing and Control*, 68:102574. (page 1)

[Géron, 2019] Géron, A. (2019). *Hands-on machine learning with Scikit-Learn, Keras, and TensorFlow: Concepts, tools, and techniques to build intelligent systems*. " O'Reilly Media, Inc.". (page 33)

[Géron, 2022] Géron, A. (2022). *Hands-on machine learning with Scikit-Learn, Keras, and TensorFlow*. " O'Reilly Media, Inc.". (pages 48, 52, and 55)

[Ghosh et al., 2015] Ghosh, P., Mazumder, A., Bhattacharyya, S., Tibarewala, D. N., and Hayashibe, M. (2015). Functional connectivity analysis of motor imagery eeg signal for brain-computer interfacing application. In *2015 7th International IEEE/EMBS Conference on Neural Engineering (NER)*, pages 210–213. IEEE. (page 2)

[Giraldo et al., 2014] Giraldo, L. G. S., Rao, M., and Principe, J. C. (2014). Measures of entropy from data using infinitely divisible kernels. *IEEE Transactions on Information Theory*, 61(1):535–548. (page 70)

[Halme and Parkkonen, 2018] Halme, H.-L. and Parkkonen, L. (2018). Across-subject offline decoding of motor imagery from meg and eeg. *Scientific reports*, 8(1):10087. (page 11)

[Hamedi et al., 2016] Hamedi, M., Salleh, S.-H., and Noor, A. M. (2016). Electroencephalographic motor imagery brain connectivity analysis for bci: a review. *Neural computation*, 28(6):999–1041. (pages 2 and 19)

[Han et al., 2019] Han, C.-H., Kim, Y.-W., Kim, D. Y., Kim, S. H., Nenadic, Z., and Im, C.-H. (2019). Electroencephalography-based endogenous brain–computer interface for online communication with a completely locked-in patient. *Journal of neuroengineering and rehabilitation*, 16:1–13. (page 5)

[Hashem et al., 2023] Hashem, H. A., Abdulazeem, Y., Labib, L. M., Elhosseini, M. A., and Shehata, M. (2023). An integrated machine learning-based brain computer interface to classify diverse limb motor tasks: Explainable model. *Sensors*, 23(6):3171. (page 4)

[He et al., 2022] He, Y., Lu, Z., Wang, J., and Shi, J. (2022). A channel attention based mlp-mixer network for motor imagery decoding with eeg. In *ICASSP 2022-2022 IEEE International Conference on Acoustics, Speech and Signal Processing (ICASSP)*, pages 1291–1295. IEEE. (page 10)

[Hooi et al., 2015] Hooi, L. S., Nisar, H., and Voon, Y. V. (2015). Tracking of eeg activity using topographic maps. In *2015 IEEE International Conference on Signal and Image Processing Applications (ICSIPA)*, pages 287–291. IEEE. (page 65)

[Hsu, 2013] Hsu, W. (2013). Wavelet-coherence features for motor imagery EEG analysis posterior to EOG noise elimination. *Int J Innov Comput Inform Control*, 9:465–475. (page 28)

[Hsu, 2014] Hsu, W.-Y. (2014). Improving classification accuracy of motor imagery eeg using genetic feature selection. *Clinical EEG and neuroscience*, 45(3):163–168. (page 10)

[Hu et al., 2023] Hu, H., Yue, K., Guo, M., Lu, K., and Liu, Y. (2023). Subject separation network for reducing calibration time of mi-based bci. *Brain Sciences*, 13(2):221. (page 3)

[Huang et al., 2019] Huang, Y.-C., Chang, J.-R., Chen, L.-F., and Chen, Y.-S. (2019). Deep neural network with attention mechanism for classification of motor imagery eeg. In *2019 9th International IEEE/EMBS Conference on Neural Engineering (NER)*, pages 1130–1133. IEEE. (page 11)

[Hyvärinen and Oja, 2000] Hyvärinen, A. and Oja, E. (2000). Independent component analysis: algorithms and applications. *Neural networks*, 13(4-5):411–430. (page 30)

[Ince et al., 2007] Ince, N. F., Tewfik, A. H., and Arica, S. (2007). Extraction subject-specific motor imagery time–frequency patterns for single trial eeg classification. *Computers in biology and medicine*, 37(4):499–508. (page 8)

[Ioffe and Szegedy, 2015] Ioffe, S. and Szegedy, C. (2015). Batch normalization: Accelerating deep network training by reducing internal covariate shift. In *International conference on machine learning*, pages 448–456. pmlr. (page 11)

[Jafarifarmand and Badamchizadeh, 2020] Jafarifarmand, A. and Badamchizadeh, M. (2020). Real-time multiclass motor imagery brain-computer interface by modified common spatial patterns and adaptive neuro-fuzzy classifier. *Biomedical Signal Processing and Control*, 57:101749. (page 43)

[Jafarifarmand et al., 2017] Jafarifarmand, A., Badamchizadeh, M., Khanmohammadi, S., Nazari, M., and Tazehkand, B. (2017). A new self-regulated neuro-fuzzy framework for classification of EEG signals in motor imagery BCI. *IEEE transactions on fuzzy systems*, 26(3):1485–1497. (page 30)

[Jeong et al., 2021] Jeong, J., Choi, J., Kim, K., Lee, S., Kim, D., and Kim, H. (2021). Multi-domain convolutional neural networks for lower-limb motor imagery using dry vs. wet electrodes. *Sensors*, 21(19):6672. (page 43)

[Kanna and Vasuki, 2021] Kanna, R. K. and Vasuki, R. (2021). Classification of brain signals using classifiers for automated wheelchair application. *International Journal of Modern Agriculture*, 10(2):2426–2431. (page 1)

[Kaur and Kaur, 2015] Kaur, J. and Kaur, A. (2015). A review on analysis of eeg signals. In *2015 International Conference on Advances in Computer Engineering and Applications*, pages 957–960. IEEE. (page 2)

[Kayser and Tenke, 2015] Kayser, J. and Tenke, C. E. (2015). Issues and considerations for using the scalp surface laplacian in eeg/erp research: A tutorial review. *International Journal of Psychophysiology*, 97(3):189–209. (page 2)

[Kevric and Subasi, 2017] Kevric, J. and Subasi, A. (2017). Comparison of signal decomposition methods in classification of eeg signals for motor-imagery bci system. *Biomedical Signal Processing and Control*, 31:398–406. (page 2)

[Khan et al., 2020] Khan, M. A., Das, R., Iversen, H. K., and Puthusserypady, S. (2020). Review on motor imagery based bci systems for upper limb post-stroke neurorehabilitation: From designing to application. *Computers in Biology and Medicine*, 123:103843. (page 1)

[Ko et al., 2021] Ko, W., Jeon, E., Jeong, S., and Suk, H. (2021). Multi-scale neural network for EEG representation learning in BCI. *IEEE Computational Intelligence Magazine*, 16(2):31–45. (page 43)

[Ko et al., 2018] Ko, W., Yoon, J., Kang, E., Jun, E., Choi, J., and Suk, H. (2018). Deep recurrent spatio-temporal neural network for motor imagery based BCI. In *2018 6th International Conference on Brain-Computer Interface (BCI)*, pages 1–3. IEEE. (page 43)

[Kong et al., 2021] Kong, Q., Wu, Y., Yuan, C., and Wang, Y. (2021). Ct-cad: Context-aware transformers for end-to-end chest abnormality detection on x-rays. In *2021 IEEE International Conference on Bioinformatics and Biomedicine (BIBM)*, pages 1385–1388. IEEE. (page 11)

[Kotte and Dabbakuti, 2020] Kotte, S. and Dabbakuti, J. K. (2020). Methods for removal of artifacts from eeg signal: A review. In *Journal of Physics: Conference Series*, volume 1706, page 012093. IOP Publishing. (page 8)

[Krusienski et al., 2006] Krusienski, D. J., McFarland, D. J., and Wolpaw, J. R. (2006). An evaluation of autoregressive spectral estimation model order for brain-computer interface applications. In *2006 International Conference of the IEEE Engineering in Medicine and Biology Society*, pages 1323–1326. IEEE. (page 2)

[Kumar and Jayanthi, 2020] Kumar, M. and Jayanthi, V. (2020). Blind source separation using kurtosis, negentropy and maximum likelihood functions. *International Journal of Speech Technology*, 23(1):13–21. (page 25)

[Kumar et al., 2017] Kumar, S., Sharma, A., and Tsunoda, T. (2017). An improved discriminative filter bank selection approach for motor imagery eeg signal classification using mutual information. *BMC bioinformatics*, 18:125–137. (page 3)

[Kumar et al., 2021] Kumar, S., Sharma, R., and Sharma, A. (2021). OPTICAL+: a frequency-based deep learning scheme for recognizing brain wave signals. *PeerJ Computer Science*, 7:e375. (page 43)

[Kwon et al., 2019] Kwon, M., Han, S., Kim, K., and Jun, S. C. (2019). Super-resolution for improving eeg spatial resolution using deep convolutional neural network—feasibility study. *Sensors*, 19(23):5317. (page 8)

[Lahane et al., 2019] Lahane, P., Jagtap, J., Inamdar, A., Karne, N., and Dev, R. (2019). A review of recent trends in eeg based brain-computer interface. In *2019 International Conference on Computational Intelligence in Data Science (ICCIDS)*, pages 1–6. IEEE. (page 8)

[Lance et al., 2012] Lance, B. J., Kerick, S. E., Ries, A. J., Oie, K. S., and McDowell, K. (2012). Brain–computer interface technologies in the coming decades. *Proceedings of the IEEE*, 100(Special Centennial Issue):1585–1599. (page 10)

[Lawhern et al., 2018] Lawhern, V. J., Solon, A. J., Waytowich, N. R., Gordon, S. M., Hung, C. P., and Lance, B. J. (2018). Eegnet: a compact convolutional neural network for eeg-based brain–computer interfaces. *Journal of neural engineering*, 15(5):056013. (pages 3, 18, 43, 49, 52, 53, and 61)

[Li et al., 2022] Li, H., Liu, M., Yu, X., Zhu, J., Wang, C., Chen, X., Feng, C., Leng, J., Zhang, Y., and Xu, F. (2022). Coherence based graph convolution network for motor imagery-induced eeg after spinal cord injury. *Frontiers in Neuroscience*, 16. (page 13)

[Li and Ruan, 2021] Li, M.-a. and Ruan, Z.-w. (2021). A novel decoding method for motor imagery tasks with 4d data representation and 3d convolutional neural networks. *Journal of Neural Engineering*, 18(4):046029. (page 14)

[Liu et al., 2017] Liu, A., Chen, K., Liu, Q., Ai, Q., Xie, Y., and Chen, A. (2017). Feature selection for motor imagery eeg classification based on firefly algorithm and learning automata. *Sensors*, 17(11):2576. (page 3)

[Liu et al., 2022] Liu, G., Tian, L., and Zhou, W. (2022). Multiscale time-frequency method for multiclass motor imagery brain computer interface. *Computers in Biology and Medicine*, 143:105299. (page 7)

[LK Jaya Shree, 2021] LK Jaya Shree, B. (2021). Automatic detection of eeg as biomarker using deep learning: A review. *Annals of the Romanian Society for Cell Biology*, pages 6502–6511. (page 6)

[Lotte et al., 2007] Lotte, F., Congedo, M., Lécuyer, A., Lamarche, F., and Arnaldi, B. (2007). A review of classification algorithms for eeg-based brain–computer interfaces. *Journal of neural engineering*, 4(2):R1. (pages 3 and 10)

[Ma et al., 2022] Ma, Y., Bian, D., Xu, D., Zou, W., Wang, J., and Hu, N. (2022). A spatio-temporal interactive attention network for motor imagery eeg decoding. In *2022 IEEE International Conference on Signal Processing, Communications and Computing (ICSPCC)*, pages 1–6. IEEE. (page 10)

[Marks and Isaac, 1995] Marks, D. F. and Isaac, A. R. (1995). Topographical distribution of eeg activity accompanying visual and motor imagery in vivid and non-vivid imagers. *British Journal of Psychology*, 86(2):271–282. (page 13)

[Marquand et al., 2014] Marquand, A. F., Brammer, M., Williams, S. C., and Doyle, O. M. (2014). Bayesian multi-task learning for decoding multi-subject neuroimaging data. *NeuroImage*, 92:298–311. (page 11)

[McFarland et al., 2006] McFarland, D. J., Anderson, C. W., Muller, K.-R., Schlogl, A., and Krusienski, D. J. (2006). Bci meeting 2005-workshop on bci signal processing: feature extraction and translation. *IEEE transactions on neural systems and rehabilitation engineering*, 14(2):135–138. (page 3)

[Meng et al., 2022] Meng, C., Trinh, L., Xu, N., Enouen, J., and Liu, Y. (2022). Interpretability and fairness evaluation of deep learning models on mimic-iv dataset. *Scientific Reports*, 12(1):7166. (page 7)

[Miao et al., 2020] Miao, M., Hu, W., Yin, H., and Zhang, K. (2020). Spatial-frequency feature learning and classification of motor imagery eeg based on deep convolution neural network. *Computational and mathematical methods in medicine*, 2020. (page 1)

[Mishuhina and Jiang, 2018] Mishuhina, V. and Jiang, X. (2018). Feature weighting and regularization of common spatial patterns in eeg-based motor imagery bci. *IEEE Signal Processing Letters*, 25(6):783–787. (page 13)

[Mridha et al., 2021] Mridha, M., Das, S. C., Kabir, M. M., Lima, A. A., Islam, M., Watanobe, Y., et al. (2021). Brain-computer interface: Advancement and challenges. *Sensors*, 21(17):5746. (pages 9 and 11)

[Müller et al., 2004] Müller, K.-R., Krauledat, M., Dornhege, G., Curio, G., and Blankertz, B. (2004). Machine learning techniques for brain-computer interfaces. *Biomed. Tech*, 49(1):11–22. (page 7)

[Musallam et al., 2021] Musallam, Y. K., AlFassam, N. I., Muhammad, G., Amin, S. U., Alsulaiman, M., Abdul, W., Altaheri, H., Bencherif, M. A., and Algabri, M. (2021). Electroencephalography-based motor imagery classification using temporal convolutional network fusion. *Biomedical Signal Processing and Control*, 69:102826. (pages 3, 54, and 61)

[Naeem et al., 2006] Naeem, M., Brunner, C., Leeb, R., Graimann, B., and Pfurtscheller, G. (2006). Seperability of four-class motor imagery data using independent components analysis. *Journal of neural engineering*, 3(3):208. (page 13)

[Oikonomou et al., 2017] Oikonomou, V. P., Georgiadis, K., Liaros, G., Nikolopoulos, S., and Kompatsiaris, I. (2017). A comparison study on eeg signal processing techniques using motor imagery eeg data. In *2017 IEEE 30th international symposium on computer-based medical systems (CBMS)*, pages 781–786. IEEE. (page 3)

[Padfield et al., 2019] Padfield, N., Zabalza, J., Zhao, H., Masero, V., and Ren, J. (2019). Eeg-based brain-computer interfaces using motor-imagery: Techniques and challenges. *Sensors*, 19(6):1423. (page 2)

[Park et al., 2021] Park, S., Ha, J., Kim, D.-H., and Kim, L. (2021). Improving motor imagery-based brain-computer interface performance based on sensory stimulation training: an approach focused on poorly performing users. *Frontiers in Neuroscience*, 15:732545. (page 33)

[Pérez-Velasco et al., 2022] Pérez-Velasco, S., Santamaria-Vazquez, E., Martinez-Cagigal, V., Marcos-Martinez, D., and Hornero, R. (2022). Eegsym: Overcoming inter-subject variability in motor imagery based bcis with deep learning. *IEEE Transactions on Neural Systems and Rehabilitation Engineering*, 30:1766–1775. (page 6)

[Phang and Ko, 2020] Phang, C.-R. and Ko, L.-W. (2020). Global cortical network distinguishes motor imagination of the left and right foot. *IEEE Access*, 8:103734–103745. (page 13)

[Phunruangsakao et al., 2022] Phunruangsakao, C., Achanccaray, D., and Hayashibe, M. (2022). Deep adversarial domain adaptation with few-shot learning for motor-imagery brain-computer interface. *IEEE Access*, 10:57255–57265. (page 11)

[Poldrack, 2011] Poldrack, R. A. (2011). Inferring mental states from neuroimaging data: from reverse inference to large-scale decoding. *Neuron*, 72(5):692–697. (page 13)

[Rajabioun, 2020] Rajabioun, M. (2020). Motor imagery classification by active source dynamics. *Biomedical Signal Processing and Control*, 61:102028. (page 9)

[Rashid et al., 2020] Rashid, M., Sulaiman, N., PP Abdul Majeed, A., Musa, R. M., Bari, B. S., Khatun, S., et al. (2020). Current status, challenges, and possible solutions of eeg-based brain-computer interface: a comprehensive review. *Frontiers in neurorobotics*, 14:25. (pages 8 and 17)

[Rathee et al., 2017] Rathee, D., Raza, H., Prasad, G., and Cecotti, H. (2017). Current source density estimation enhances the performance of motor-imagery-related brain–computer interface. *IEEE Transactions on Neural Systems and Rehabilitation Engineering*, 25(12):2461–2471. (page 34)

[Repov, 2010] Repov, G. (2010). Dealing with noise in eeg recording and data analysis spoprijemanje s umom pri zajemanju in analizi eeg signala. In *Informatica medica slovenica*, number 15, page 18. (page 9)

[Rodrigues et al., 2019] Rodrigues, P., Stefano Filho, C., Attux, R., Castellano, G., and Soriano, D. (2019). Space-time recurrences for functional connectivity evaluation and feature extraction in motor imagery brain-computer interfaces. *Medical & biological engineering & computing*, 57(8):1709–1725. (page 43)

[Rosário et al., 2015] Rosário, R., Cardoso, P., Muñoz, M., Montoya, P., and Miranda, J. (2015). Motif-synchronization: A new method for analysis of dynamic brain networks with EEG. *Physica A: Statistical Mechanics and its Applications*, 439:7–19. (page 29)

[Roy et al., 2020] Roy, S., Chowdhury, A., McCreadie, K., and Prasad, G. (2020). Deep learning based inter-subject continuous decoding of motor imagery for practical brain-computer interfaces. *Frontiers in Neuroscience*, 14:918. (page 11)

[Roy et al., 2019] Roy, Y., Banville, H., Albuquerque, I., Gramfort, A., Falk, T. H., and Faubert, J. (2019). Deep learning-based electroencephalography analysis: a systematic review. *Journal of neural engineering*, 16(5):051001. (page 6)

[Ruiz-Gómez et al., 2019] Ruiz-Gómez, S. J., Hornero, R., Poza, J., Maturana-Candelas, A., Pinto, N., and Gómez, C. (2019). Computational modeling of the effects of eeg volume conduction on functional connectivity metrics. application to alzheimer's disease continuum. *Journal of neural engineering*, 16(6):066019. (page 13)

[Sadiq et al., 2019] Sadiq, M. T., Yu, X., Yuan, Z., Fan, Z., Rehman, A. U., Li, G., and Xiao, G. (2019). Motor imagery eeg signals classification based on mode amplitude and frequency components using empirical wavelet transform. *IEEE access*, 7:127678–127692. (page 10)

[Saha and Baumert, 2020] Saha, S. and Baumert, M. (2020). Intra-and inter-subject variability in eeg-based sensorimotor brain computer interface: a review. *Frontiers in computational neuroscience*, 13:87. (page 5)

[Sahu et al., 2021] Sahu, M., Mohdiwale, S., Khoriya, N., Upadhyay, Y., Verma, A., and Singh, S. (2021). Eeg artifact removal techniques: a comparative study. In *International Conference on Innovative Computing and Communications: Proceedings of ICICC 2020, Volume 2*, pages 395–403. Springer. (page 2)

[Sakkaff and Nanayakkara, 2008] Sakkaff, Z. and Nanayakkara, A. (2008). Removal of ocular artifacts from eeg signals in brain computer interface. In *Proceedings of the Technical Sessions*, volume 24, pages 51–57. (page 2)

[Salami et al., 2022] Salami, A., Andreu-Perez, J., and Gillmeister, H. (2022). Eeg-itnet: An explainable inception temporal convolutional network for motor imagery classification. *IEEE Access*, 10:36672–36685. (page 5)

[Samek et al., 2017] Samek, W., Wiegand, T., and Müller, K.-R. (2017). Explainable artificial intelligence: Understanding, visualizing and interpreting deep learning models. *arXiv preprint arXiv:1708.08296*. (page 3)

[Sannelli et al., 2019] Sannelli, C., Vidaurre, C., Müller, K.-R., and Blankertz, B. (2019). A large scale screening study with a smr-based bci: Categorization of bci users and differences in their smr activity. *PLoS One*, 14(1):e0207351. (page 6)

[Schirrmeister et al., 2017] Schirrmeister, R. T., Springenberg, J. T., Fiederer, L. D. J., Glasstetter, M., Eggensperger, K., Tangermann, M., Hutter, F., Burgard, W., and Ball, T. (2017). Deep learning with convolutional neural networks for eeg decoding and visualization. *Human brain mapping*, 38(11):5391–5420. (pages 3, 53, 54, and 61)

[Seghier and Price, 2018] Seghier, M. L. and Price, C. J. (2018). Interpreting and utilising intersubject variability in brain function. *Trends in cognitive sciences*, 22(6):517–530. (page 6)

[Shamsi et al., 2021] Shamsi, F., Haddad, A., and Najafizadeh, L. (2021). Early classification of motor tasks using dynamic functional connectivity graphs from EEG. *Journal of neural engineering*, 18(1):016015. (page 27)

[Shoka et al., 2019] Shoka, A., Dessouky, M., El-Sherbeny, A., and El-Sayed, A. (2019). Literature review on eeg preprocessing, feature extraction, and classifications techniques. *Menoufia J. Electron. Eng. Res*, 28(1):292–299. (page 6)

[Singh et al., 2021] Singh, A., Hussain, A. A., Lal, S., and Guesgen, H. W. (2021). A comprehensive review on critical issues and possible solutions of motor imagery based electroencephalography brain-computer interface. *Sensors*, 21(6):2173. (page 8)

[Somers et al., 2018] Somers, B., Francart, T., and Bertrand, A. (2018). A generic eeg artifact removal algorithm based on the multi-channel wiener filter. *Journal of neural engineering*, 15(3):036007. (page 8)

[Song et al., 2021] Song, Y., Jia, X., Yang, L., and Xie, L. (2021). Transformer-based spatial-temporal feature learning for eeg decoding. *arXiv preprint arXiv:2106.11170*. (page 10)

[Song et al., 2019] Song, Y., Wang, D., Yue, K., Zheng, N., and Shen, Z.-J. M. (2019). Eeg-based motor imagery classification with deep multi-task learning. In *2019 International Joint Conference on Neural Networks (IJCNN)*, pages 1–8. IEEE. (page 10)

[Srivastava et al., 2014] Srivastava, N., Hinton, G., Krizhevsky, A., Sutskever, I., and Salakhutdinov, R. (2014). Dropout: a simple way to prevent neural networks from overfitting. *The journal of machine learning research*, 15(1):1929–1958. (page 11)

[Steenbergen et al., 2020] Steenbergen, B., Krajenbrink, H., Lust, J., and Wilson, P. (2020). Motor imagery and action observation for predictive control in developmental coordination disorder. *Developmental Medicine & Child Neurology*, 62(12):1352–1355. (page 1)

[Stefano-Filho et al., 2017] Stefano-Filho, C., Attux, R., and Castellano, G. (2017). EEG sensorimotor rhythms' variation and functional connectivity measures during motor imagery: linear relations and classification approaches. *PeerJ*, 5:e3983. (page 27)

[Stergiadis et al., 2022] Stergiadis, C., Kostaridou, V.-D., and Klados, M. A. (2022). Which bss method separates better the eeg signals? a comparison of five different algorithms. *Biomedical Signal Processing and Control*, 72:103292. (page 8)

[Sturm et al., 2016] Sturm, I., Lapuschkin, S., Samek, W., and Müller, K.-R. (2016). Interpretable deep neural networks for single-trial eeg classification. *Journal of neuroscience methods*, 274:141–145. (page 14)

[Subirats et al., 2018] Subirats, L., Allali, G., Briansoulet, M., Salle, J., and Perrochon, A. (2018). Age and gender differences in motor imagery. *Journal of the neurological sciences*, 391:114–117. (page 6)

[Sun et al., 2022] Sun, B., Liu, Z., Wu, Z., Mu, C., and Li, T. (2022). Graph convolution neural network based end-to-end channel selection and classification for motor imagery brain-computer interfaces. *IEEE Transactions on Industrial Informatics*. (page 10)

[Sun et al., 2021] Sun, J., Xie, J., and Zhou, H. (2021). Eeg classification with transformer-based models. In *2021 ieee 3rd global conference on life sciences and technologies (lifetech)*, pages 92–93. IEEE. (page 11)

[Tabar and Halici, 2016] Tabar, Y. R. and Halici, U. (2016). A novel deep learning approach for classification of eeg motor imagery signals. *Journal of neural engineering*, 14(1):016003. (page 2)

[Taran and Bajaj, 2019] Taran, S. and Bajaj, V. (2019). Motor imagery tasks-based eeg signals classification using tunable-q wavelet transform. *Neural Computing and Applications*, 31:6925–6932. (page 9)

[Tayeb et al., 2019] Tayeb, Z., Fedjaev, J., Ghaboosi, N., Richter, C., Everding, L., Qu, X., Wu, Y., Cheng, G., and Conradt, J. (2019). Validating deep neural networks for online decoding of motor imagery movements from eeg signals. *Sensors*, 19(1):210. (page 13)

[Teng et al., 2022] Teng, Q., Liu, Z., Song, Y., Han, K., and Lu, Y. (2022). A survey on the interpretability of deep learning in medical diagnosis. *Multimedia Systems*, pages 1–21. (page 7)

[Tobón-Henao et al., 2022] Tobón-Henao, M., Álvarez-Meza, A., and Castellanos-Domínguez, G. (2022). Subject-dependent artifact removal for enhancing motor imagery classifier performance under poor skills. *Sensors*, 22(15):5771. (page 9)

[Uribe et al., 2019] Uribe, L. F. S., Stefano Filho, C. A., de Oliveira, V. A., da Silva Costa, T. B., Rodrigues, P. G., Soriano, D. C., Boccato, L., Castellano, G., and Attux, R. (2019). A correntropy-based classifier for motor imagery brain-computer interfaces. *Biomedical Physics & Engineering Express*, 5(6):065026. (page 9)

[Valencia-Marin et al., 2021] Valencia-Marin, C., Pulgarin-Giraldo, J., Velasquez-Martinez, L., Alvarez-Meza, A., and Castellanos-Dominguez, G. (2021). An enhanced joint hilbert embedding-based metric to support mocap data classification with preserved interpretability. *Sensors*, 21(13):4443. (page 29)

[Van Erp et al., 2012] Van Erp, J., Lotte, F., and Tangermann, M. (2012). Brain-computer interfaces: beyond medical applications. *Computer*, 45(4):26–34. (page 10)

[Velasquez-Martinez et al., 2020a] Velasquez-Martinez, L., Caicedo-Acosta, J., and Castellanos-Dominguez, G. (2020a). Entropy-based estimation of event-related de/synchronization in motor imagery using vector-quantized patterns. *Entropy*, 22(6):703. (page 37)

[Velasquez-Martinez et al., 2018] Velasquez-Martinez, L. F., Zapata-Castaño, F., Cárdenas-Peña, D., and Castellanos-Dominguez, G. (2018). Detecting eeg dynamic changes using supervised temporal patterns. In *Progress in Artificial Intelligence and Pattern Recognition: 6th International Workshop, IWAIPR 2018, Havana, Cuba, September 24–26, 2018, Proceedings 6*, pages 351–358. Springer. (page 13)

[Velasquez-Martinez et al., 2020b] Velasquez-Martinez, L. F., Zapata-Castano, F., and Castellanos-Dominguez, G. (2020b). Dynamic modeling of common brain neural activity in motor imagery tasks. *Frontiers in Neuroscience*, 14:714. (page 12)

[Venkatachalam et al., 2020] Venkatachalam, K., Devipriya, A., Maniraj, J., Sivaram, M., Ambikapathy, A., and Iraj, S. A. (2020). A novel method of motor imagery classification using eeg signal. *Artificial intelligence in medicine*, 103:101787. (page 1)

[Vidaurre and Blankertz, 2010] Vidaurre, C. and Blankertz, B. (2010). Towards a cure for bci illiteracy. *Brain topography*, 23:194–198. (page 6)

[Vrbik, 2020] Vrbik, J. (2020). Deriving cdf of kolmogorov-smirnov test statistic. *Applied Mathematics*, 11(3):227–246. (page 64)

[Wang et al., 2015a] Wang, G., Teng, C., Li, K., Zhang, Z., and Yan, X. (2015a). The removal of eog artifacts from eeg signals using independent component analysis and multivariate empirical mode decomposition. *IEEE journal of biomedical and health informatics*, 20(5):1301–1308. (page 2)

[Wang et al., 2017] Wang, K., Wang, Z., Guo, Y., He, F., Qi, H., Xu, M., and Ming, D. (2017). A brain-computer interface driven by imagining different force loads on a single hand: an online feasibility study. *Journal of neuroengineering and rehabilitation*, 14(1):1–10. (page 1)

[Wang et al., 2015b] Wang, T., Zhao, D., and Tian, S. (2015b). An overview of kernel alignment and its applications. *Artificial Intelligence Review*, 43:179–192. (page 18)

[Wang et al., 2014] Wang, Y., Li, X., Li, H., Shao, C., Ying, L., and Wu, S. (2014). Feature extraction of motor imagery electroencephalography based on time-frequency-space domains. *Sheng wu yi xue gong cheng xue za zhi= Journal of biomedical engineering= Shengwu yixue gongchengxue zazhi*, 31(5):955–961. (page 2)

[Wei and Lin, 2020] Wei, M. and Lin, F. (2020). A novel multi-dimensional features fusion algorithm for the EEG signal recognition of brain's sensorimotor region activated tasks. *International Journal of Intelligent Computing and Cybernetics*. (page 43)

[Wilson et al., 2019] Wilson, R., Mullinger, K. J., Francis, S. T., and Mayhew, S. D. (2019). The relationship between negative bold responses and ers and erd of alpha/beta oscillations in visual and motor cortex. *Neuroimage*, 199:635–650. (page 12)

[Xu et al., 2018] Xu, B., Zhang, L., Song, A., Wu, C., Li, W., Zhang, D., Xu, G., Li, H., and Zeng, H. (2018). Wavelet transform time-frequency image and convolutional network-based motor imagery eeg classification. *IEEE Access*, 7:6084–6093. (pages 9 and 17)

[Xu, 2021] Xu, K. (2021). Silicon electro-optic micro-modulator fabricated in standard cmos technology as components for all silicon monolithic integrated optoelectronic systems. *Journal of Micromechanics and Microengineering*, 31(5):054001. (page 26)

[Xu et al., 2020] Xu, M., Yao, J., Zhang, Z., Li, R., Yang, B., Li, C., Li, J., and Zhang, J. (2020). Learning eeg topographical representation for classification via convolutional neural network. *Pattern Recognition*, 105:107390. (page 13)

[Yang et al., 2016] Yang, B., Li, H., Wang, Q., and Zhang, Y. (2016). Subject-based feature extraction by using fisher wpd-csp in brain–computer interfaces. *Computer methods and programs in biomedicine*, 129:21–28. (page 2)

[Yang et al., 2021] Yang, L., Song, Y., Ma, K., and Xie, L. (2021). Motor imagery eeg decoding method based on a discriminative feature learning strategy. *IEEE Transactions on Neural Systems and Rehabilitation Engineering*, 29:368–379. (page 11)

[Yang et al., 2022] Yang, S., Li, M., and Wang, J. (2022). Fusing semg and eeg to increase the robustness of hand motion recognition using functional connectivity and gcn. *IEEE Sensors Journal*, 22(24):24309–24319. (page 13)

[Yu et al., 2014] Yu, X., Chum, P., and Sim, K.-B. (2014). Analysis the effect of pca for feature reduction in non-stationary eeg based motor imagery of bci system. *Optik*, 125(3):1498–1502. (page 3)

[Zhang et al., 2021] Zhang, A., Lipton, Z. C., Li, M., and Smola, A. J. (2021). Dive into deep learning. *arXiv preprint arXiv:2106.11342*. (page 50)

[Zhang et al., 2020] Zhang, R., Li, F., Zhang, T., Yao, D., and Xu, P. (2020). Subject inefficiency phenomenon of motor imagery brain-computer interface: Influence factors and potential solutions. *Brain Science Advances*, 6(3):224–241. (page 37)

[Zhang et al., 2018] Zhang, R., Xiao, X., Liu, Z., Jiang, W., Li, J., Cao, Y., Ren, J., Jiang, D., and Cui, L. (2018). A new motor imagery eeg classification method fb-trcsp+ rf based on csp and random forest. *IEEE Access*, 6:44944–44950. (page 10)

[Zhang et al., 2017] Zhang, Y., Wang, Y., Jin, J., and Wang, X. (2017). Sparse bayesian learning for obtaining sparsity of eeg frequency bands based feature vectors in motor imagery classification. *International journal of neural systems*, 27(02):1650032. (page 2)

[Zhang et al., 2019] Zhang, Z., Duan, F., Sole-Casals, J., Dinares-Ferran, J., Cichocki, A., Yang, Z., and Sun, Z. (2019). A novel deep learning approach with data augmentation to classify motor imagery signals. *IEEE Access*, 7:15945–15954. (page 11)